Monte Carlo Simulation Studies for Medical and Astrophysical Applications

Master Thesis

submitted by

Christian Pommranz

January 2019

Eberhard Karls Universität Tübingen

Institute for Astronomy and Astrophysics

Department for High Energy Astrophysics

Hiermit versichere ich, dass ich gemäß des allgemeinen Teils der Studien- und Prüfungsordnung der Universität Tübingen für den Studiengang Physik mit akademischer Abschlussprüfung Master of Science (M.Sc.) vom 30.07.2013 diese Masterarbeit mit dem Titel „Monte Carlo Simulation Studies for Medical and Astrophysical Applications“ selbstständig verfasst und keine anderen als die angegebenen Hilfsmittel und Quellen benutzt habe. Alle wörtlich oder sinngemäß aus anderen Werken übernommenen Aussagen wurden als solche kenntlich gemacht. Die Arbeit war weder vollständig noch in wesentlichen Teilen Gegenstand eines anderen Prüfungsverfahrens und wurde weder vollständig noch in wesentlichen Teilen bereits veröffentlicht. Das in Dateiform eingereichte Exemplar stimmt mit den eingereichten gebundenen Exemplaren überein.

Tübingen, den ...... Januar 2019

....

(**Christian Pommranz**)

Abstract

Monte Carlo simulations have become an increasingly important topic in high energy physics over the last few decades especially as a method for studying systems with a large number of degrees of freedom, such as tracking high energy particles through detector geometries. In this thesis, Monte Carlo simulation studies were performed to estimate performance characteristics for three different geometries of a future breast PET/MR insert for a clinical PET/MR scanner, and to reproduce the measured EPIC pn-CCD camera background on board the ESA X-ray satellite XMM-Newton.

PET performance characteristics for sensitivity and spatial resolution of the insert were investigated and are found to show significant improvements for two of the probed geometries in both sensitivity and spatial resolution near the center of the field of view, with spatial resolutions better than 1.6 mm FWHM, compared to modern clinical PET/MR scanners with roughly 4 mm FWHM. A blurring in the radial direction, referred to as the radial elongation effect, is seen towards the outer regions of the field of view, deteriorating the spatial resolution. Future studies are suggested to explore the impact of Depth Of Interaction (DOI) detectors on the spatial resolution across the whole field of view and especially on the mitigation of the radial elongation effect.

In X-ray astronomy, a sound understanding of the background picked up by X-ray satellites operating in a space environment is crucial, since weak sources must be observable in the presence of a strong background. Foundations for a modern Geant4 simulation environment, inspired by earlier background simulations and enabling enhanced future studies, were developed and used to reproduce the quantum efficiency and background of the EPIC pn-CCD camera with a reasonable agreement with measurements.

Contents

Abstract **v**

1. Introduction **1**

2. Monte Carlo Simulations **3**
2.1. The Monte Carlo Method . . . 3
2.2. Geant4 . . . 4
2.2.1. Creating Geant4 Applications . . . 6
2.2.2. Simulation Geometry . . . 6
2.2.3. Physics Processes . . . 7
2.2.4. General Particle Source . . . 8
2.2.5. Random Number Generator . . . 8
2.3. GATE . . . 9
2.3.1. Simulation Geometry . . . 9
2.3.2. Physics Processes and Sources . . . 10
2.3.3. Readout and Digitization . . . 10
2.3.4. Output . . . 12
2.4. Estimating Statistical Errors of Efficiency Calculations . . . 12

3. Simulation Studies of a Breast PET/MR Insert **15**
3.1. Positron Emission Tomography . . . 15
3.2. Breast PET/MR Insert . . . 19
3.3. Validating Simulation Results . . . 20
3.4. PET Scanner Performance Characteristics . . . 23
3.4.1. Sensitivity . . . 23
3.4.2. Spatial Resolution . . . 25
3.4.3. Maximum Count Rate . . . 29
3.5. Simulation Studies of Breast PET/MR Inserts . . . 30
3.5.1. Two Cylinders Geometry . . . 32
3.5.2. Stretched Cylinder Geometry . . . 37
3.5.3. Peanut Geometry . . . 42
3.6. Conclusion . . . 46

4. Simulation Studies of the XMM-Newton EPIC pn-CCD Camera Background **49**
4.1. X-ray astronomy . . . 49
4.2. XMM-Newton . . . 50
4.3. Simulation Principles for Background Studies . . . 52
4.3.1. Isotropic Background Radiation . . . 52
4.3.2. Normalization . . . 53
4.4. Simulation Studies . . . 56
4.4.1. Simulation Environment . . . 57

4.4.2. Detector Quantum Efficiency 58
4.4.3. Background Spectrum 59
4.5. Conclusion 62

5. Conclusions **65**

Bibliography **67**

Appendix **71**
A. Tabular View of the Simulated Spatial Resolution Results 71

1. Introduction

With the ever increasing computing power available, Monte Carlo simulations have become a more and more important method for studying systems with a large number of degrees of freedom in high energy physics over the last few decades. In this thesis, Monte Carlo simulations are used in two separate fields in physics: medical imaging and high energy astrophysics. Furthermore, the Monte Carlo simulations are performed for two different applications, with the ones in the field of astrophysics helping to understand data previously recorded by an experiment, and the others in the field of medical imaging providing assistance in designing a future detector system.

In Chapter 2.1 an explanation of the basic principles of Monte Carlo simulations is given, followed by introductions to the software toolkits Geant4 (GEometry ANd Tracking) and GATE (Geant4 Application for Emission Tomography), which were used for the performed simulation studies, in Chapters 2.2 and 2.3, respectively. Since estimating statistical errors is crucial for Monte Carlo simulations due to the principle of repeated random sampling, the evaluation of the standard deviation in efficiency calculations is developed in Chapter 2.4.

In the field of medical imaging, simulation studies of a planned hybrid PET/MR (Positron Emission Tomography/Magnetic Resonance) insert dedicated to breast imaging for a clinical PET/MR scanner were performed. Three different possible geometries of the insert device PET detector system were exemplarily probed to obtain the expected PET performance characteristics based on the “NEMA Standards Publication NU 4-2008” for small animal positron emission tomographs [NEM08].

After introducing the basic working principle of PET and motivating multi-modality PET/MR imaging in Chapter 3.1, the planned breast PET/MR insert is described in Chapter 3.2. For validating simulation results obtained with GATE, a simplified experiment using a single detector block was conducted and the count rates as determined by the GATE simulation are compared in Chapter 3.3 against measurement results as well as results from a second simulation relying on another Monte Carlo simulation code. The investigated PET performance characteristics of the insert device are explained in Chapter 3.4 followed by the results of the performed simulation studies and conclusions in Chapters 3.5 and 3.6, respectively.

In the field of high energy astrophysics, background simulation studies for the EPIC-pn camera of the ESA X-ray space observatory XMM-Newton are implemented using Geant4. Previous simulation studies performed by [Ten08] more than ten years ago showed promising results, but could only be realized through workarounds, drastically reducing computation time, and were limited by the physics processes available in Geant4 at that time. Since both the available computing power and the Geant4 toolkit improved significantly in the last decade, the simulation environment was recreated with state of the art technology to provide a basis for more sophisticated future studies.

Short introductions to X-ray astronomy and the XMM-Newton mission are given in Chapters 4.1 and 4.2, respectively, followed by explanations of the methods used for simulating isotropic background radiation and normalizing the results in Chapter 4.3. The performed simulation studies including the results of the simulated detector quantum efficiency and background spectrum are listed in Chapter 4.4 followed by conclusions and an outlook in Chapter 4.5.

The thesis closes with combined conclusions and outlooks for both investigated projects in Chapter 5.

2. Monte Carlo Simulations

2.1. The Monte Carlo Method

Monte Carlo simulations use a stochastic approach based on random or pseudo-random numbers enabling investigation of for instance complex physical problems in statistical physics. Early use of such statistical sampling methods began already in the 18th century by Georges-Louis Leclerc, Comte de Buffon (1707-1788). Assuming a tile floor with parallel lines, it can be shown that dropping a needle with the same length as the distance between two lines leads to a probability of $2/\pi$, that the dropped needle intersects a line. Repeated dropping of needles and counting the intersecting needles therefore yields an estimation for π using

$$\pi \approx \frac{2 \cdot n}{x} \tag{2.1}$$

with the total number of dropped needles n and the count of intersecting needles x [Har10]. Exemplary simulation results for 100 dropped needles are shown in Figure 2.1.

While random sampling methods were used in the 19th and early 20th centuries for statistically analyzing deterministic problems, which were already understood, modern Monte Carlo simulations are often used to study problems, which are difficult to address analytically, or where an experimental approach is impractical or too expensive [Har10]. In the early 30s of the 20th century Enrico Fermi invented the "Fermiac" shown in Figure 2.2, a mechanical device used to determine neutron diffusion in nuclear systems [Met87]. With the computing capacities of modern electronic computers, Monte Carlo methods became popular for studying systems with a large number of degrees of freedom, such as tracking high energy particles through detector geometries.

In contrast to other simulation methods, the Monte Carlo method only needs a modeled system of probability density functions (PDFs) for the performed simulation step. Therefore, precise knowledge of the differential equations of the underlying physics is not necessarily required for Monte Carlo simulations. The nature of PDFs places two constraints on the respective functions. The PDF must be

- a positive real-valued function, since negative or non-real probabilities would not be physically reasonable,
- normalized, ensuring that the integral over the complete PDF equals to 1, since the particle must be in one of the possible states after sampling [Har10].

The integral of the PDF is referred to as cumulative density function (CDF). For an invertible CDF, sampling from the given distribution can be performed using the inversion method with a uniformly distributed random number provided by a

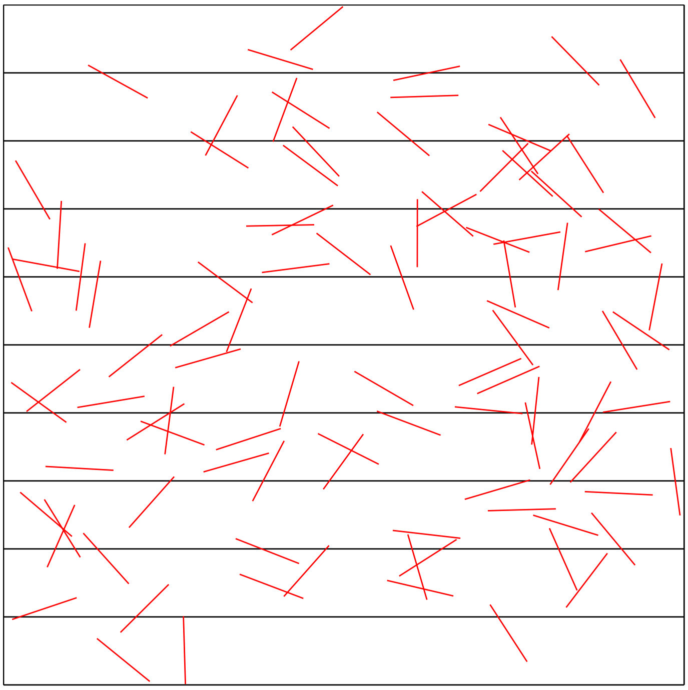

Figure 2.1.: Needles (red lines) dropped onto a tiled floor (black lines) calculated and plotted by a simple illustrative simulation program written by the author. 100 needle drops are simulated and plotted, which resulted in $\pi \approx 3.125$ for the given seed. The needle length and distance of two parallel lines are set to 1 unit length. The floor size measures 10×10 unit lengths.

random number generator (RNG). For example, assuming a PDF p of an exponential distribution describing the time between two radioactive decays in a source activity of the form

$$p(x) = \lambda \cdot e^{-\lambda x} \tag{2.2}$$

with an adjustment parameter λ and $x \geq 0$ yields the CDF P

$$P(x) = 1 - e^{-\lambda x} \quad . \tag{2.3}$$

The integration constant can be obtained by stating, that after waiting an infinite amount of time the decay must have happened. Requesting a uniformly distributed random number u from the RNG and inserting it into the inverted CDF

$$x = P^{-1}(u) = -\frac{\ln(1-u)}{\lambda} \tag{2.4}$$

finally leads to the sample of the exponential distribution x [Har10].

2.2. Geant4

Geant4 (GEometry ANd Tracking) is an object-oriented Monte Carlo simulation toolkit developed by the international Geant4 Collaboration in the C++ programming language and released as open-source software under the custom “Geant4 Software License”. Multiple parts of the software simulation process are included in Geant4,

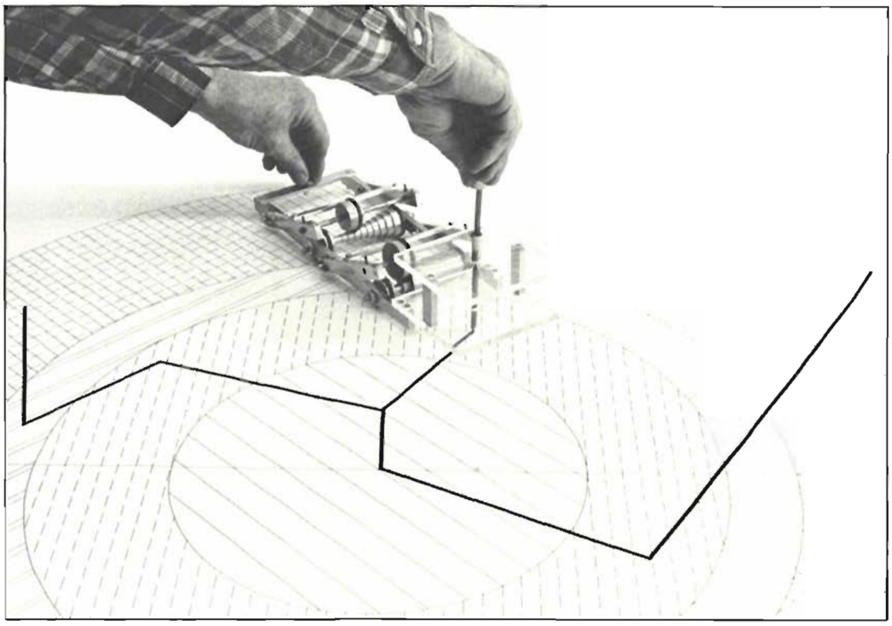

Figure 2.2.: Fermiac, or Monte Carlo trolley, invented by Enrico Fermi. The drums are set to track either slow or fast neutrons based on a random choice through material reflected in the drum configuration. Direction of motion and distance to the next point of interaction between particle and material are determined by additional random numbers. Drawing a line while rolling, the trolley is moved through the two-dimensional reactor arrangement [Met87].

ranging from geometry definition of the system and sensitive detectors, over particle creation and particle tracking through the experiment geometry and electromagnetic fields, to storage of resulting data and visualization [A+03].

Development of Geant4 began in 1993 with two working groups at CERN and KEK independently investigating how GEANT3, written in the FORTRAN language, could benefit from modern computing techniques and programming patterns, such as object-oriented programming. Both projects merged in the international RD44 collaboration, which finalized the choice of design patterns and released the first productive version of Geant4 written in C++ in 1998 [A+03]. Today, the Geant4 Collaboration established in 1999 keeps adding new features to the toolkit, providing fixes to known bugs and maintaining documentation. New feature releases to the current Geant4 generation 10 are released about once a year with the most recent version being v10.4.2 at the time of writing. Recent major improvements to Geant4 include the possibility to create multithreaded simulations added in version 10.0 [A+16].

The user documentation of Geant4, which this chapter is based upon, is available online[1], including detailed guides for application developers creating their own simulations as well as for toolkit developers contributing to Geant4 itself.

[1] https://geant4.web.cern.ch/support/user_documentation

2.2.1. Creating Geant4 Applications

Geant4 simulations are created by developing an application written in C++, which configures the simulation workflow and implements mandatory abstract classes provided by the toolkit. The key class to instantiate in the application main file is "G4RunManager", or "G4MTRunManager" in case of multithreading. The created run manager is the fundamental Geant4 class used to configure and initialize important parts of the simulation, such as:

- the detector geometry and sensitive detectors (Chapter 2.2.2),
- a physics list describing all physical processes considered in the simulation (Chapter 2.2.3),
- action classes, including a primary particle generator (Chapter 2.2.4) and optional actions performed at fixed states of the simulation, i.e. at the beginning or end of each simulated event.

Furthermore, the run manager is responsible for controlling the flow of the performed simulation as well as managing the event loops of each run. Optionally, the user can derive a custom run manager class from G4RunManager or G4MTRunManager, allowing modifications to the basic run control behavior.

The additional management class "G4UImanager" is commonly used in the application main file. It allows to control the "intercoms" category providing a command interpreter as well as multiple types of user interfaces to control the application. The command interpreter can be used to configure parts of the application at run time, such as the primary particle source, either interactively or by batch processing a series of commands given in a macro file. Therefore, multiple similar simulations with different configurations can be performed without editing the C++ code and recompiling.

2.2.2. Simulation Geometry

The simulation geometry is implemented in Geant4 applications using the concept of volumes, representing the shape and physical characteristics of the building blocks of the geometry. The volumes are arranged in a hierarchical way with a single "world volume" containing all other defined volumes.

In earlier Geant4 versions, the detector construction and definition of materials was set up in the application code by deriving a class from the "G4VUserDetector-Construction" abstract class and implementing the geometry in C++. More recent versions allow the detector definition to be provided in the Geometry Description Markup Language (GDML)[2] based on the Extensible Markup Language (XML). Keeping all necessary information about the detector geometry in GDML files strongly adheres to the separation of concerns design principle and permits sharing of the geometry or parts of it between separate Geant4 applications. Since GDML is realized using a set of XML schema definition files without modifications to XML itself, it can be used as a universal format for storing geometry and material information. Converters from Computer-Aided Design (CAD) programs to GDML

[2] http://gdml.web.cern.ch/GDML/

exist either based on Constructive Solid Geometry (CSG) supporting specific CAD tools like SolidWorks [VCD+17], or based on tessellated solids allowing for more generic translation of STEP files used by multiple CAD tools into GDML [PG18], but leading to reduced Geant4 performance in terms of simulation time especially for more complex geometries.

2.2.3. Physics Processes

In Geant4 the physics processes are implemented in an object-oriented design using the same abstract interface for all individual physics processes, adhering to the Geant4 design goal of an open and easy to inspect physics implementation. The common abstract interface leads to a decoupling of the particle tracking mechanism from the details of the underlying physics, allowing for modifying or adding physics processes without interfering with other parts of the Geant4 toolkit. This approach also enables complementary or alternative physics models in order to cover large energy ranges in simulations [A+03]. Today, Geant4 users can choose from many competing options for physics processes and models, varying for example in accuracy or computational cost. Therefore, customized physics lists for particular use cases can be assembled. Multiple predefined exemplary physics lists for dedicated simulation scenarios are included in the Geant4 toolkit, each providing a consistent set of models [A+06].

Particles are transported through the geometry in single steps with dynamic length. For each configured physics process applicable for the tracked particle type, Geant4 calculates a distance to the next interaction based on its probability density function

$$p\left(l\right) = e^{-n_\lambda}, \qquad n_\lambda = \int_0^{l'} \frac{1}{\lambda\left(l\right)} dl \tag{2.5}$$

with the length l and the mean free path λ. The specific distance for the currently simulated particle in the material is determined (compare Section 2.1) by setting

$$n_\lambda = -\ln\left(\eta\right) \tag{2.6}$$

with a uniformly distributed random number η generated by a pseudo-random number generator as described in Section 2.2.5 [A+03].

The process yielding the smallest length will be chosen, if no geometry boundaries are crossed and the allowed step length range configurable by the user allows it. For particles at rest, a step time is calculated in a similar fashion. Multiple types of actions can be connected to a process and triggered by the tracking mechanism, namely actions

- at rest, e.g. decays, applicable for particles with negligible kinetic energy,
- along steps, e.g. Cherenkov radiation, for continuous interactions,
- post steps, e.g. producing secondary particles, for decays or interactions taking place after the calculated step [A+03].

2.2.4. General Particle Source

At the beginning of each event a primary particle is created for tracking through the defined geometry. Besides the simple "G4ParticleGun" creating particles with a specified position and momentum, the more elaborate General Particle Source (GPS) can be used to create particles of a certain type following configured energy, position and angular distributions. The GPS can be configured completely via macro files, allowing for quick modifications of settings between simulation runs and for reusing configurations across different Geant4 applications.

The primary particle position can be defined with macro commands using the "/gps/pos/" prefix. Valid configuration options include a point source, particles created on two-dimensional planes like circles, ellipses or rectangles, and particles spawned either on the surface or inside the volume of three-dimensional spheres, cylinders, elliptical cylinders, ellipsoids and parallelepipeds. The particle source can be positioned at arbitrary locations inside the simulation world volume.

Angular distributions can be applied to the generated particles in multiple fashions, such as isotropic and cosine-law using the "/gps/ang/" command prefix, or by providing a distribution defined by the user. The cosine-law model, following Lambert's cosine law, can be used to mimic isotropic background radiation in space by applying it to the inner surface of a large sphere (see Section 4.3.1). Additional biasing can be set to limit the values of the θ and ϕ angles of the defined distributions.

The energy of the primary particles generated by the general particle source follows the configured energy distribution ranging from a fixed energy used for generating mono-energetic particles to more sophisticated predefined options including black body or bremsstrahlung spectra. Customized energy distributions are set using histograms with a maximum of 1024 bins providing the energy and weight of each bin. For interpolation of the given energies, multiple types including linear interpolation and the cubic splines method are available.

2.2.5. Random Number Generator

Reliable generators for random or pseudo-random numbers are crucial for Geant4 simulations and Monte Carlo simulation tools in general, since due to the statistical nature of Monte Carlo simulations, valid results can only be obtained for random number generators yielding uncorrelated and uniformly distributed numbers. Pseudo-random number generators (PRNGs) rely on deterministic algorithms for generating numbers determined by an initial given seed. Therefore, PRNGs are of particular interest for simulation studies, since results are reproducible by repeating a simulation with the same seed. Still, simulations with a large number of created primary particles can be split up into smaller portions for concurrent execution on multiple processing units by setting different initial seeds for every separate run.

Geant4 uses the "HEPRandom" module distributed with "a Class Library for High Energy Physics" (CLHEP), offering several utility classes designed for high energy physics simulations. CLHEP provides an abstract base class "HepRandomEngine" acting as a common interface for various implemented PRNGs. The "RanecuEngine" originally written in FORTRAN77 as part of the MATHLIB HEP library is of special interest and was used in the Geant4 simulation environment developed in the course of this thesis, due to its simple internal representation of the current engine state, allowing for simple reproduction of specific events of a simulation.

2.3. GATE

The Geant4 Application for Emission Tomography (GATE) is a simulation toolkit mainly focused on medical imaging applications such as PET, Single-Photon Emission Computed Tomography (SPECT) and Computed Tomography (CT) systems as well as radiotherapy [J+11], [J+04]. Realized as a Geant4 application, GATE is written in the C++ language while being controlled and configured using text files containing a dedicated scripting mechanism, referred to as macros. This allows development and configuration of GATE simulations without requiring knowledge of C++ or programming in general. While reducing flexibility due to restricting functionality to the features provided in the macro mechanism, GATE significantly simplifies simulation definitions and therefore allows for faster developing and adapting of simulations. GATE is open-source software developed by the OpenGATE collaboration and licensed under the GNU Lesser General Public License in version 3.

Besides implementing functionality dedicated to medical imaging applications, GATE extends Geant4 with the ability to model time-dependent processes. Subdividing the simulation process into multiple time steps allows the user to include moving parts to the probed geometry or to include source isotopes with decreasing activities in the process of the simulation. While the geometry is fixed in each simulated time step, the source activity decrease can dynamically be calculated also within a single time step.

In the course of this thesis, GATE was used for the simulation studies of the breast PET/MR insert described in Chapter 3. The most important features and settings used for this work are introduced in the following sections. This chapter is based upon the detailed GATE users guide available online[3].

2.3.1. Simulation Geometry

For defining the geometry of the simulation, GATE offers a selection of fundamental shapes as a starting point to build more complex geometries. This selection includes simple shapes like boxes and cylinders, as well as more elaborate shapes such as ellipsoids and wedges. Additionally, a tessellated shape allows the user to define a custom basic shape using a separate text file containing the vertices, which can be used to include more complex shapes created with a Computer-Aided Design (CAD) program. An extendable database of material definitions is included in GATE in form of a text file. Since GATE is implemented as a Geant4 application, the basic Geant4 constraints also apply to geometries defined using GATE macros:

- Volumes located inside another volume must be set as its daughter volumes.
- Daughter volumes must be completely included in their respective mother volume.

[3] http://wiki.opengatecollaboration.org/index.php/Users_Guide

- Separate volumes are not allowed to overlap each other.

Violating these constraints can lead to erroneous simulation results.

To allow for convenient copying of volumes in the simulation environment, the concept of repeaters is supported in the macro language. In addition to predefined repeaters such as the linear and ring repeaters, a generic repeater is implemented, which reads a given text file containing arbitrary volume translations and rotations for given time steps. The generic repeater method is used in the simulation studies described in Chapter 3, with the text file automatically produced by a custom helper tool developed in the course of this thesis offering repeater functionality needed for the probed geometries.

The concept of “systems” is essential for GATE simulations. Multiple predefined systems exist, such as “cylindricalPET” or “ecat”. These systems act like templates for the detector geometry and put constraints on the shape and hierarchical structure of volumes used in the geometry attached to a specific system. These constraints ensure that different detector setups of the same system share the same geometrical characteristics, such as the number of hierarchical levels of components. This allows GATE to simulate the readout electronics and signal processing, as well as adding dedicated output formats to specific systems. For PET detector geometries not covered by the predefined systems, a “PETScanner” system with limited functionality exists, which adds no geometrical constraints.

2.3.2. Physics Processes and Sources

Recent versions of GATE provide the ability to load physics lists into its Geant4 core. Previously, it was necessary to manually add all desired physical processes using macro commands. For the performed simulation studies in Chapter 3 the “emstandard_opt3” physics list was chosen, offering the Geant4 standard electromagnetic processes together with a more detailed Compton scattering model. Further physics processes can be added to the simulation, such as a radioactive decay process enabling the use of a generic ion source using a simulated nuclear decay as starting point to each simulated event.

Alongside the ion source, simplified types of sources can be configured. Wrapping Geant4 GPS commands, GATE offers the possibility to create simple particle sources producing mono-energetic particles or following a given energy spectrum. In order to save simulation time compared to a more realistic simulation of positron-emitting sources, a “back-to-back” photon source emitting two annihilation photons with an angle of 180° is implemented in GATE.

2.3.3. Readout and Digitization

Multiple processes are available in GATE for simulating the impact of readout electronics and the signal processing chain on the measured data. In terms of the simulation, this refers to the conversion from the simulated particle trajectory (“track”) and the interactions between the photon and the sensitive detector material (“hits”) to data observed by a real detector, such as single or coincident events. In order to obtain the resulting digital values, multiple digitizer modules describing

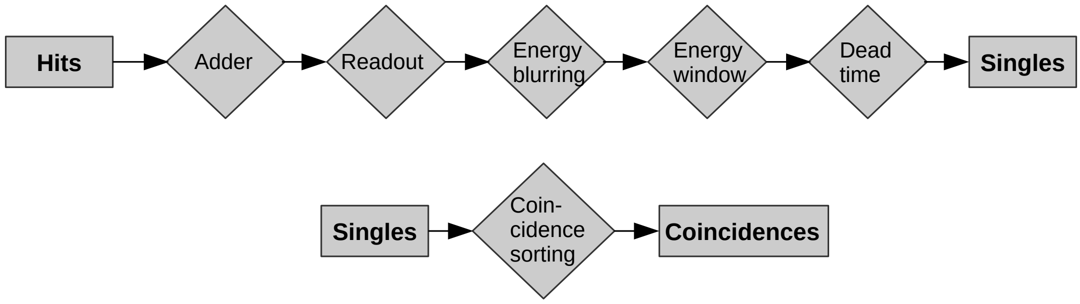

Figure 2.3.: Exemplary GATE digitizer chain similar to the configuration used for the performed simulation studies.

sampling methods of the signal are configured and organized into a digitizer chain. The individual modules of an exemplary digitizer chain similar to the chains used in the performed simulation studies are shown in Figure 2.3 and introduced in the following list.

- **Adder:** Multiple interactions between a photon and the sensitive detector material can occur in a single crystal producing multiple hits. Since a real detector cannot distinguish between the single interactions, the individual hits in a single crystal are summed up by the adder module to a “pulse” object.

- **Readout:** Individual crystals can be grouped and read out together to mimic the behavior of detectors with a different amount of photosensors compared to the number of crystals per block. While the energy of the resulting single pulse is the sum of all concerned per-crystal pulses, two different policies exist for setting the position of the resulting pulse. While the “TakeEnergyCentroid” policy calculates the energy centroid position, the “TakeEnergyWinner” policy was applied for the performed simulation studies, using the coordinates of the interaction with the highest deposited energy as the resulting position.

- **Energy blurring:** The energy blurring module applies a Gaussian blurring to the resulting deposited energy, simulating a finite energy resolution of the detector. For the simulated detectors an energy resolution following an inverse square law of the form
$$R = \frac{R_0 \cdot E_0}{\sqrt{E}} \tag{2.7}$$
is chosen with the resulting resolution R (FWHM), the configured resolution R_0 (FWHM) at the energy of reference E_0, and the energy of the pulse E.

- **Energy window:** For limiting acquired data to a given energy window and dropping all other events, thresholder and upholder modules can be configured and added to the digitizer chain.

- **Dead time:** Real detectors show a dead time effect after detecting events resulting in a dead time window, in which impinging photons are undetected. Dead time windows can be simulated using GATE in a paralyzable or non-paralyzable manner. In the non-paralyzable case, only detected photons trigger a following dead time window, while in the paralyzable mode a dead time window is opened on each photon interaction, possibly resulting in less detected events in the case of high interaction rates.

- **Coincidence sorter:** Multiple single events can be marked as coincident events using the coincidence sorter module. By default, a coincidence window with a configured duration is only opened on a detected single event if no other coincidence window is already opened. Another policy opening a new coincidence window for every detected event is implemented in GATE, but marked as experimental. This policy can result in more detected coincidences compared to the policy using a single coincidence window. Different policies are available for determining the coincidence sorter behavior in case more than two single events are detected in one coincidence window. In the performed simulation studies the "takeWinnerOfGoods" policy is set, taking only the valid coincident pair with the highest sum of single event energies into account.

2.3.4. Output

GATE supports writing the simulation results into various different output formats. While ASCII and ROOT output are also available for generic scanner systems, several predefined systems additionally provide specific output formats, such as ECAT7. The ROOT output module writes the simulated hits, singles and coincidence events into their own trees in the results file. For debugging, the output module can be configured to fill additional trees with the resulting events at multiple stages of the digitizer chain. To decrease the size of the resulting ROOT file and save computation time, it is possible to activate a specific tree while dropping all other resulting data.

2.4. Estimating Statistical Errors of Efficiency Calculations

In order to obtain significant results about the response function of detectors investigated using the Monte Carlo method, it is essential to have an estimation of the statistical uncertainties of the performed simulations. Although frequently applied for Monte Carlo simulations, the Poissonian and Binomial error calculations show problematic results in extreme cases: Since the total number of events n is a fixed quantity, assuming an efficiency definition of the form $E(\epsilon) = \hat{\epsilon} = \frac{k}{n}$ with k being the number of detected events leads to the variance $V(\hat{\epsilon}) = \frac{k}{n^2}$ using the Poisson distribution. For a single simulated event, which is not detected ($k = 0$ and $n = 1$), this would erroneously yield zero uncertainty. The same problematic behavior can be found for the Binomial error calculation leading to the variance $V(\hat{\epsilon}) = \frac{k(n-k)}{n^3}$. In addition, the second limit $n = k$ yields a vanishing uncertainty for the Binomial method even for a minimal simulation with $n = k = 1$ [UX07].

With the previously described methods being inadequate for estimating the errors of efficiency calculations for a very low number of events, Ullrich and Xu propose [UX07] a different probability function of the form

$$P(\epsilon; k, n) = \frac{(n+1)!}{k!\,(n-k)!}\epsilon^k (1-\epsilon)^{n-k} \quad , \tag{2.8}$$

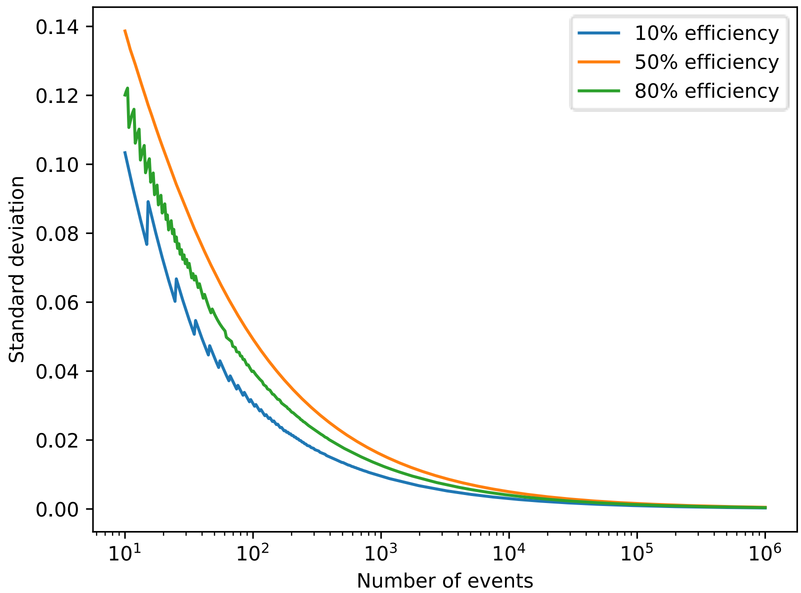

Figure 2.4.: Standard deviation of Monte Carlo efficiency simulations for different efficiencies and numbers of simulated events. The jitter at lower numbers of events is due to the numbers of detected events ($k = \hat{\epsilon} \cdot n$ with the efficiency $\hat{\epsilon}$ and the number of events n) being rounded to integer values.

which correctly assigns zero probability to $\epsilon = 0$ and $\epsilon = 1$ unless $k = 0$ or $k = n$, respectively. This probability density leads to the standard deviation

$$\sigma = \sqrt{\frac{(k+1)(k+2)}{(n+2)(n+3)} - \frac{(k+1)^2}{(n+2)^2}} \tag{2.9}$$

for efficiency calculations, which is used throughout this thesis to estimate the statistical errors of the performed Monte Carlo simulations.

For three exemplary efficiencies the standard deviation in dependence of the total simulated number of events n is calculated using Equation 2.9 and plotted in Figure 2.4. To lower the statistical uncertainties of Monte Carlo simulations it is generally advisable to increase the number of simulated events.

3. Simulation Studies of a Breast PET/MR Insert

3.1. Positron Emission Tomography

Positron Emission Tomography (PET) is a modality of physiological imaging with applications in varying fields in medicine and research, such as oncology or molecular imaging. As a scintigraphic method, PET provides improved functional and metabolic information about tumor cells compared to other imaging modalities like Computed Tomography (CT) [SK06].

Tumor cells show significantly enhanced glucose utilization compared to normal tissues. Radiopharmaceuticals like FluoroDeoxyGlucose (FDG) – an analog of 2-deoxyglucose – accumulate in regions with higher metabolic activity, such as tumor cells. Labeling of FDG with the positron emitting radionuclide ^{18}F before injection into the patient enables visualization of the tracer distribution in the patient body. Today, FDG is the major workhorse in PET [SK06].

The basic PET working principle is illustrated in Figure 3.1. Beta plus decays of the injected radionuclide produce electron neutrinos and positrons. While the neutrinos leave the patient without interaction due to the small cross section, the charged positrons scatter and stop in the surrounding tissue. Finally, the positron and a nearby electron form an unstable bound quantum state referred to as positronium, which in a dense medium predominantly decays into two gamma-rays with energies of 511 keV each in opposite directions in the positronium rest frame. Detecting two coincident photons yields a line of response (LOR) connecting the impinged detector elements. With many LORs detected, the radionuclide distribution in the field of view can be visualized using reconstruction techniques.

Detection of annihilation photons in PET is most commonly performed with scintillation detectors. The scintillators, made of inorganic crystal with a high stopping efficiency due to their high atomic number and density, produce photons in the visible band on interaction with a gamma-ray [BTVM05]. Today, Lutetium Oxyorthosilicate (LSO) is commonly used as PET scintillator material. Compared with the former predominantly used Bismuth Germanate (BGO) it offers higher light output and enables shorter dead time windows [SK06]. Energy reconstruction is possible due to the proportionality of the number of produced visible photons to the energy of the impinging photon. Photomultiplier tubes (PMTs) are frequently used as photosensors in PET scintillation detectors, while recent developments in semiconductor based sensors, such as the Avalanche Photo Diode (APD), provide promising alternatives, but show a gain highly sensitive to variations in temperature [BTVM05].

For determining whether two detected gamma-rays should be marked as coincident, PET scanners use a coincidence sorting mechanism, where coincidences are marked

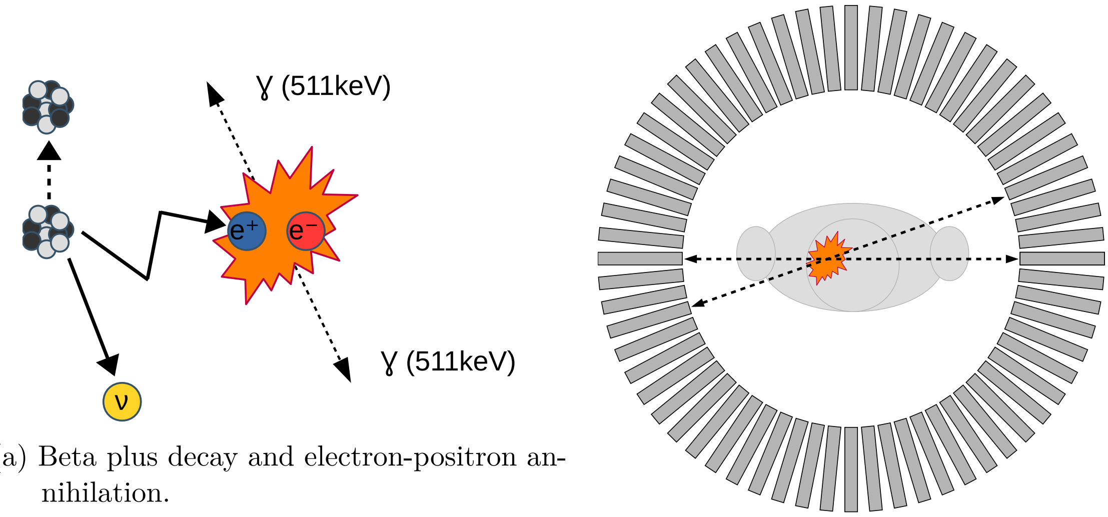

(a) Beta plus decay and electron-positron annihilation.

(b) True coincidences.

Figure 3.1.: Basic PET physics. The radioactive element of the tracer injected into the patient (i.e. ^{18}F in case of FDG) disintegrates via beta plus decay emitting an electron neutrino and a positron (a). After losing energy through scattering in the surrounding tissue, the positron eventually finds an electron for annihilation producing two 511 keV photons in opposite direction. Detection of multiple pairs of coincident photons allows for reconstruction of the tracer distribution in the patient (b).

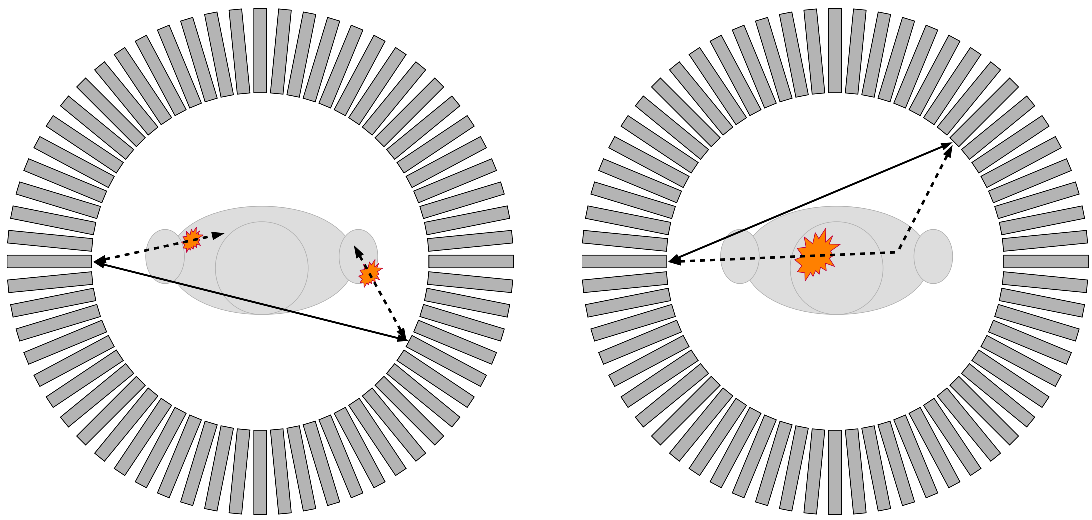

(a) Random coincidence.

(b) Scattered event.

Figure 3.2.: Two possibilities of misplaced lines of response. Random coincidences (a) occur in the case of detecting two photons from independent decays taking place in a single coincidence time window. Compton scattering of photons (b) can introduce misplaced lines of response for detected photons of a single decay.

Figure 3.3.: Siemens “Biograph mMR” PET/MR scanner at the Universitätsklinikum Tübingen. Image: Universitätsklinikum Tübingen.

for two photons detected within a fixed time window, usually between 4 ns and 12 ns, depending on the scanner [SK06]. This coincidence sorting can lead to misplaced LORs due to marking unrelated photons as coincident, referred to as random coincidences, as shown in Figure 3.2a. For higher activities, more random coincidences occur due to the fixed time window of the coincidence sorter. In general, random coincidences can be reduced by using shorter coincidence time windows.

Misplaced LORs can also occur in case of Compton scattered photons as depicted in Figure 3.2b. During the Compton scattering, part of the photon energy is transferred to an electron, leading to a decreased photon energy

$$E' = \frac{E}{1 + \frac{E}{m_e c^2} \cdot (1 - \cos\theta)} \tag{3.1}$$

with the photon energies E and E' before and after the scattering event, respectively, the electron rest mass m_e and the scattering angle θ. Therefore, detected scattered events with larger scattering angles can be reduced by increasing the lower threshold of the energy acceptance window applied to each detected single event.

With the first commercial hybrid PET/CT scanners available in 2001 for multi-modality imaging, clinical dedicated PET devices were driven out of the market within a few years. PET and CT provide complementary features in the acquired data, with the anatomical information of CT images allowing to accurately localize functional abnormalities. Combined PET/CT scanners replace the difficult process of fusing the individual images, which demands accurate alignment after acquisition. These devices also allow for attenuation correction of the PET data using the acquired CT images, which requires energy scaling techniques to estimate the attenuation of 511 keV gamma-rays from CT X-ray energies of about 70 keV. The time consuming process of obtaining attenuation correction using transmission scans, where a gamma-ray source is moved around the patient while measuring the photons transmitted through the body, can be replaced with CT data [Tow08].

PET/MR combining PET and Magnetic Resonance Imaging (MRI) is another modern multi-modality imaging technique with the first clinical PET/MR scanners available since 2010. A clinical Siemens “Biograph mMR” PET/MR scanner combining a PET and MR detector in a single device resembling the shape of conventional MR devices

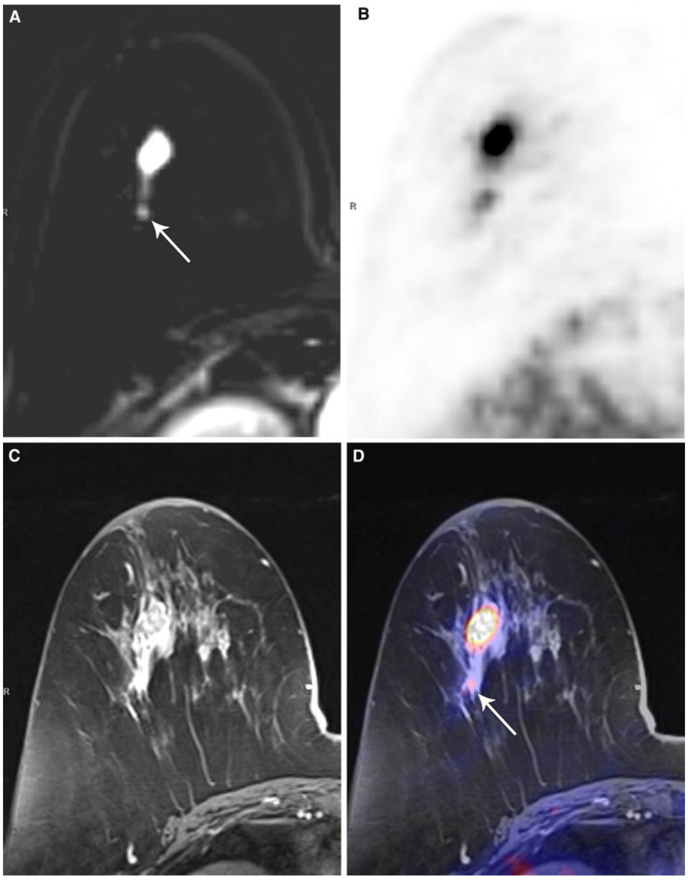

Figure 3.4.: Axial images showing satellite nodules in the breast. Contrast enhanced (CE) MR subtracted image (A) obtained by subtracting a mask image taken before the injection of the contrast agent from the image taken after contrast administration. FDG PET image (B), high-resolution CE MR image (C) and fused high-resolution CE PET-MR image (D). The spatial overlapping of anatomical and functional data from CE MR (arrow in A, C) and metabolic information due to increased FDG uptake (B and arrow in D) in the satellite nodule improves confidence in confirming the satellite nodule as tumor. Image: [C+17].

is shown in Figure 3.3. Single component and fused images of a contrast enhanced PET/MR scan are depicted in Figure 3.4. Combining the complementary data of the high sensitivity for lesion detection of MRI and PET with its high specificity for identifying cancer leads to improved imaging of certain parts of the human body, such as improved breast imaging following X-ray mammographic screening. The reduced radiation exposure compared to PET/CT is advantageous especially for pediatric patients and patients needing repeated scanning [MD14].

Combining PET and MR in a simultaneous scanner holds challenges due to mutual interplay between both techniques. MR scanners need a very homogeneous main magnetic field to stimulate proton resonance at a precise frequency. Placing ferromagnetic materials in the field of view potentially degrades the magnetic field homogeneity and therefore causes artifacts in the resulting image. Further, PET detectors can interfere with the MR scanner detecting small radio frequency (RF) signals due to electromagnetic noise. Consequently, the PET detectors must be carefully designed to minimize caused inhomogeneities to the magnetic field and reduce electromagnetic noise. In addition, the strong magnetic field of the MR device impacts the gain of the PMTs used in traditional PET scanners. In the first clinical simultaneous PET/MR scanners, PMTs were therefore replaced by Silicon Photomultipliers (SiPMs) using APDs, which show less sensitivity to magnetic fields [MD14].

3.2. Breast PET/MR Insert

Global cancer data in the GLOBOCAN 2018 database estimates breast cancer as the leading cause of cancer death in women and the most frequently diagnosed cancer in women worldwide [BFS+18]. The tumors show diversity in their molecular, phenotypic or behavioral characteristics among different patients, referred to as inter-tumor heterogeneity. Therapies are further complicated by intra-tumor heterogeneity, describing similar diversity within a primary tumor of a single patient, demanding precise diagnoses and individualized treatment strategies [KBA15], [MNP+14].

Combined clinical PET/MR scanners offer potential advantages for breast cancer imaging [RF16]. For improved MR imaging, patient beds with integrated MR coils dedicated for breast imaging and suitable for operation in clinical PET/MR scanners are available on the market. Figure 3.5 shows an optical photograph and a computed tomography (CT) scan of a NORAS MRI products patient bed at the Universitätsklinikum Tübingen. A common limitation to the PET imaging quality of clinical PET and PET/MR scanners is given by their spatial resolution as introduced in Chapter 3.4.2. Since the spatial resolution depends on the detector size with small animal PET scanners usually yielding better spatial resolution than clinical devices, a dedicated breast PET insert device could potentially increase spatial resolution and sensitivity for regions in and around the breast, improving PET imaging quality.

Integrating a PET scanner into the patient bed with already integrated MR coils as shown in Figure 3.5 would lead to a combined breast PET/MR insert device for a clinical PET/MR scanner. The patient bed mainly is composed of two horizontal levels and offers unused space between the upper and lower level. In order to integrate PET detector blocks into the patient bed with impacting the magnetic field of the breast coils inside the fields of view as little as possible, placing the blocks outside

(a) Optical photograph.

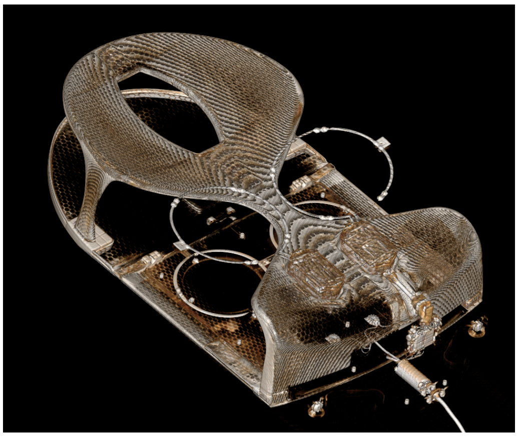

(b) Computed tomography scan.

Figure 3.5.: NORAS MRI products patient bed, which will frame the planned PET insert (a). Coils are integrated into the upper and lower level around the circular cavities for more detailed magnetic resonance imaging of the field of view. These coils are clearly visible in the CT scan (b). The unused volume between the upper and lower coils is available for allocation by the PET breast insert.

the MR fields of view seems reasonable. Another possibility to include a PET scanner, is to elaborate structural changes to the existing patient bed. However, decisive modifications of the bed geometry could probably make adaptations and re-optimizations to the MR parts of the patient bed necessary.

The patient bed in its current form offers a minimum distance between the upper and lower breast coils of roughly 12 cm[1]. The small distance of about 2 cm between the upper coils with a radius of roughly 20 cm represents the critical point for a PET device geometry fitting into the patient bed without modification, since two detector blocks with an anticipated crystal length of 10 mm do not fit into this volume in a back-to-back arrangement.

Multiple geometries suitable for mounting into the patient bed can be designed. In the following simulation studies, three different exemplary breast PET insert geometries are investigated. Although requiring a larger distance between the upper breast coils and therefore making adaptations to the patient bed necessary, a geometry composed of two cylindrical PET scanners is simulated in Chapter 3.5.1. Two more geometries fitting into the unmodified bed are designed and simulated in the course of this thesis, one built by using a detector block setup based on a stretched cylinder (Chapter 3.5.2) and another geometry resembling the shape of a peanut (Chapter 3.5.3).

3.3. Validating Simulation Results

Before simulating and determining performance characteristics of varying detector geometries, a simple experiment was outlined for validating GATE simulation results against a second simulation realized using different software, as well as a measurement. The measurement was performed by Fabian Schmidt at the Werner Siemens Imaging

[1]Precise measures of the patient bed geometry are known to the author.

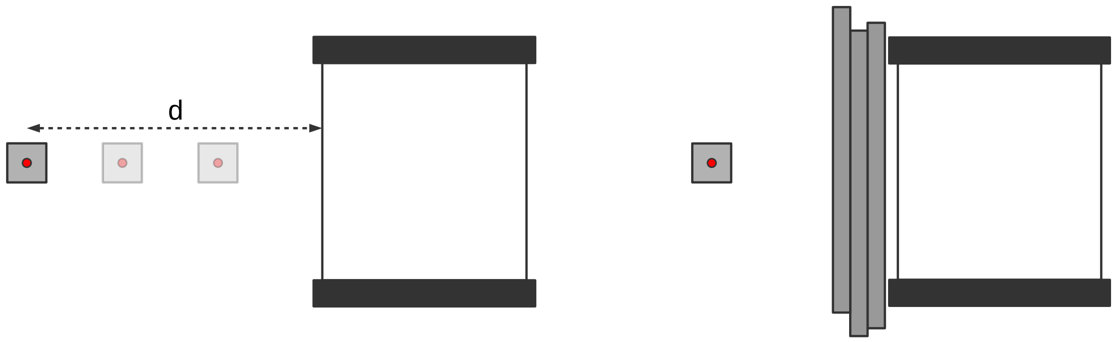

(a) Varying source distances. (b) Varying PCB barrier thickness.

Figure 3.6.: Sketches of the performed validation experiments. The detector block is irradiated from the side using a ^{22}Na gamma source. One test series is carried out with varying distances between detector block and source (a). For a second experiment, the source is placed at a fixed distance of 4 cm to the detector block, and up to three PCB plates are iteratively placed in the line of sight to validate the simulated attenuation (b).

Center (WSIC) in Tübingen, while the second simulation was executed by Dr. Johannes Breuer at Siemens Healthineers using the "PETSim" software[2].

For the validation setup, a dual-side read out detector block with 12×12 20 mm long Lutetium Oxyorthosilicate (LSO) crystals was probed. The edge lengths of the crystal square front faces measure 1.52 mm and the crystal pitch is 1.60 mm. The individual crystals are separated from each other by an Enhanced Specular Reflector (ESR) film. Two setups are examined using this detector block as illustrated in Figure 3.6. A first measurement series is performed with a ^{22}Na gamma source placed in distances measuring multiples of 2 cm in the range from 4 cm to 16 cm between the center of the cubic source and the nearest side of the detector block. A source activity of 458 kBq was obtained using a well counter.

The count rate of single photons detected in the block is measured and simulated for obtained energies between 435 keV and 650 keV, while an energy resolution of 15 % at a reference energy of 511 keV is added in the simulations by applying an energy blurring using an inverse square law. To minimize statistical errors, a duration of 10 s was simulated using GATE, resulting in 4.58×10^6 simulated decays.

The count rate estimated by the PETSim and GATE simulations as well as the measured count rate are depicted in Figure 3.7. Both simulations are in very good accordance with each other. GATE simulations yield slightly higher count rates compared to the PETSim results, which is expected, since PETSim ignores bremsstrahlung effects, while the physics list configured in GATE activates bremsstrahlung processes in the Geant4 physics calculations. Both simulations overestimate the measured count rates by between 8 % and 22 % depending on the individual source position. Variations of the relative offset and deviations of the measured values from an inverse-square law could possibly be due to uncertainties in the source placement, since the source mounting was placed for each individual position by hand. A constant relative offset between measurement and simulations is explainable with uncertainties in

[2]PETSim is developed by Dr. Johannes Breuer, Siemens Healthineers. The physics engine is developed from scratch. Therefore, in contrast to GATE, it is not based on Geant4.

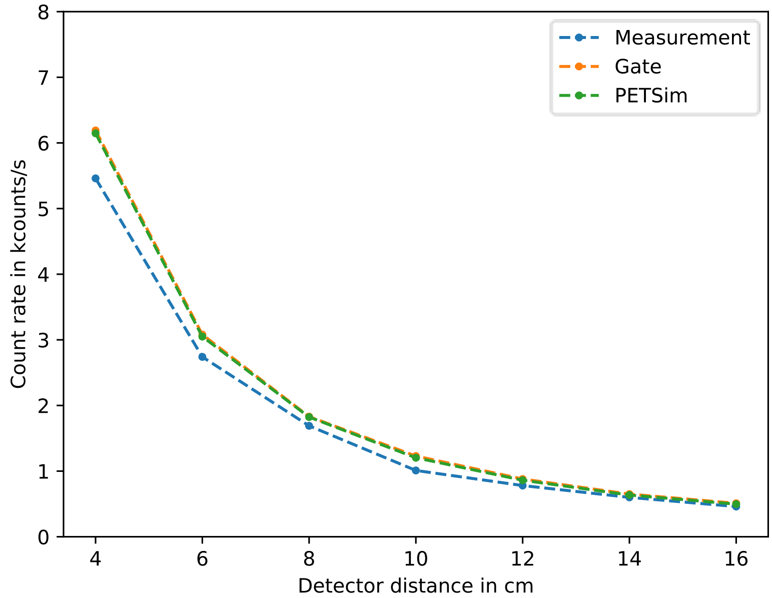

Figure 3.7.: Comparison between measured and simulated count rates depending on the source distance. Simulations were performed using the GATE and PETSim simulation tools. Dashed lines are drawn to guide the eye.

determining the exact source activity. Since the used well counter lacks specifications of its accuracy, further investigations of the different results could be obtained by remeasuring the source activity using a device with specified accuracy (i.e. a preclinical PET scanner) and repeating the performed simulations and measurements after developing a more elaborate and precise construction for placing the source at the specified positions.

Using the same source and detector block, a second validation measurement was performed as illustrated in Figure 3.6b. With the source positioned at a fixed distance of 4 cm between the center of the source and the nearest detector surface, up to three Printed Circuit Board (PCB) layers with a thickness of 1.5 mm each, were placed between the source and the detector. After adding single PCB layers to the setting, increasing attenuation, the count rate measured by the detector was examined. The PCB material is modeled in the simulations by a combined material made of the woven glass and epoxy of a type FR-4 PCB and copper with a combined density of $2.03\,\mathrm{g\,cm^{-3}}$ evenly distributed inside the PCB volumes. The resulting simulated and measured count rates are shown in Figure 3.8. Similar to the previous experiment, both simulations are in very good accordance with each other, with GATE resulting in slightly higher count rates than PETSim. The simulations again overestimate the measured count rates by between 13 % and 16 %. A possible improved realization of the measurement and simulations as described for the previous validation experiment could help in further understanding the differences between measured and simulated count rates. Additionally, the effects of more elaborate modelings of the PCB plates in the simulations could be investigated.

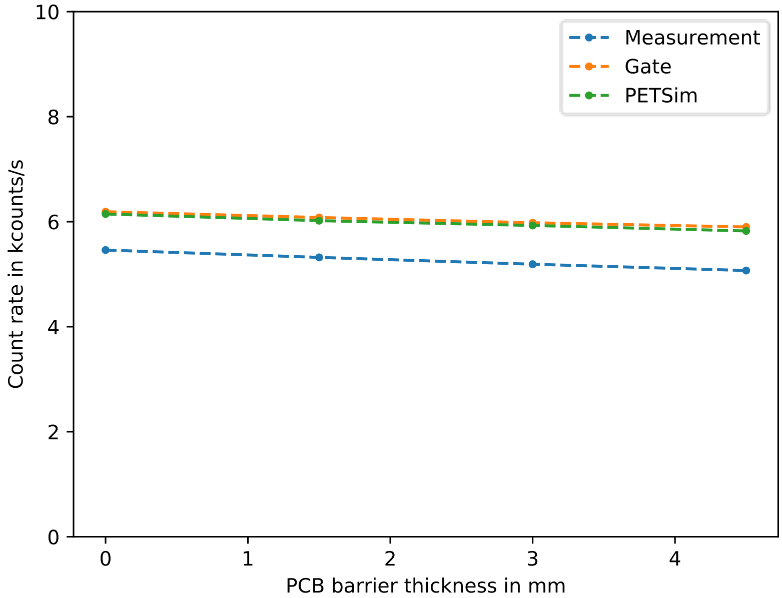

Figure 3.8.: Comparison between measured and simulated count rates depending on the PCB barrier thickness using a fixed source distance of 4 cm. Simulations were performed using the GATE and PETSim simulation tools. Dashed lines are drawn to guide the eye.

3.4. PET Scanner Performance Characteristics

Today, many PET systems from multiple manufacturers exist on the market. To make these systems comparable to each other, the National Electrical Manufacturers Association (NEMA) publishes standardized sets of performance measurements for different types of PET scanners. Although the breast PET/MR insert is developed for clinical use cases, its dimensions resemble rather the small animal PET scanners used for preclinical studies taking place before clinical trials can begin, rather than clinical scanners. Therefore, the performance measurements introduced in this section are based on the "NEMA Standards Publication NU 4-2008" for small animal positron emission tomographs [NEM08] with adjustments accounting for the different usage scenarios.

3.4.1. Sensitivity

The sensitivity of a PET scanner is defined as the amount of coincidence counts per time and source activity and describes the PET scanner capability of detecting coincident events of 511 keV annihilation photons. It depends on the solid angle occupied by scintillator material, the detection efficiency and the attenuation depending on the scanned living subject (or object responding similar to a living subject, referred to as phantom). An analytical representation of the sensitivity S can be given for cylindrical scanners as

$$S = \frac{A \cdot \epsilon^2 \cdot \gamma}{4\pi r^2} \qquad \frac{\text{events}}{\text{s} \cdot \text{Bq}} \tag{3.2}$$

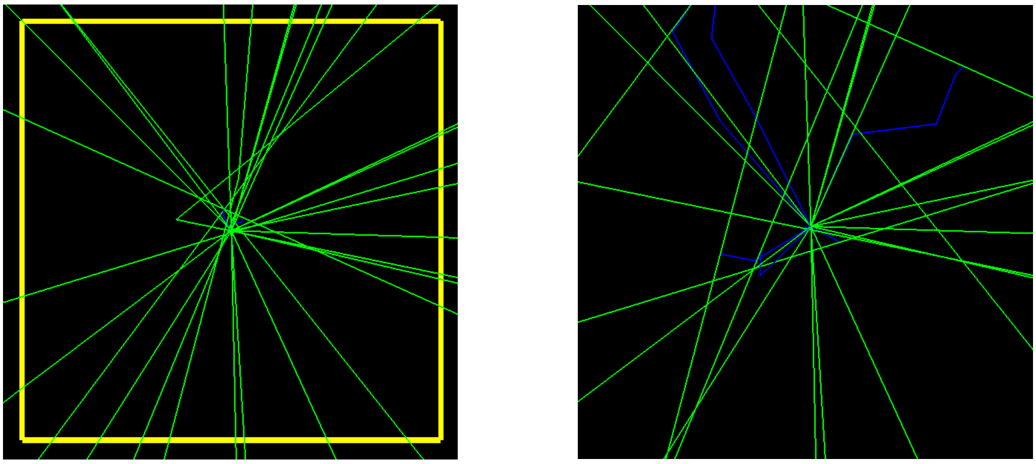

(a) Top view. (b) Zoomed in.

Figure 3.9.: Spherical ^{22}Na gamma source with a radius of 0.15 mm placed inside an acrylic cube with an edge length of 10 mm (yellow wireframe). In the zoomed view (b), a section around the center with an edge length of roughly 0.8 mm is shown. The positrons emitted on 10 simulated decays (blue trajectories) are confined inside the acrylic cube due to their mean free path being much shorter than the cube dimensions. Gamma-ray trajectories are visualized in green color.

with the area of detector material A, the detection efficiency ϵ, the attenuation factor γ and the scanner radius r [Bud98].

For measuring the sensitivity of a PET scanner, the NEMA standard [NEM08] requires a ^{22}Na gamma source with a maximum concentrated activity extent of 0.3 mm placed inside an acrylic cube with an edge length of 10.0 mm ensuring positron annihilation within the source. The source activity shall be low so that the dead-time losses as well as the random coincidence rate are below or equal to 5 % of the total event rate. While transaxially centered, the source is moved in steps from the axial center outwards to the edge of the field-of-view, then starting again from the center towards the other end. At each step the source shall be measured for the duration needed to get 10 000 true coincidence events at the transaxially and axially centered point.

The source requested by the NEMA standard is modeled in GATE using a spherical geometry with a radius of 0.15 mm, placed inside an acrylic phantom volume box with a density of 1.2 g cm^{-3} and a length of 10 mm on all sides. The modeled source is shown in Figure 3.9 together with the trajectories of positrons and gamma rays emitted on ten simulated ^{22}Na decays and the subsequent electron-positron annihilations, respectively. To take the finite positron mean free path, the ^{22}Na branching ratio as well as the possible non-collinearity of the emitted photons into consideration, the nuclear decay itself is the starting point of each simulated event, rather than directly creating two anti-parallel (“back-to-back”) 511 keV photons. The source activity is set to 100 000 Bq to obey the required upper limits for the random coincidence rate and dead-time losses. For improved statistics, a simulation time of 30 s is used for each individually measured point, resulting in at least 80 000 detected coincidence events for the central point of the probed detector geometries.

In contrast to small animal scanners, the positions of the phantom and source in the breast PET insert are not confined to a bed inside the cylinder, but might be placed anywhere in the field-of-view including varying positions along the y-axis, which corresponds to the axis orthogonal to the patient bed. To reflect the increased interest of imaging sources distributed over the complete scanner interior space compared to the situation covered by the NEMA NU 4 standard, the sensitivity is calculated for additional source movements along the transaxial x- and y-axes. Additionally, the simulated sensitivity is visualized using three-dimensional plots for the three orthogonal planes spanned along the the axes of the used coordinate system.

The system sensitivity can be calculated from the simulated or measured data via

$$S_i = \left(\frac{R_i - R_{B,i}}{A_{cal}}\right) \tag{3.3}$$

at the slice i with the event rate R, the source activity at time of the measurement A_{cal} and the background rate R_B [NEM08] with a vanishing background rate in case of simulated data.
The absolute sensitivity given as a unit-less percentage can be obtained by considering the ^{22}Na branching ratio of 0.9060 between the beta plus decay mode and the competing electron capture decay mode:

$$S_{A,i} = \frac{S_i}{0.9060} \cdot 100 \qquad \text{[NEM08]}. \tag{3.4}$$

3.4.2. Spatial Resolution

Spatial resolution characterizes the PET scanner ability to produce reconstructed images allowing to distinguish between regions of the scanned object differing in source activity. It is a measure for the minimum distance of two point sources that allows them to be discriminated in the final image. A PET scanner spatial resolution can be determined by imaging a point source or thin line source and measuring the Full Width at Half Maximum (FWHM) of a Gaussian fit of the resulting profile [BTVM05].

The spatial resolution of a PET system is influenced by the following list of physical effects [Mos11]:

- **Detector size:** The finite width of the detector crystals usually marks the dominant factor due to the undetermined position of photon interactions in the scintillator material and the solid angle coverage of the finite crystal face.
- **Positron range:** Before annihilating, the positrons travel a finite distance depending on the material surrounding the activity and the positrons' initial kinetic energy depending on the source isotope. The positron trajectories are illustrated in blue color in Figure 3.9b.
- **Non-collinearity**: The 511 keV annihilation photons are emitted in opposite directions with an angle of 180° ("back-to-back") in the positronium rest frame. Residual kinetic energy of the positron leads to non-collinear annihilation photons in the lab frame and therefore in a line of response (LOR) departing from the actual position of annihilation. This effect increases linearly with the scanner radius.

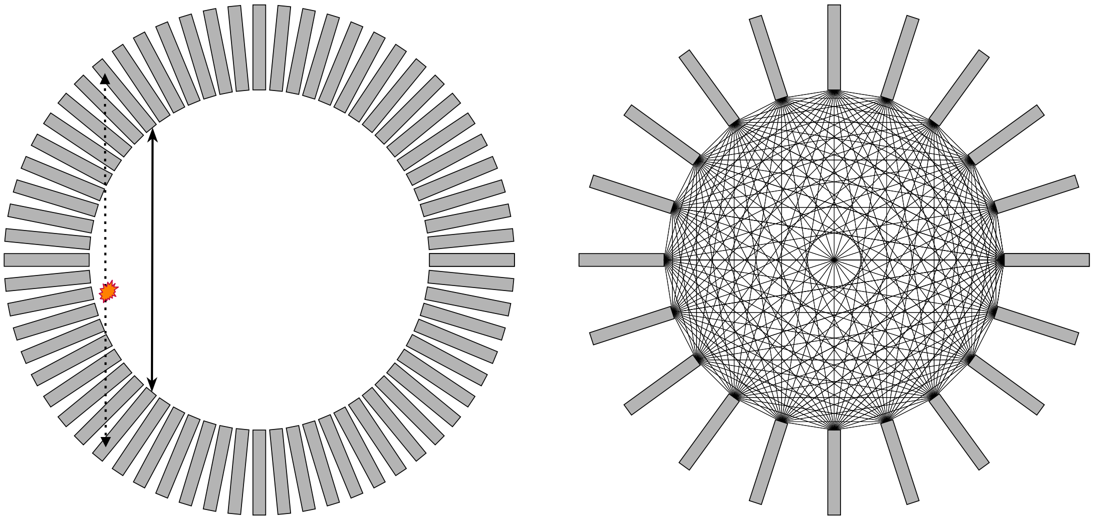

(a) Radial elongation.

(b) Sampling error.

Figure 3.10.: Two effects deteriorating spatial resolution: Radial elongation (a) occurs because conventional PET scanners detect only the crystal in which the photon interaction took place and do not obtain information about the exact position of interaction in the crystal. With the photon trajectories (dotted line) penetrating multiple crystals before interacting, the reconstructed line of response (continuous line) shows a parallax error. The sampling error (b) is caused by an imperfect sampling due to the finite crystal width. For this ring detector built of 20 individual crystals, multiple areas with bad sampling exist in the field of view while other positions show good sampling, such as the central point or other points circularly arranged around the center.

- **Decoding:** Most PET devices use optical multiplexing with a different amount of photosensors compared to the number of scintillation crystals, instead of reading out every crystal individually. Imperfections in this decoding introduce a constant error.
- **Radial elongation:** In case the incident photon is not perpendicular to the crystal face it might traverse the crystal and finally be detected by another crystal than the one it first impinged. This introduces an error dependent on the scanner radius as well as the radial distance from the source to the center of the detector ring. The radial elongation effect is illustrated in Figure 3.10a.
- **Sampling error:** Single voxels in the detector field-of-view contain different counts of LORs passing through them. The sampling is not uniform due to the cylindrical geometry and the finite width of the crystals. Figure 3.10b shows all valid LORs of an exemplary ring detector with 20 individual crystals. The sampling error increases the above effects by a constant empirical factor.

For a cylindrical PET detector these effects combined can be analytically expressed and the resulting spatial resolution (mm FWHM) approximated as

$$\begin{aligned}\Gamma &= \gamma_{\text{sampling}} \cdot (\gamma_{\text{size}} + \gamma_{\text{range}} + \gamma_{\text{non-collinearity}} + \gamma_{\text{decoding}} + \gamma_{\text{elongation}}) \\ &= 1.25 \cdot \sqrt{\left(\frac{d}{2}\right)^2 + s^2 + (0.0044 \cdot R)^2 + b^2 + \frac{(12.5 \cdot r)^2}{r^2 + R^2}} \end{aligned} \tag{3.5}$$

with the spatial resolution Γ, the crystal width d, the positron range s, the crystal decoding error factor b, the detector ring radius R and the radial distance r from a point source to the center of the detector [Mos11].

A fundamental limit for the spatial resolution of PET imaging can be calculated by assuming a perfect PET scanner with zero width crystals and the point source placed in the center of the detector ring. Equation 3.5 then reduces to

$$\Gamma = \sqrt{\gamma_{\text{positron\_range}} + \gamma_{\text{non-collinearity}}} = \sqrt{s^2 + (0.0044 \cdot R)^2} \quad . \tag{3.6}$$

This yields fundamental limits of 0.67 mm FWHM for preclinical devices and 1.83 mm FWHM for clinical scanners assuming a positron range of 0.5 mm and a minimal required radius of 100 mm for preclinical and 400 mm for clinical systems, respectively [Mos11].

The "NEMA Standards Publication NU 4-2008" for small animal positron emission tomographs describes a measurement procedure for determining the spatial resolution of a preclinical PET scanner to allow comparison of the results between different devices. For this measurement the same source as described in Section 3.4.1 is placed at different locations and scanned until at least 100 000 coincidences are recorded. The source is placed at transaxial distances of 5 mm, 10 mm, 15 mm, 25 mm and at further increments of 25 mm from the transaxial center as long as the source remains in the scanner field-of-view. Two collections of data are performed using these positions, one at the axial center and one at 1/4 of the axial field-of-view towards a scanner edge along the axial direction. Reconstruction is subsequently performed with no smoothing using the analytic filtered backprojection algorithm. For three orthogonal directions the FWHM and the Full Width at Tenth Maximum (FWTM)

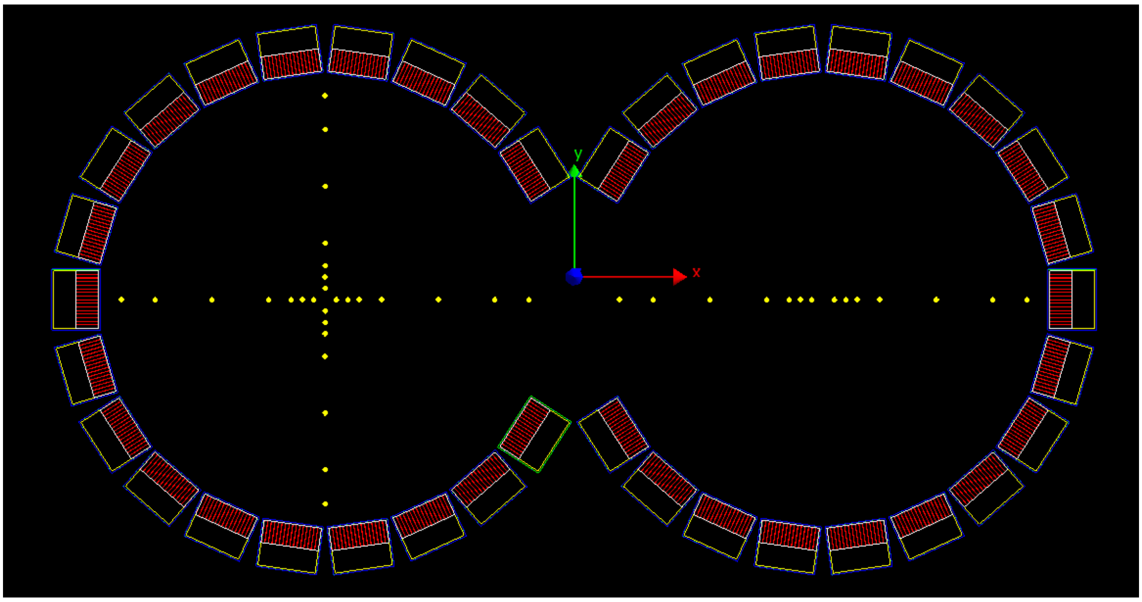

Figure 3.11.: Top view of the probed source placements in the peanut geometry. The central points of the ^{22}Na gamma sources are represented by small yellow spheres. The probed axial positions are at the axial center and at 1/4 off the axial center along the positive z-axis. The red, green and blue arrows point along the positive x-, y- and z-axes, respectively. The axes central point is displayed at (0 cm, 1 cm, 0 cm) for better visibility of the sources.

are calculated from one-dimensional response functions and reported in a tabular view, which is exemplary given in the standards publication [NEM08].

In order to address the missing constraints of source activity positions inside the breast PET insert and the missing symmetries of a cylindrical geometry, additional placements of the ^{22}Na gamma source are simulated and investigated. The transaxial source distances described in the NEMA NU 4 standard are repeated along the positive and negative x-axis as well as along the positive and negative y-axis. An additional position close to the radial edge of the field-of-view is added to the measurements along each direction. The studies along the x-axis are extended into the second field-of-view to verify that the symmetry of the different geometries is reflected in the simulation results. The probed source positions are shown using the example of the "peanut" geometry in Figure 3.11.

Iterative reconstruction allowing for generic detector layouts is performed instead of filtered backprojection using CASToR ("Customizable and Advanced Software for Tomographic Reconstruction") [MSB+18] in version 2.0. The iterative MLEM optimization algorithm [SV82], which is the CASToR default setting, is used with two iterations of 24 subsets together with an accelerated Siddon projector [JSS+98]. Figure 3.12 shows an exemplary reconstructed image of a point source. To comply with the NEMA NU 4 requirement on the minimum recorded counts, the source is scanned for 100 s for each position together with a "warm" background of reduced activity filling the field-of-view.

For determining the spatial resolution from a reconstructed image the "IAEA-NMQC

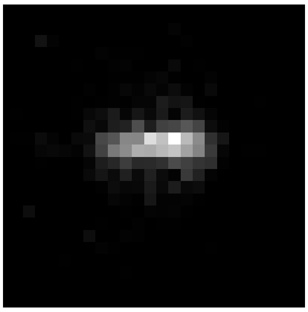

Figure 3.12.: Reconstructed image of an exemplary point source using the CASToR reconstruction software. Two iterations of 24 subsets are performed using the iterative MLEM optimization algorithm and an accelerated Siddon projector.

Toolkit"[3] installed as a plugin into the "Fiji" [S+12] distribution of "ImageJ" [SRE12] is used. The voxel size and the slice thickness of the reconstructed image are set to 0.5 mm to ensure that multiple voxels are spanned by the Gaussian fit used to determine the spatial resolution. For a few single source positions the automatic determination of the spatial resolution failed and "AMIDE" [LG03] was used in these cases to determine the resolutions manually.

In the performed simulation studies the decoding error vanishes due to an individual crystal readout. Because the final readout electronics design is dependent on the simulation results, optical multiplexing is not added to the simulated readout and digitizer chain. The simulated spatial resolution values therefore represent an ideal case without decoding errors and might deteriorate with the use of optical multiplexing methods. Future optimizations to the reconstruction method could potentially allow to further improve the spatial resolution.

3.4.3. Maximum Count Rate

For the development of the detector hardware and dimensioning of the readout electronics taking place at the same time as the software-based simulation studies, it is important to have a sound assumption of the highest expected count rates. The count rates, defined as the number of detected single events per second, is calculated per detector block as well as per ring of blocks to provide a basis for the decision for or against multiplexing multiple detector blocks.

A previous breast PET/MR measurement series with five scanned patients [S+16] measured a worst-case uptake of 1.5 MBq in the human breast using an FDG tracer[4]. Therefore, simulations are performed counting single events using a ^{18}F source with an activity of 1.5 MBq confined in a sphere with 0.15 mm radius placed inside a cube consisting of human breast tissue with an edge length of 10 mm. Detector dead time and energy filtering are disabled in order to yield the maximum raw singles count rate. The source is moved from the center of the field-of-view towards the edges along the x-axis. In order to simulate the maximum expected count rates, the source

[3] https://humanhealth.iaea.org/HHW/MedicalPhysics/NuclearMedicine/QualityAssurance/NMQC-Plugins/

[4] Internal communication with WSIC

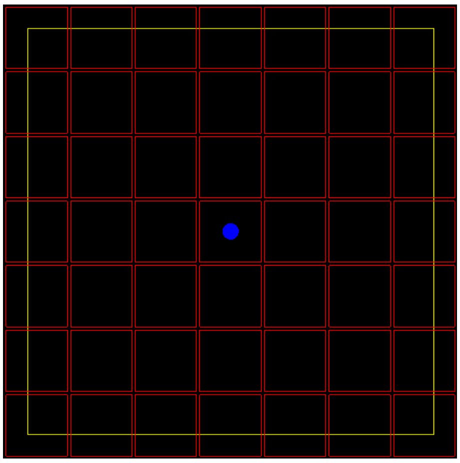

Figure 3.13.: Position of the ^{18}F spherical source (blue) surrounded by a cube consisting of human breast tissue with an edge length of 10 mm (yellow wireframe). The center of the spherical source is placed centered in front of the face of one of the four crystals located at the detector block center to ensure simulating the maximum possible count rate per detector block. For better visibility the spherical source is not true to scale.

is placed slightly off the x-axis in y and z directions in such a way that the center of the ^{18}F spherical source is located in front of the center of a crystal as illustrated in Figure 3.13.

3.5. Simulation Studies of Breast PET/MR Inserts

Unmodified reuse of the patient bed framing the planned PET breast insert shown in Figure 3.5 puts two main constraints on the possible detector geometries of the insert device: The PET breast insert must be small enough to fit into the unused volume between the upper and lower level of the patient bed, and the volume enclosed by the coils used for magnetic resonance imaging should not be filled with detector blocks to minimize disturbances of the magnetic field inside the field of view.

Based on the geometries of available preclinical and clinical PET scanners, an ideal breast insert could be built using two cylindrical scanners, each enclosing one of the two fields of view as well as the respective coils. This would make it possible to build on previous experience and existing technology specifically adapted for cylindrical geometries. However, the distance between the upper coils of the patient bed is too small to fit two detector blocks in between based on the anticipated size of the individual detector blocks. Therefore, modifications of the patient bed and the coil placements would be necessary. The simulated performance characteristics of the “two cylinders” geometry are listed in Chapter 3.5.1. Two additional geometries were exemplarily simulated and probed for suitability based on their performance characteristics in the course of this thesis. The “stretched cylinder” and the “peanut” geometries meet the described constraints and allow implementation into the patient bed without the necessity of modifying the coils. The simulation results for the

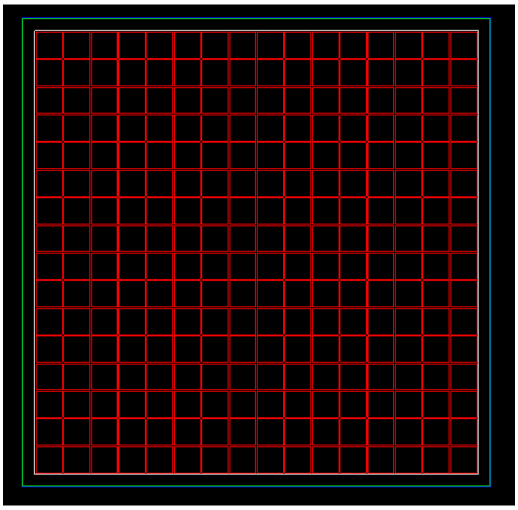

(a) Front view.

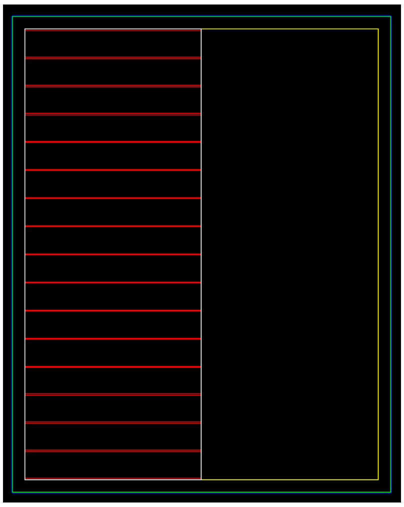

(b) Side view.

Figure 3.14.: Wireframe visualization of the detector block used for the PET simulation studies. This block contains 16×16 crystals with a depth of 10 mm and a crystal pitch of 1.59 mm. The block dimensions are 26.99 mm × 26.99 mm × 21.47 mm including shielding. Crystal edges are shown in red color, the outer edges of the ESR film in white and the detector volume including crystals, photosensors, readout electronics and cooling elements in yellow. The ABS layer and copper shielding are shown in green and blue, respectively.

"stretched cylinder" and the "peanut" geometries are described in Chapter 3.5.2 and 3.5.3, respectively.

All of the simulated PET breast insert devices are based on the same detector block, which is currently under development, and the specifications, depending also on the results of the performed simulation studies, therefore represent realistic assumptions based on the current state of development and are possibly subject to change.

Each simulated detector block is assembled of a 16×16 grid of individual 10 mm long Lutetium Oxyorthosilicate (LSO) crystals separated by 80 µm thick Enhanced Specular Reflector (ESR) films. The 1.51 mm side length of the square crystal front faces result in a crystal pitch of 1.59 mm. An additional 10 mm long volume housing the Silicon Photomultipliers (SiPM), readout electronics and cooling elements is placed behind the crystal block. Since the details of this detector part are not finalized yet, a material with a density of $2.03\,\mathrm{g\,cm^{-3}}$ combining the woven glass and epoxy of a FR-4 Printed Circuit Board (PCB) together with copper is assumed for this volume. The detector blocks are wrapped in a 0.7 mm thick layer of Acrylonitrile Butadiene Styrene (ABS) and an additional 35 µm thick copper layer for shielding against the magnetic field of the MR. Combining all individual volumes, the detector block dimensions result in a square front face with a side length of 26.99 mm and a depth of 21.47 mm. A visualization of this detector block modeled in GATE is shown in Figure 3.14.

The estimated readout parameters are implemented in the GATE simulations in order to include the effects of readout and digitization in the simulation results. The "TakeEnergyWinner" readout policy is chosen to map a detected photon to the

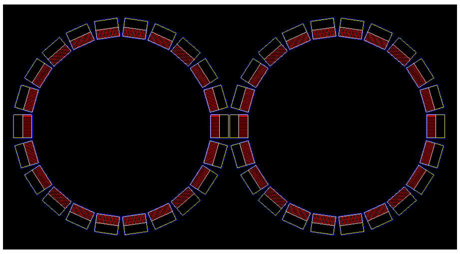

(a) Top view.

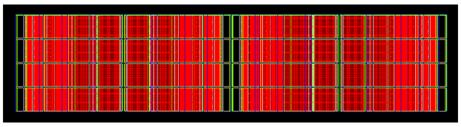

(b) Side view.

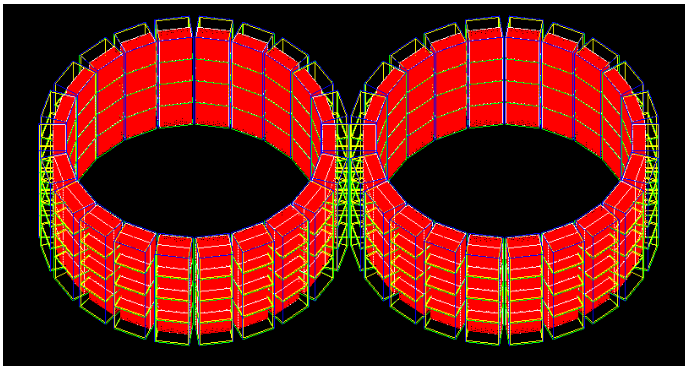

(c) 3-dimensional view.

Figure 3.15.: Detector geometry consisting of two individual cylinders. Each cylinder is composed of four rings with 22 detector blocks each.

crystal with the highest sum of deposited energy across all single hits. A finite energy resolution of 15 % at the reference energy of 511 keV is applied using an inverse square law before filtering out single events with the lower and upper threshold used in the validation experiment of 435 keV and 650 keV, respectively. A dead time of 500 ns is applied in paralysable mode at detector block level resulting in opening a full dead time window for each incident photon including photons hitting the detector block during an existing dead time period. Detected single events in a time windows of 10 ns are combined to coincidences using a coincidence sorter with the "takeWinnerOfGoods" policy configured, resulting in only one considered coincidence per time window, which is set to be the valid singles pair with the highest detected energy.

All PET simulation studies are performed using GATE in version 8.1.p01 with custom patches allowing coincidence sorting for arbitrary geometries and the "emstandard_opt3" physics list configured. The GATE installation was compiled against Geant4 in version 10.4.2. Before reconstruction, the position and orientation of every crystal is calculated and saved into a Lookup Table (LUT) binary file, which can be used as geometry input for CASToR. Simulations and reconstructions are performed on an HP Z840 Workstation with 8 physical CPU cores.

3.5.1. Two Cylinders Geometry

The "two cylinders" geometry shown in Figure 3.15 consists of two individual and separated cylindrical PET scanners with a radius of 100 mm from the center of the FOV to the crystal front faces allowing the detector blocks to be outside of the coils included in the patient bed. The two cylinders do not operate in coincidence with each other. Therefore, a coincident event with one single event detected by the left cylinder and the other photon impinging on a crystal in the right cylinder is marked as two single events. Each cylinder contains four detector rings with a pitch of 27 mm with 22 detector blocks per ring resulting in a total number of 22 528 individual LSO crystals per cylinder and consequently 45 056 crystals for the complete setup. With the anticipated size of the readout electronics and cooling elements already considered inside each detector block, the two individual cylinders are assembled without additional space between them. The minimum needed distance between the left and right coils to mount this geometry into the patient bed is therefore $2 \cdot l = 42.94$ mm with the detector block length l. Since the distance of the upper coils measures roughly 2 cm, structural changes of the patient bed would be necessary.

The simulated sensitivities are shown in Figure 3.16 for multiple source positions and source movements across different directions in the field of view. Simulations are performed for the cylinder positioned along the negative x-axis with the central point located at $(-120.75, 0, 0)$. Due to the reflection symmetry of the geometry, the results also apply to the cylinder located along the positive x-axis. Statistical errors are calculated for the resulting sensitivity for every source position using Equation 2.9 and added to the figures. Due to the long simulation time of 30 s the statistical error bars are confined in the area filled by the individual points and therefore not visually distinguishable. A sensitivity of 3.79 % is found in the center of the cylinder which strongly declines towards the edges of the field of view along the axial direction while increasing along the radial directions. Using Equation 3.4, the absolute sensitivity at the center of the field of view is calculated to 4.18 %. The cylindrical symmetry is clearly reflected by the sensitivity results. The local maxima and minima seen for source positions along the x- and y-axes are due to the gaps between the individual detector blocks of the scanner rings.

Figures 3.17 and 3.18 show the values of the simulated spatial resolution for source positions along the x-axis and y-axis, respectively. Since errors of the spatial resolution results are hard to pinpoint exactly due to the iterative reconstruction introducing errors depending on the applied algorithm, the specified number of iterations and subsets, the simulated geometry and recorded coincident events in addition to the statistical error of the Monte Carlo simulation and the uncertainties of the Gaussian fits, no error bars are shown. To obtain a visual estimation of the result fluctuations using the reflection symmetry of the geometry, the source positions in the cylinder along the negative x-axis are simulated again in the other cylinder along the positive x-axis and plotted in combined figures.

For the "two cylinders" geometry non-radial spatial resolutions are better than 1.7 mm FWHM for all investigated source positions and better or equal to 1.5 mm FWHM except for one outlier at $x = 210.75$ mm in the axially centered series of measurements. The spatial resolution along the radial direction shows a strong radial elongation effect with results better than 1.5 mm FWHM near the center and declining resolutions towards the edges of the field of view with results worse than 5 mm FWHM and up to 10 mm FWTM. NEMA NU 4 compatible tabular views of the spatial resolution for a source movement along the x-axis and y-axis are outlined in Tables A.1 and A.2 in the appendix, respectively.

Maximum count rates per detector block and per cylinder ring are depicted in Figure 3.19. For a source with an activity of 1.5 MBq near the center of the field

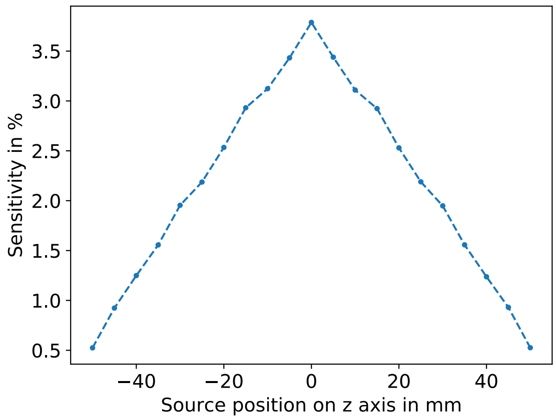

(a) Axial flight through center of FOV.

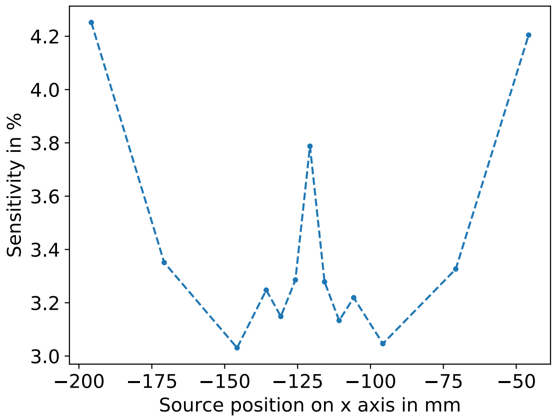

(b) Flight along x-axis through center of FOV.

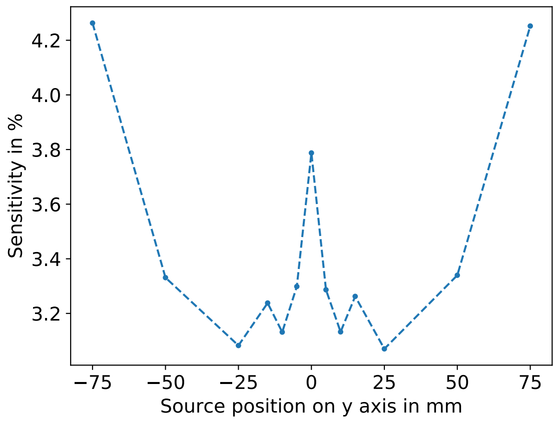

(c) Flight along y-axis through center of FOV.

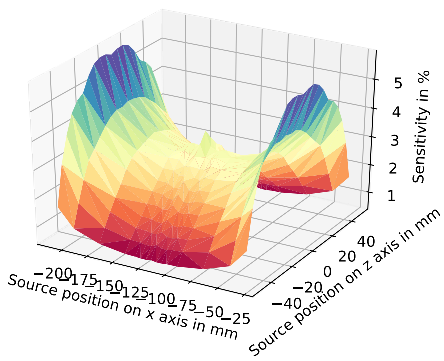

(d) Sensitivity in xz-plane through center of FOV.

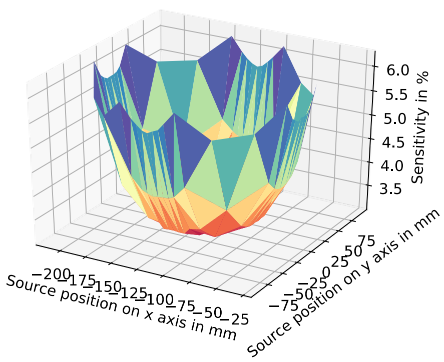

(e) Sensitivity in xy-plane through center of FOV.

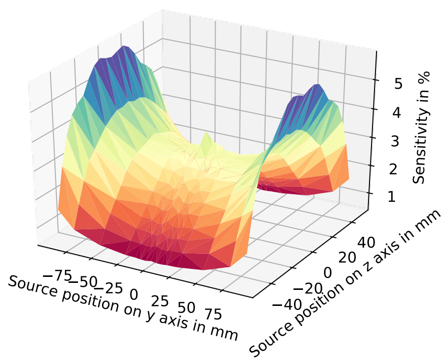

(f) Sensitivity in yz-plane through center of FOV.

Figure 3.16.: Simulated sensitivity of the “two cylinders” geometry. Dashed lines and planes are drawn to guide the eye.

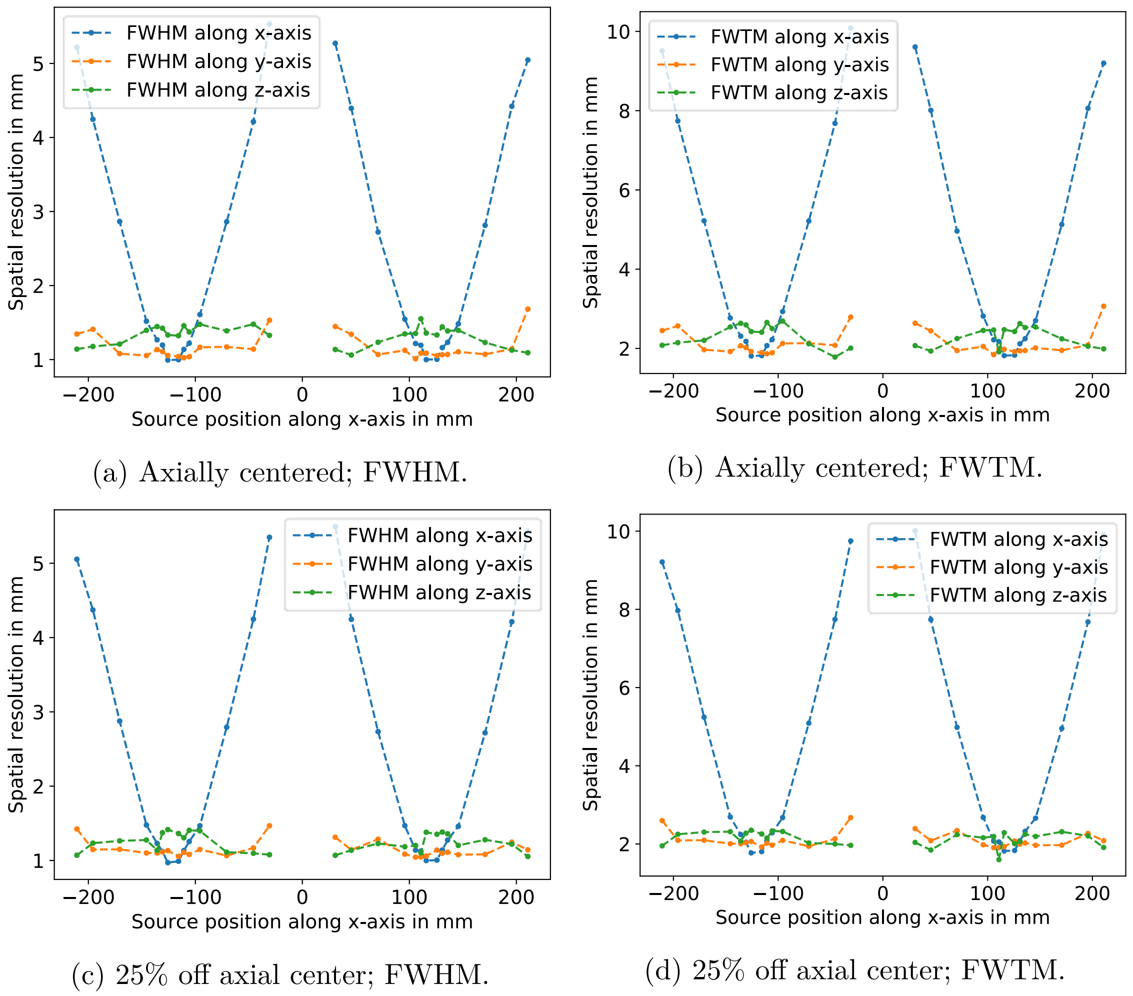

Figure 3.17.: Simulated spatial resolutions of the “two cylinders” geometry for a source moved along the x-axis. Dashed lines are drawn to guide the eye.

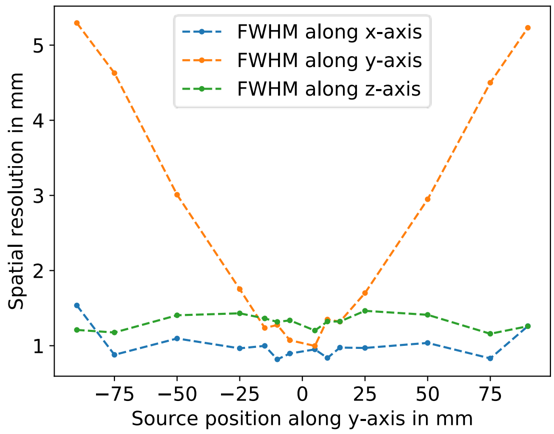

(a) Axially centered; FWHM.

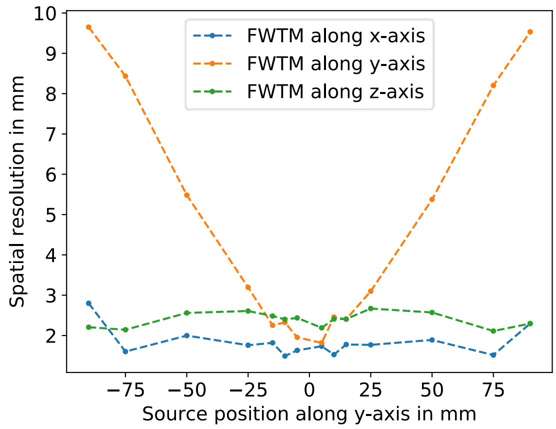

(b) Axially centered; FWTM.

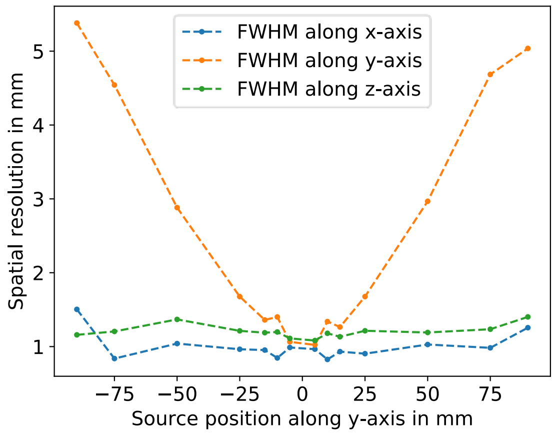

(c) 25% off axial center; FWHM.

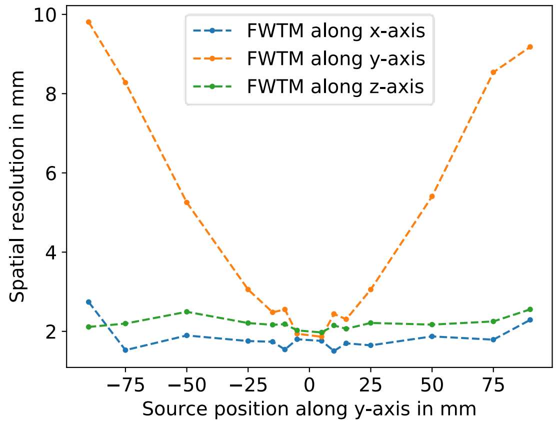

(d) 25% off axial center; FWTM.

Figure 3.18.: Simulated spatial resolutions of the “two cylinders” geometry for a source moved along the y-axis in one of the FOVs. Dashed lines are drawn to guide the eye.

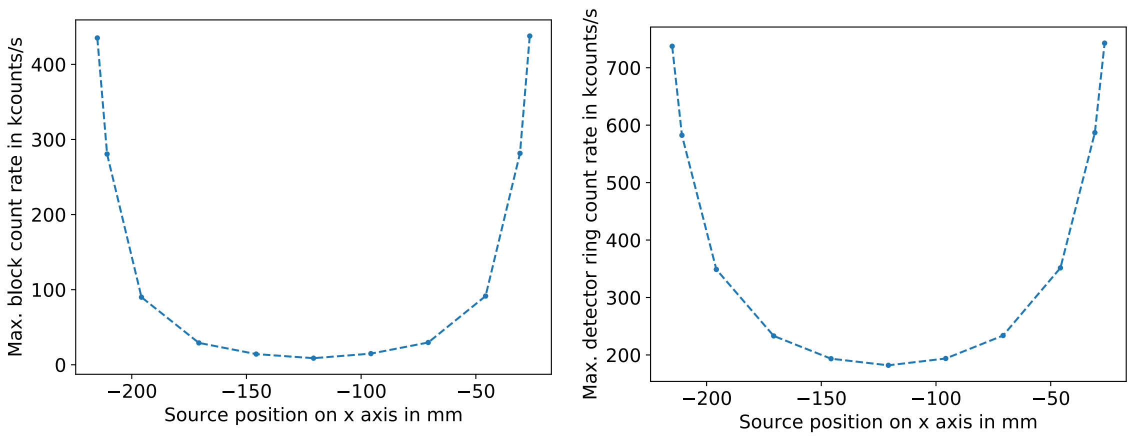

Figure 3.19.: Maximum count rates per block and detector ring of the “two cylinders” geometry for a source flight along the x-axis through the center of the FOV. Dashed lines are drawn to guide the eye.

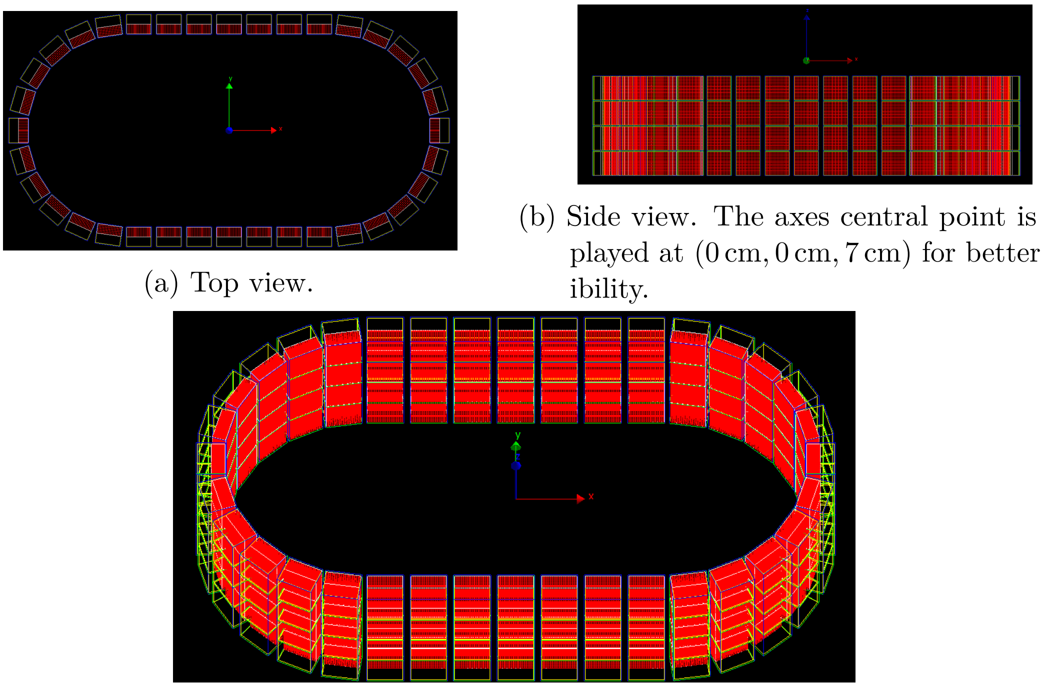

(a) Top view.

(b) Side view. The axes central point is displayed at (0 cm, 0 cm, 7 cm) for better visibility.

(c) 3-dimensional view.

Figure 3.20.: Detector geometry built of two half cylinders connected with two grids of detector blocks. The red, green and blue arrows point along the positive x-, y- and z-axes, respectively.

of view, maximum count rates of 8.7 kcounts s^{-1} and 181.9 kcounts s^{-1} are expected per detector block and ring, respectively. With the growing solid angle coverage of a single detector block and ring for sources closer towards the radial edges of the field of view, the expected maximum count rates rise until maximal values of 438 kcounts s^{-1} per detector block and 743 kcounts s^{-1} per ring for the closest possible position of the simulated source model with the cubical phantom touching the detector front face and therefore a distance of 0.5 mm between the copper shielding and the center of the ^{18}F activity.

3.5.2. Stretched Cylinder Geometry

Because two detector blocks do not fit between the upper coils of the patient bed, the alternative "stretched cylinder" geometry is developed as illustrated in Figure 3.20, allowing the PET insert to be mounted inside the patient bed without changes. The same cylinder as in the "two cylinders" geometry with four rings containing 22 detector blocks each and a distance between the center of the FOV and the crystal front faces of 110 mm is divided into two half cylinders and filled up with two grids of 4×7 detector blocks each at the center. This results in a total number of 36 864 individual LSO crystals assembled in 144 detector blocks. A distance of 220 mm between the centers of both fields of view allows the "stretched cylinder" geometry to fully enclose the area of interest spanned by the patient bed coils.

The resulting sensitivities for the "stretched cylinder" geometry are depicted in Figure 3.21 for multiple flights through the center of one field of view located at $(-110, 0, 0)$ along multiple directions together with three-dimensional plots visualizing

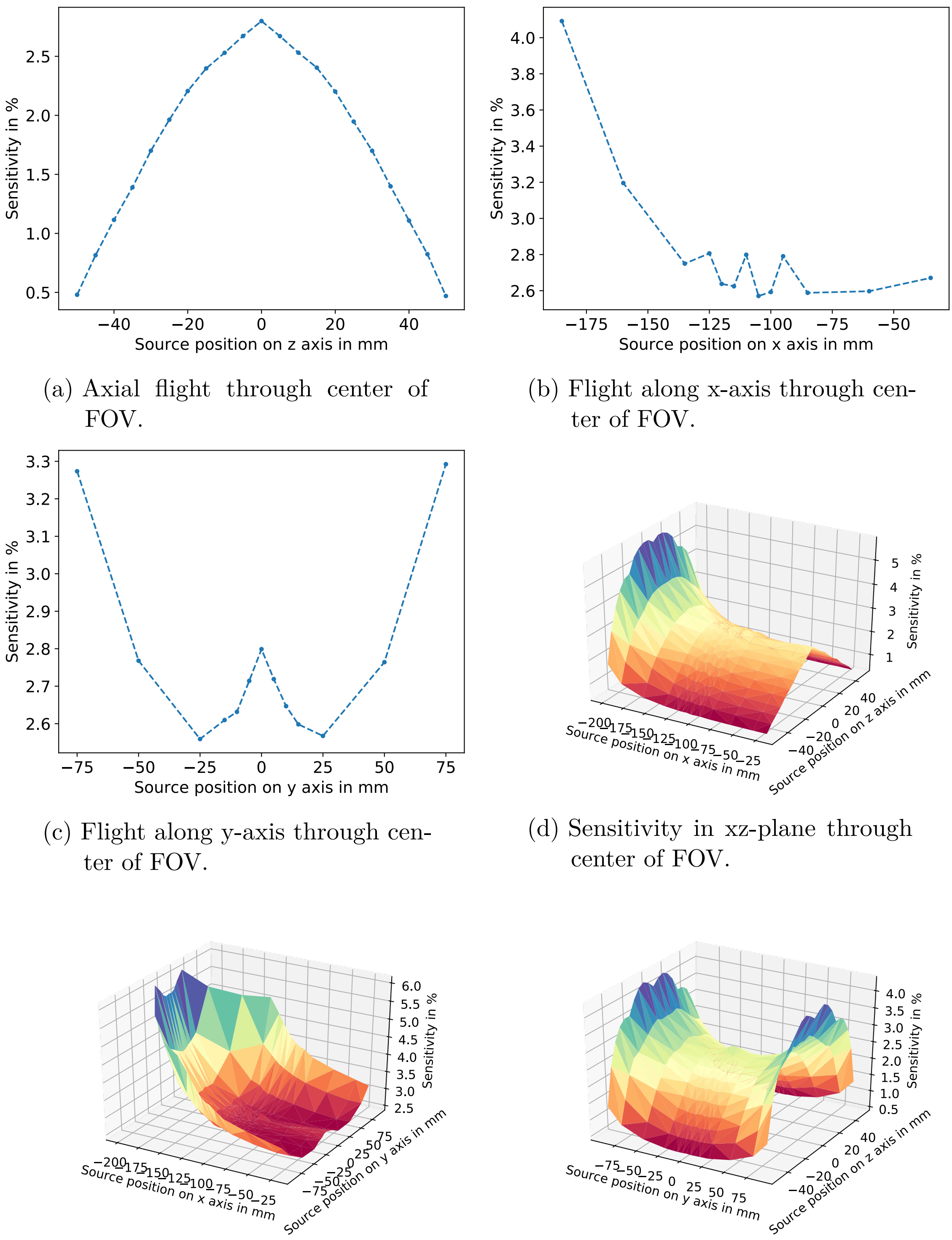

(a) Axial flight through center of FOV.

(b) Flight along x-axis through center of FOV.

(c) Flight along y-axis through center of FOV.

(d) Sensitivity in xz-plane through center of FOV.

(e) Sensitivity in xy-plane through center of FOV.

(f) Sensitivity in yz-plane through center of FOV.

Figure 3.21.: Simulated sensitivity of the "stretched-cylinder" geometry. Dashed lines and planes are drawn to guide the eye.

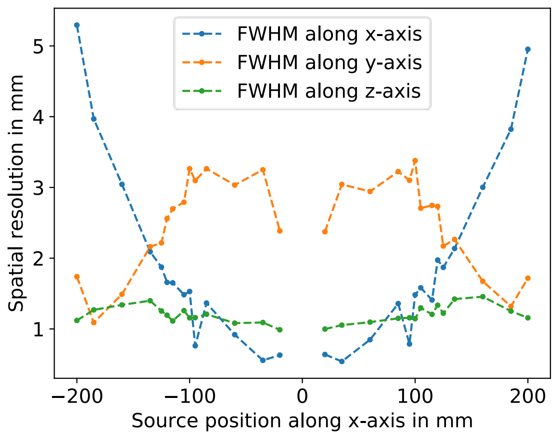

(a) Axially centered; FWHM.

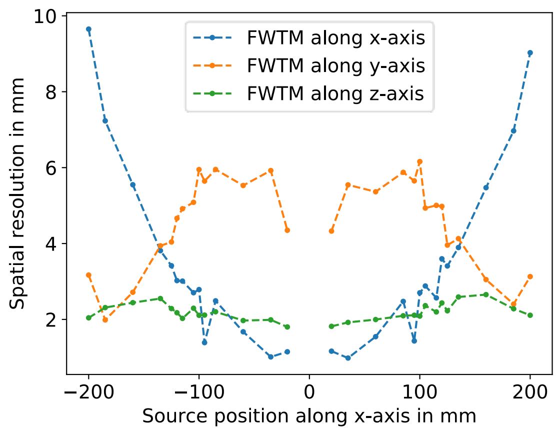

(b) Axially centered; FWTM.

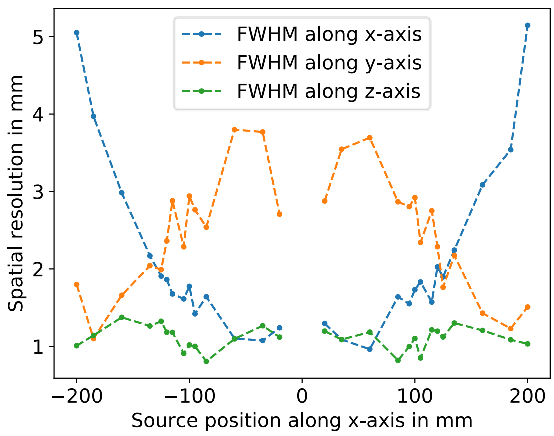

(c) 25% off axial center; FWHM.

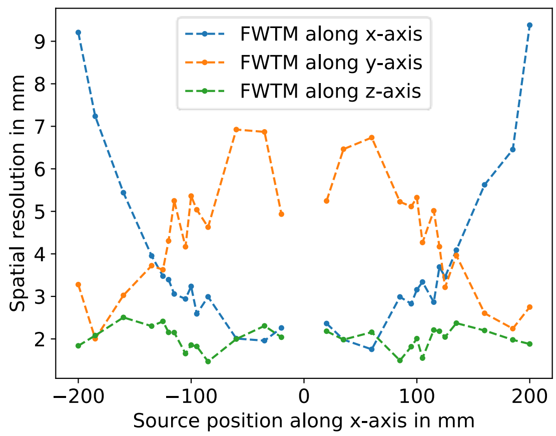

(d) 25% off axial center; FWTM.

Figure 3.22.: Simulated spatial resolutions of the "stretched cylinder" geometry for a source moved along the x-axis. Dashed lines are drawn to guide the eye.

the sensitivity variations in different planes inside the field of view. The sensitivity at the central point of the field of view amounts to 2.80 %, which corresponds to an absolute sensitivity of 3.09 %, which is 26 % lower than the absolute sensitivity at the corresponding position for the "two cylinders" geometry due to the lower solid angle covered by sensitive detectors. While the simulated sensitivities show symmetric behavior along the axial direction and the y-axis, the sensitivities along the x-axis are not individually symmetric for both single fields of view reflecting the different symmetric properties of the geometry compared to the "two cylinders" solution. In particular the sensitivity from the center of the field of view to the center of the whole geometry along the x-axis is not increasing beyond 2.8 % as shown in Figure 3.21b.

The simulated spatial resolution for source movements along the x-direction are shown in Figure 3.22 for an axially centered source and a source placed 25 % off the axial center along the z-direction. For the outer edges of the fields of view, where the source is placed close to the half cylinders, the spatial resolution behavior resembles the "two cylinders" geometry with a radial elongation effect towards the outer edges. Closer to the central grids of detector blocks, the spatial resolution

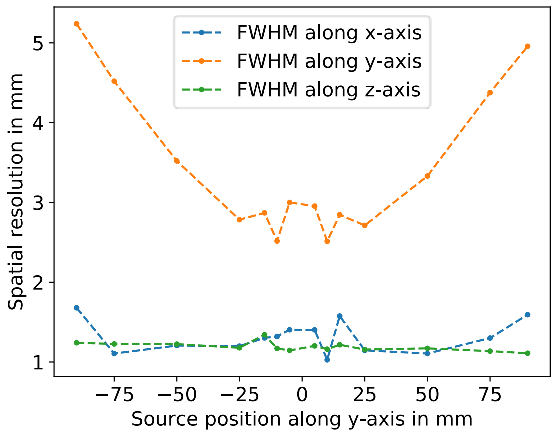

(a) Axially centered; FWHM.

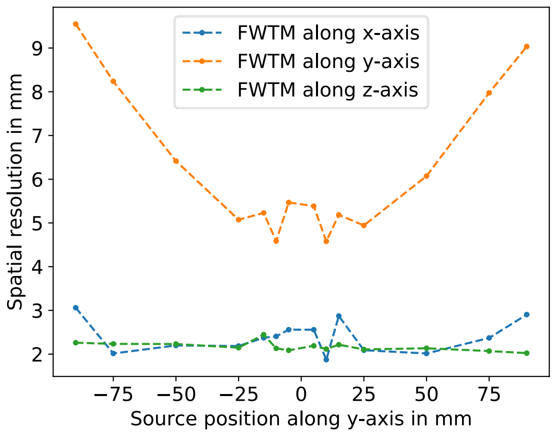

(b) Axially centered; FWTM.

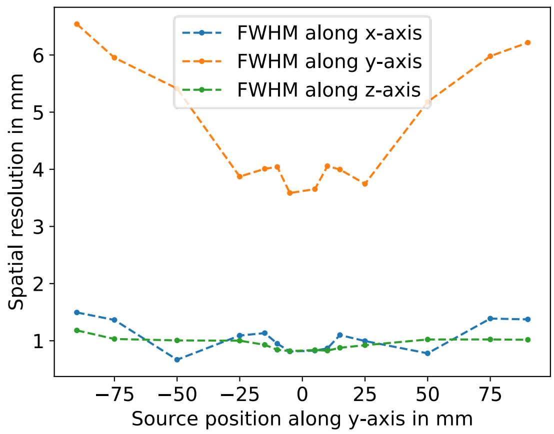

(c) 25% off axial center; FWHM.

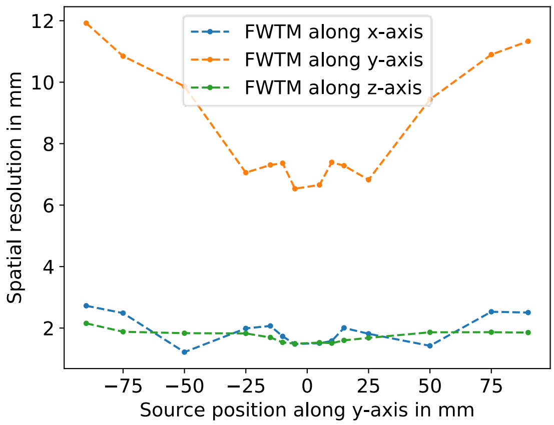

(d) 25% off axial center; FWTM.

Figure 3.23.: Simulated spatial resolutions of the “stretched cylinder” geometry for a source moved along the y-axis in one of the FOVs. Dashed lines are drawn to guide the eye.

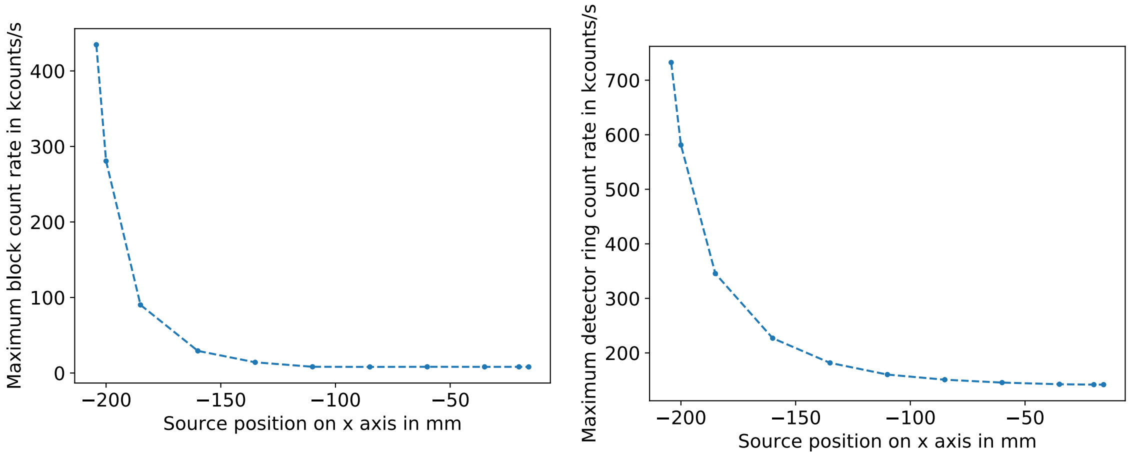

Figure 3.24.: Maximum count rates per block and detector ring of the "stretched-cylinder" geometry for a source flight along the x-axis through the center of the FOV. Dashed lines are drawn to guide the eye.

along the y-direction strongly deteriorates while the radial component improves. The two-dimensional grids at the center of the geometry show a good resolution along the x- and z-directions, but a parallax error along the direction of the crystals, resulting in a degraded spatial resolution of 3 mm and worse along the y-axis for most source positions towards the inner edge of the field of view.

The spatial resolution for a source flight along the y-direction as depicted in Figure 3.23 shows a symmetric radial elongation effect towards the edges comparable to the "two cylinders" geometry. Due to the grids of detector blocks yielding limited depth information, the resolution along the y-direction is between 2.5 mm and 3.0 mm towards the center of the field of view. Tables A.3 and A.4 in the appendix list the spatial resolution values in a NEMA NU 4 compatible view for a source flight along the x-direction and along the y-direction, respectively.

The maximum count rates per detector block and detector ring are shown in Figure 3.24 for the "stretched cylinder" setup. For this simulation, detector blocks with the same axial position are combined to a detector ring, thus resulting in four individual rings for the complete geometry with each ring containing 36 blocks. Because for sources near the front face of a detector the expected count rate for the most frequently hit detector block is predominantly given by the single block properties and not the geometry, the results for the "stretched cylinder" geometry are similar to the other simulated geometries for positions near the outer edge of the field of view at the negative x-axis. At the center of the field of view a maximum count rate of 8.3 kcounts s^{-1} is expected per detector block and 160 kcounts s^{-1} for the most frequently hit detector ring. Although the individual detector rings contain more blocks than the rings of the "two cylinder" geometry, the simulated maximum count rate per detector ring of 733 kcounts s^{-1} for a source position at the outer edge of the field of view at the negative x-axis is lower due to the smaller solid angle occupied by the blocks forming the detector ring.

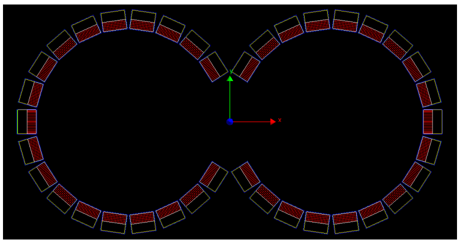

(a) Top view.

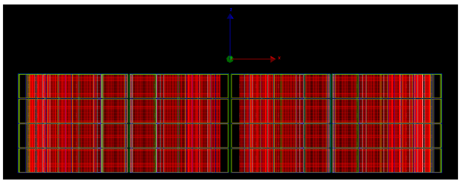

(b) Side view. The axes central point is displayed at (0 cm, 0 cm, 7 cm) for better visibility.

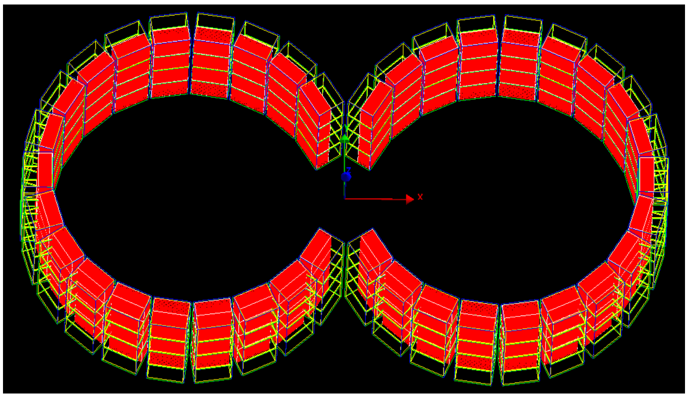

(c) 3-dimensional view.

Figure 3.25.: Detector geometry built of two cylinders with the detector blocks overlapping in the center removed. The red, green and blue arrows point along the positive x-, y- and z-axes, respectively.

3.5.3. Peanut Geometry

The “peanut” geometry represents an alternative detector setup fitting into the patient bed without modification. The “two cylinders” geometry is used as a starting point to build this alternative setup. Both cylinders are pushed together until a distance of 220 mm between the centers of the cylinders is reached. Due to the central detectors now overlapping each other, three vertical lines of detector blocks are removed from each cylinder. This geometry visualized in Figure 3.25 results in 152 detector blocks with a total of 38 912 LSO crystal units.

The simulation of the sensitivity at the center of the field of view located at $(-110, 0, 0)$ results in a sensitivity of 3.42 %, which corresponds to an absolute sensitivity of 3.77 %. Therefore, the missing detector blocks between the two fields of view lead to a reduction of the absolute sensitivity of about 9 % at the center of the individual fields of view. The simulated sensitivities for multiple positions in the field of view are shown in Figure 3.26. For the outer parts of the probed positions the sensitivity behavior is similar to the results of the “two cylinders” geometry. Major differences can be observed for source positions near the symmetry plane due to the missing detector blocks, which is well recognizable in the three-dimensional plot showing the sensitivities in the xz-plane in Figure 3.26d. For the simulated source position on the x-axis closest to the symmetry plane this results in a sensitivity drop of about 19 % compared to the “two cylinders” setup.

The simulated spatial resolutions for a source movement along the x-axis axially centered as well as 25 % off the axial center are depicted in Figure 3.27. Near the centers of the fields of views at $x = \pm 110$ mm the simulations yield spatial resolutions

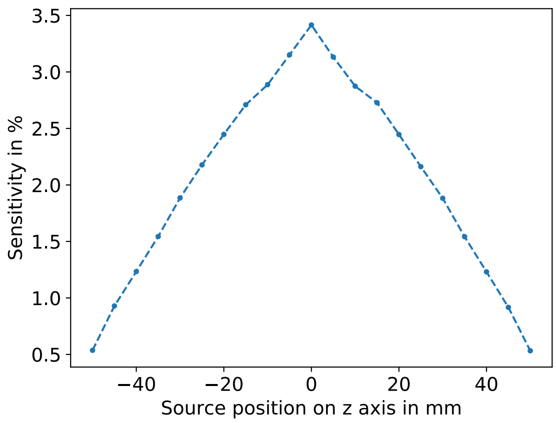

(a) Axial flight through center of FOV.

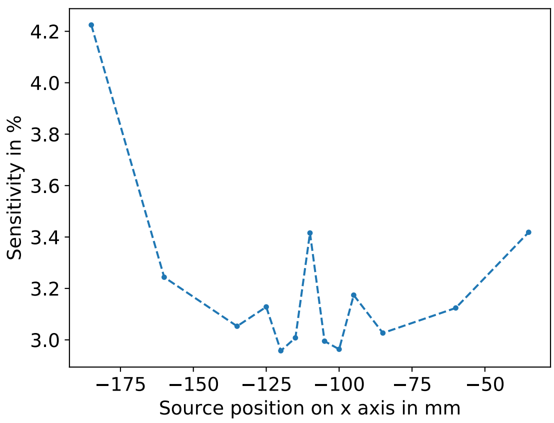

(b) Flight along x-axis through center of FOV.

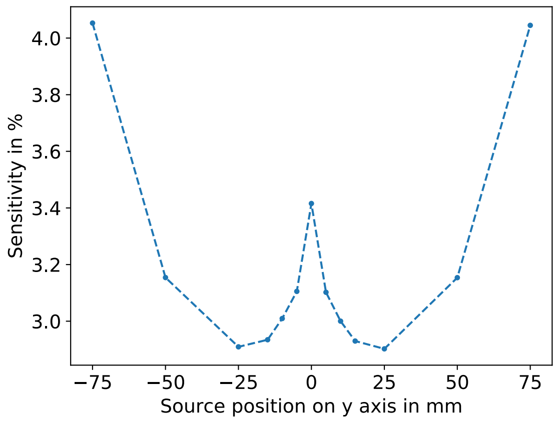

(c) Flight along y-axis through center of FOV.

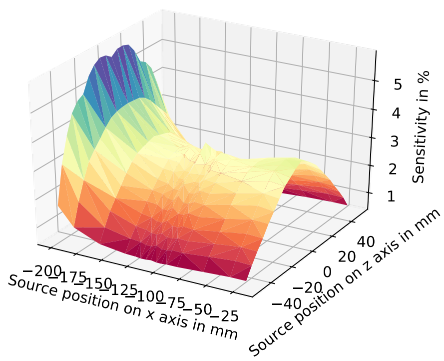

(d) Sensitivity in xz-plane through center of FOV.

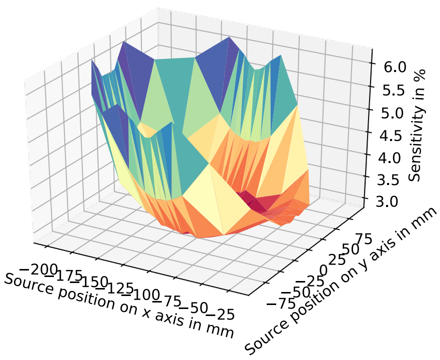

(e) Sensitivity in xy-plane through center of FOV.

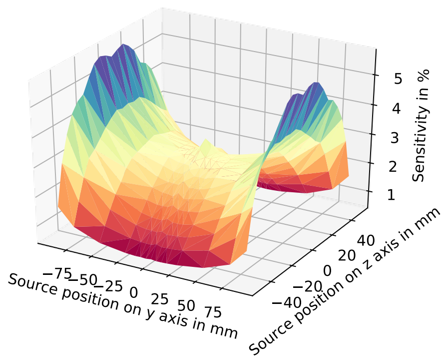

(f) Sensitivity in yz-plane through center of FOV.

Figure 3.26.: Simulated sensitivity of the "peanut" geometry. Dashed lines and planes are drawn to guide the eye.

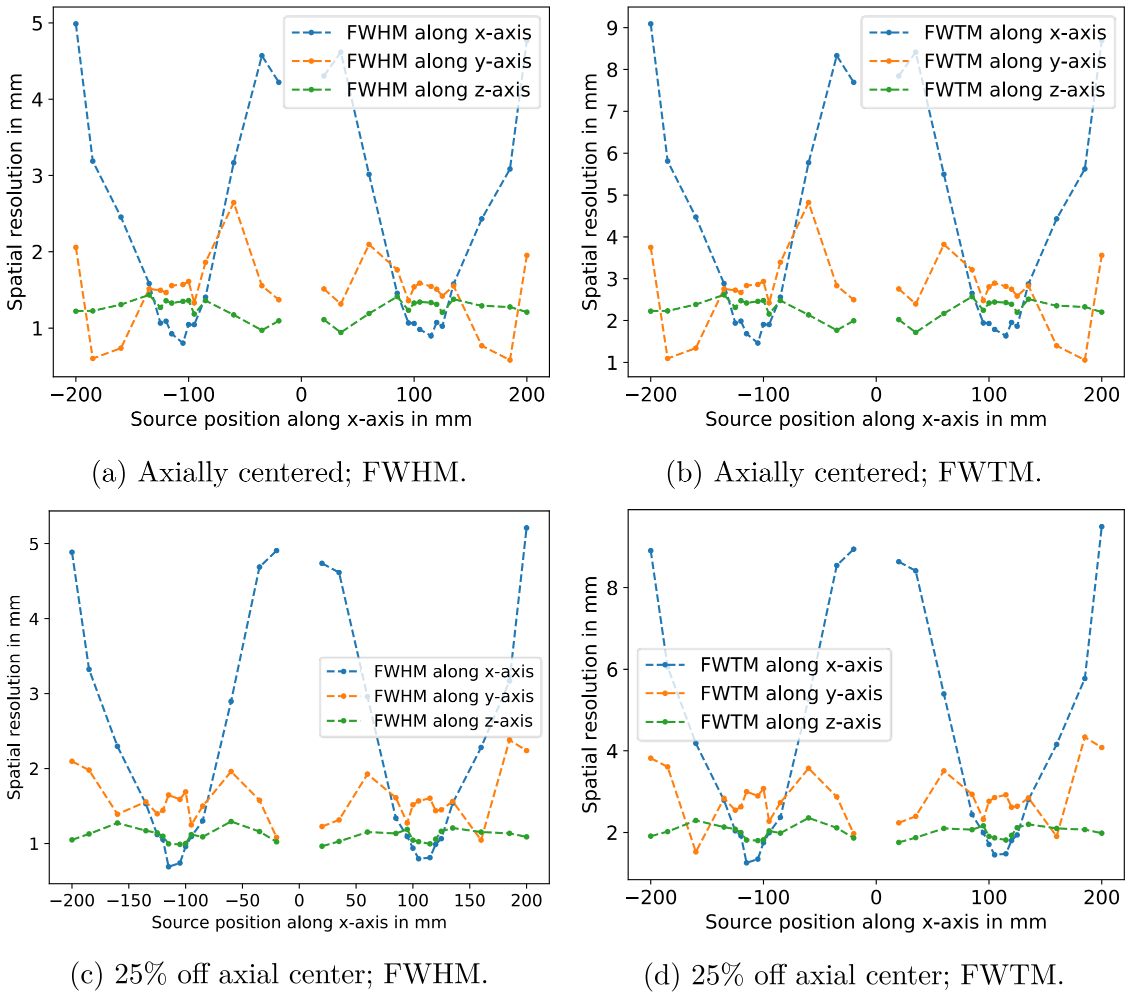

Figure 3.27.: Simulated spatial resolutions of the “peanut” geometry for a source moved along the x-axis. Dashed lines are drawn to guide the eye.

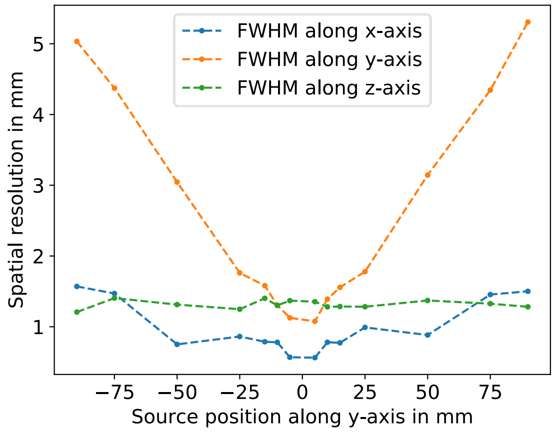

(a) Axially centered; FWHM.

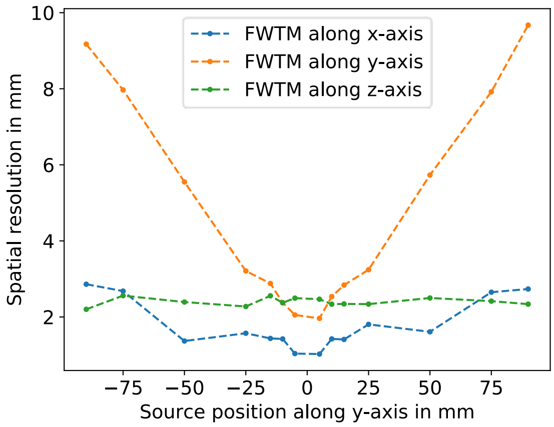

(b) Axially centered; FWTM.

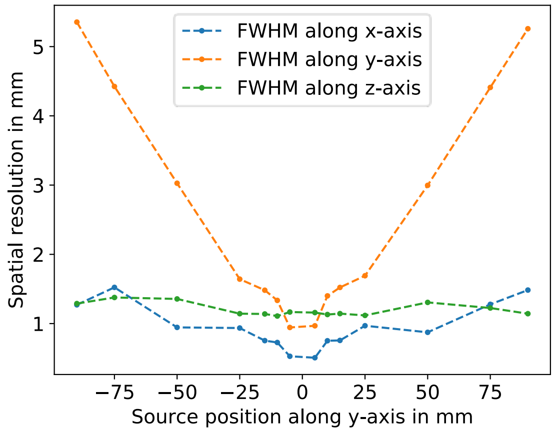

(c) 25% off axial center; FWHM.

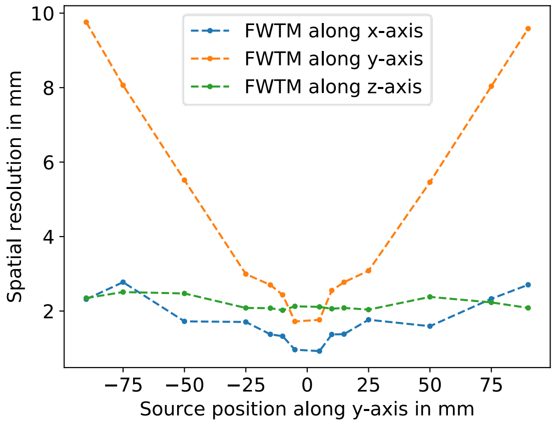

(d) 25% off axial center; FWTM.

Figure 3.28.: Simulated spatial resolutions of the "peanut" geometry for a source moved along the y-axis in one of the FOVs. Dashed lines are drawn to guide the eye.

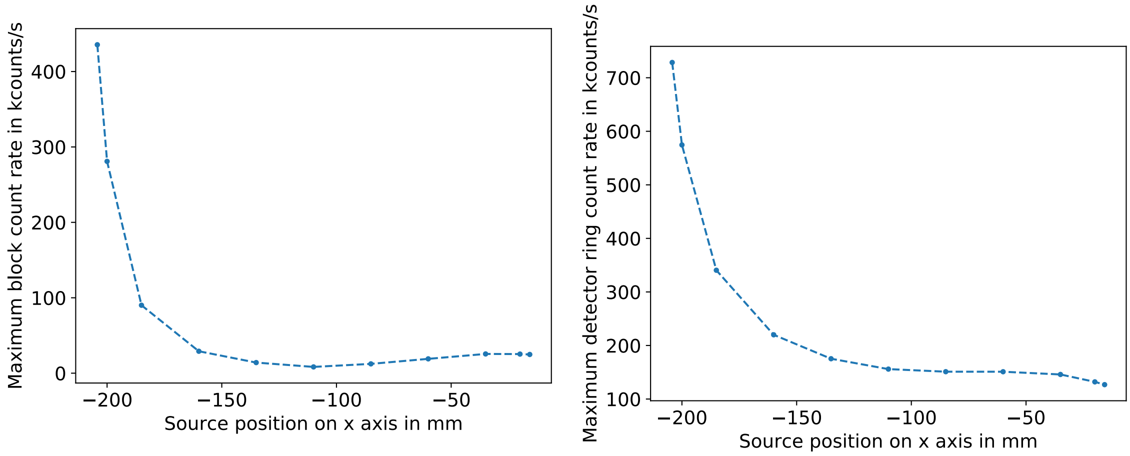

Figure 3.29.: Maximum count rates per block and detector ring of the “peanut” geometry for a source flight along the x-axis through the center of the FOV. Dashed lines are drawn to guide the eye.

better than 1.7 mm FWHM along all directions. Strong radial elongation effects with the spatial resolution along the x-axis dropping to about 5 mm FWHM and 9 mm FWTM can be seen for source positions closer towards the edges of the probed volume with this effect being slightly stronger towards the outer edges of the geometry for axially centered sources.

For source movements along the y-axis with the x-coordinate set to −110 mm the resulting spatial resolutions are shown in Figure 3.28. Overall, the simulation results for the source flights along the y-direction are similar and competitive to the spatial resolutions obtained for the “two-cylinder” geometry with better than 1.6 mm spatial resolutions along the non-radial directions for all plotted source positions. NEMA NU 4 compatible tables listing the simulated spatial resolutions are shown in the appendix A.5 and A.6.

As stated earlier, the maximum single count rate per detector block for a source placed close to the block is mostly affected by the detector block characteristics. Since the same detector block is used for all probed geometries, the expected maximum count rate per detector block is very similar towards the outer edge of the field of view. With the “peanut” geometry split in a total of four individual rings of detectors, the maximum count rate per ring amounts to 729 kcounts s^{-1} at the outer position and to 156 kcounts s^{-1} at the center of the field of view.

3.6. Conclusion

The performed simulation studies of various possible geometries of PET breast inserts underline the suitability of Monte Carlo simulations for supporting the determination of specifications of prospective PET scanners. Software helper tools and minor modifications of GATE were developed in the course of this thesis to enable GATE in combination with CASToR to simulate the detector response of arbitrary PET scanner geometries and to reconstruct the source distribution in the scanner field of view.

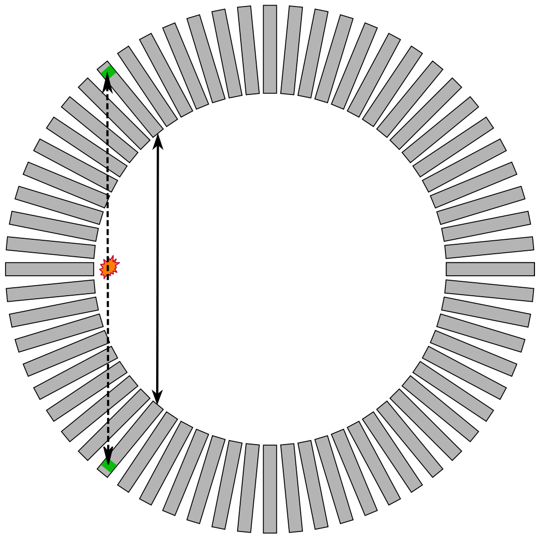

Figure 3.30.: Reduction of the parallax error using DOI. Without information about the depth of interaction, the scanner yields a line of response connecting the faces of the hit crystals (continuous line). DOI detectors, resolving the volumes of interaction to the crystal subvolumes visualized in green color, yield a more precise line of response reducing the radial elongation effect (dashed line).

The simulation results can be used to derive detector performance characteristics, such as sensitivity and spatial resolution.

All simulated PET insert geometries show significant improvements near the center of their fields of view in terms of sensitivity and spatial resolution compared to the clinical Siemens “Biograph mMR” scanner with 1.5 % sensitivity at its center, between 4.0 mm FWHM and 4.3 mm FWHM spatial resolution at a distance of 1 cm from the central position and between 6.4 mm FWHM and 6.6 mm FWHM axial spatial resolution at a distance of 10 cm from the center [DFJ+11], [KSEG16]. At the edges of the fields of view, the radial elongation effect observed in the simulations leads to a spatial resolution comparable with the resolution of the clinical scanner. A possible countermeasure to reduce this effect is the use of a depth of interaction (DOI) detector measuring the distance from the crystal face to the position of interaction between the impinging photon and the crystal. The information about the depth of interaction can be used to obtain a more accurate line of response reducing the parallax error as illustrated in Figure 3.30. A prototype of a cross-strip DOI PET detector is already available at the WSIC in Tübingen [SKP18], [KPM+14].

Solely comparing the simulated performance characteristics of the various probed PET insert geometries, the “two cylinders” geometry is the most promising setup in terms of sensitivity and spatial resolution. Although yielding similar resolutions, the “peanut” geometry shows more fluctuations in the spatial resolution depending on the source position, which could impede the interpretation of reconstructed images in a clinical use case. The “stretched cylinder” geometry shows significantly lower sensitivities for large parts of the field of view combined with declined spatial resolution with more definitive fluctuations and is therefore less favorable than the two other possible setups. Considering the assembly of the PET insert inside the patient bed, the “peanut” and “stretched cylinder” solutions are more practical, since the “two cylinders” approach requires adaptations of the patient bed and the position of the built-in breast coils, which could make significant changes to the calibration and post-processing of the MRI necessary. In result, the “two cylinders” and “peanut” solutions provide promising geometries for a breast PET insert and further simulations are necessary to compare the two devices in more realistic scenarios.

Further simulation studies can be performed to quantify the expected improvement of a DOI detector for the radial component of the spatial resolution as well as the possible benefit of operating the breast PET insert in coincidence with the outer detector rings of the clinical scanner. When operating both devices in coincidence, the bottom side of the insert could be filled with detector blocks to increase the amount of valid lines of response between the insert and the outer scanner through the patient thorax and thus to estimate the possible gain of a bottom lid for thorax lesion detection. A complete validation of the simulation and reconstruction methods can be achieved using a clinical PET scanner or a possible future prototype of the breast PET/MR insert.

More realistic scenarios can be simulated by including diversely distributed sources based on real patient data and considering attenuation inside the field of view. Realistic phantom models are available for detailed simulations of the human body [SSM+10], which could be used for simulating the impact of activities in organs on the imaging quality, especially the activity in the heart due to its spatial proximity to the breast insert, and investigate possible shielding solutions for the scanner device.

4. Simulation Studies of the XMM-Newton EPIC pn-CCD Camera Background

4.1. X-ray astronomy

X-ray astronomy studying photons with energies between 0.1 keV and 100 keV faces the challenge that ground based detectors are not feasible for observation of celestial X-ray sources due to the high level of X-ray absorption in the atmosphere. Consequently, a rocket was used for the first detection of X-rays emitted by the solar corona using a set of photon counter tubes sensitive at the soft X-ray and extreme ultraviolet spectral regions [FLB51]. In 1962, first evidence for X-rays emitted from a source outside the solar system was found using large area Geiger counters carried by an Aerobee rocket [GGPR62].

With the new X-ray window opened for astronomical observations, numerous balloons and rockets carrying X-ray detectors as well as satellites offering long, uninterrupted observation times were launched in the previous decades. With these experiments observing the universe in the X-ray spectral range, a broad range of different types of X-ray sources is known today, spanning from galactic sources such as supernova remnants or X-ray binaries to extragalactic sources such as galaxy clusters or active galactic nuclei.

A major challenge for X-ray satellite missions is the typical radiation environment present in the orbit around Earth and therefore the presence of a strong background hindering the detection of the usually rather low fluxes of cosmic X-ray sources. Although modern instruments show higher signal-to-noise ratios due to techniques reducing background and short dead times, minimization of the measured background fluxes for future missions, allowing for more significant science output and shorter observation times, is still a major topic in X-ray astronomy today [Ten08], [PBD+17].

Monte Carlo simulation studies as described in the following sections can be used to reproduce and understand the background of current X-ray instruments. Separate simulations of the expected background can be performed for the different components of the radiation environment, such as cosmic ray protons or the cosmic X-ray background composed by many X-ray sources, which are not resolved separately, in order to obtain information about the composition of the detected background. Based on these results, future detectors and shielding mechanisms can be developed and their effects on background reduction can be estimated by simulations.

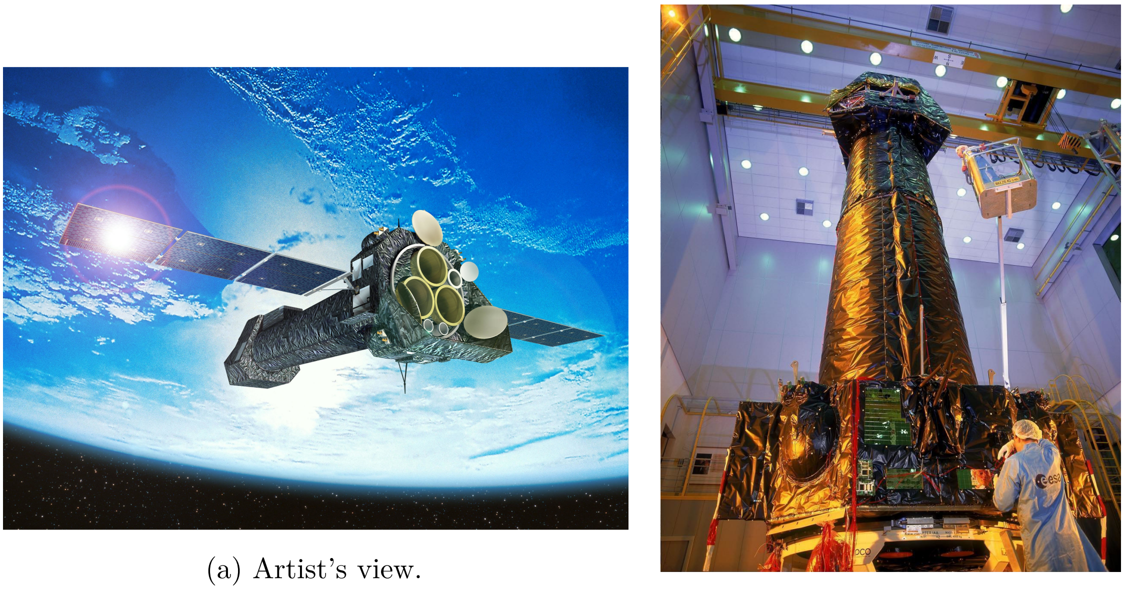

(a) Artist's view.

(b) Assembly.

Figure 4.1.: XMM-Newton satellite. Artist's impression (a), image courtesy of ESA, and photography of the XMM-Newton assembly (b), image courtesy of D. Parker and ESA.

4.2. XMM-Newton

The XMM-Newton satellite of the European Space Agency (ESA) was launched on December 10, 1999 by the first commercial Ariane-V launch. At that time, it was the largest scientific satellite launched by ESA with a spacecraft length of 10 m and a weight of 4 t. The spacecraft is placed in a highly eccentric orbit with maximum and minimum distances from Earth of 114 000 km and 7000 km, respectively, and an orbital period of about 48 h. The satellite hosts three X-ray telescopes, each consisting of 58 Wolter I mirrors arranged in a concentrical and confocal way providing a large collection area. To shield the detectors at the focal plane from low energy electrons reflected by the mirrors, an electron deflector producing a circumferential magnetic field is installed in the exit aperture. As a major step beyond previous X-ray missions, XMM-Newton was particularly designed for high quality X-ray spectroscopy on faint sources. An artist's view of the spacecraft in orbit and a picture of the XMM-Newton assembly on ground are shown in Figure 4.1 [J+01].

The European Photon Imaging Camera (EPIC) pn-CCD camera investigated in the following simulation studies is located on the Focal Plane Assembly together with two EPIC MOS detectors and two Reflection Grating Spectrometers. The layout of the CCD focal plane as shown in Figure 4.2 divides the camera into four quadrants with three individual CCDs each. Each CCD with a size of $3\,\mathrm{cm}^2 \times 1\,\mathrm{cm}^2$ and a sensitive silicon thickness of 300 µm and an additional 30 nm thick layer of silicon dioxide is divided into 199×64 pixels, resulting in a pixel size of $150\,\mu\mathrm{m} \times 150\,\mu\mathrm{m}$ corresponding to $4.1''$. To obtain a uniform quality in all detectors, the 12 individual CCDs are fabricated using a single monolithic waver [S+01].

After being focused by the XMM-Newton mirrors, X-rays impinge the fully depleted EPIC pn-CCD from the rear side causing the generation of electrons and holes in

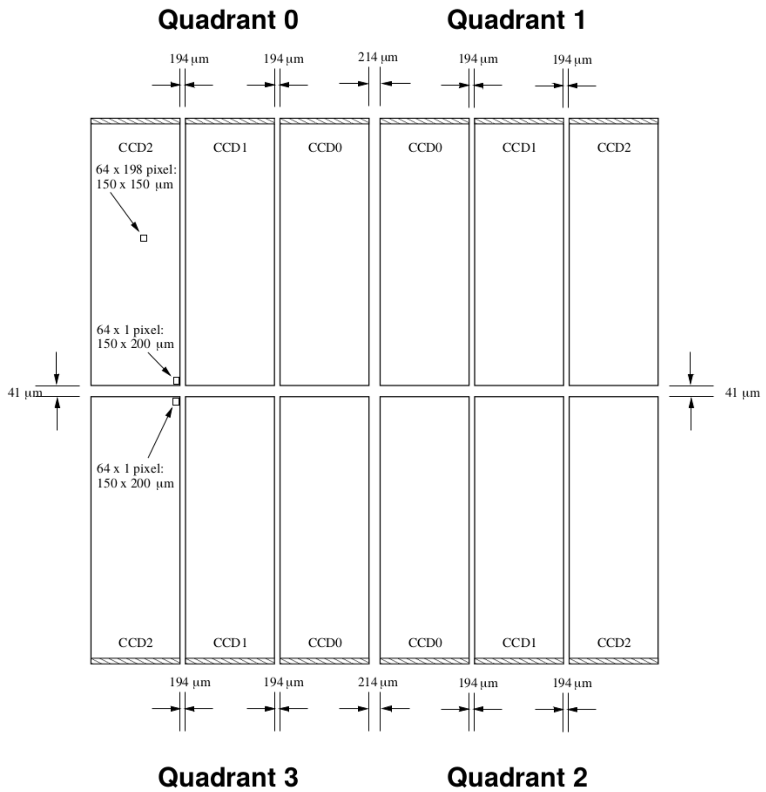

Figure 4.2.: Detector layout of the pn-CCD focal plane. The focal point is shifted to CCD0 in quadrant 1 in order to put the focal point to a sensitive area of the detector instead of the gap at the geometrical center. Each CCD is divided into 64 by 199 individual pixels resulting in a total of 152 832 pixels for the whole detector. About 6 cm^2 of the sensitive area are outside of the telescope field of view. This area can be used for background studies. Image: [S+01]

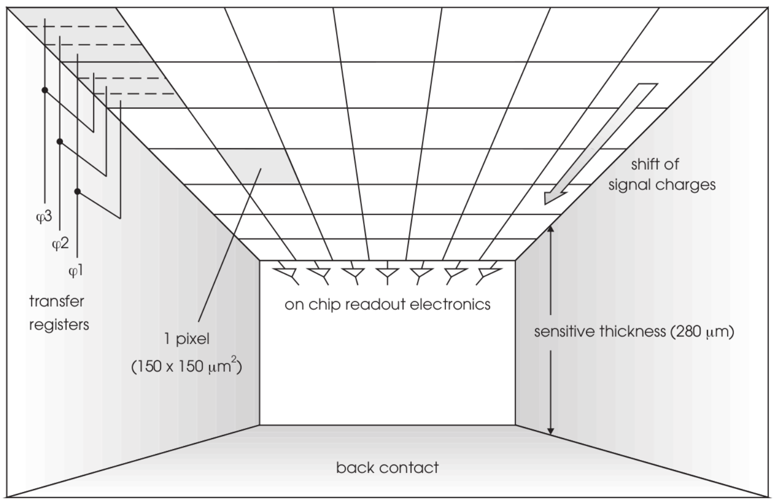

Figure 4.3.: EPIC pn-CCD readout schematics. X-rays hit the detector from the bottom producing electrons and holes. Electrons are stored 10 µm from the upper surface under the transfer registers for integration and finally shifted towards the readout amplifiers. Image: [S+01]

case of an interaction between the photon and silicon atoms. The electrons and holes are separated by electric fields shifting the holes to the back side of the detector and the electrons to the front side. As illustrated in Figure 4.3, the electrons are stored under transfer registers and finally shifted towards the readout amplifiers by applying a shifting pattern to the transfer register potentials. The local charge distribution is conserved to a high degree in the shifting process. Since all 64 channels per CCD can be measured in parallel, a high time resolution can be accomplished [S+01].

Since CCDs have been originally designed for photon intensity imaging instead of performing spectroscopy, the integration time must be short enough to detect only single events per pixel and integration time. For bright sources, the readout area of the detector must be shortened to enable faster readout cycles at the cost of a decreased sensitive detector area. Six operating modes are implemented in the EPIC pn-CCD camera differing in the duration of readout cycles and the readout area. The duration of a complete readout cycle varies between 73.3 ms and 199.2 ms for the full frame mode and extended full frame mode, respectively, and can be shortened to 7 ms choosing the burst mode [S+01].

4.3. Simulation Principles for Background Studies

4.3.1. Isotropic Background Radiation

As stated previously, satellite missions are exposed to isotropic high energy background radiation including photons and charged particles, such as protons and atomic nuclei. Realistic isotropic background radiation can be implemented in a Geant4 application by simulating primary particles created at random positions on the surface of a sphere enclosing the entire investigated detector geometry. The energies of the generated particles must thereby follow the spectrum measured by previous satellite missions, depending on the type of particles created.

In order to create isotropic radiation inside a volume from a generic surface it must be considered, that emitting particles with an isotropic angle distribution from the surface leads to non-isotropic fluxes in the volume due to Lambert's cosine law. A surface obeying Lambert's cosine law emits radiation with a radiative intensity I proportional to the cosine of the angle between the surface normal and the direction of emission θ, following

$$I = I_0 \cdot \cos\theta \tag{4.1}$$

with the radiative intensity emitted along the surface normal I_0. Since the apparent size of the emitting surface seen by an observer decreases with the cosine of θ, a constant flux independent of θ is observed. Therefore, to simulate an isotropic flux seen by the detector, a cosine-law angular distribution must be chosen for each point on the emitting surface [San07].

The Geant4 General Particle Source (GPS) (see Chapter 2.2.4) can be configured to simulate isotropic background radiation using macro commands. For the performed simulations, particles were created on the surface of a sphere with a radius of 5 m following a cosine-law. To reduce computing time, the maximum emission angle of created particles was set to $\theta_{\max} = 5°$ as shown in the following listing.

```
/gps/pos/type          Surface
/gps/pos/shape         Sphere
/gps/pos/centre        0. 0. 0. cm
/gps/pos/radius        5. m
/gps/ang/type          cos
/gps/ang/mintheta      0. deg
/gps/ang/maxtheta      5. deg
```

The intensity spectrum of the cosmic X-ray background can be approximated with an empirical analytical representation using exponential and power law functions given in [GMPJ99]:

$$
\begin{aligned}
3 - 60\text{keV}: &\quad 7.877 \cdot E^{-0.29} \cdot e^{-E/41.13} && \frac{\text{keV}}{\text{keV}\,\text{cm}^2\,\text{s}\,\text{sr}} \quad , \\
> 60\text{keV}: &\quad 0.0259 \left(\frac{E}{60}\right)^{-5.5} && \\
&\quad + 0.504 \left(\frac{E}{60}\right)^{-1.58} && \\
&\quad + 0.0288 \left(\frac{E}{60}\right)^{-1.05} && \frac{\text{keV}}{\text{keV}\,\text{cm}^2\,\text{s}\,\text{sr}} \quad .
\end{aligned}
\tag{4.2}
$$

To obtain this fit over the energy range of 3 keV to 100 GeV, measured data from three satellite missions was used. Results below 500 keV were measured by the High Energy Astronomical Ovservatory 1 (HEAO 1). At higher energies above 0.8 MeV, results from COMPTEL and EGRET on the Compton Gamma Ray Observatory (CGRO) were used. The resulting spectrum is shown in Figure 4.4a extrapolated to the minimum energy of 1 keV. For the simulations, photons were created between 1 keV and 1 GeV resulting in a total flux of 197.23 counts $\text{cm}^{-2}\,\text{s}^{-1}$ determined by numerical integration over the energy range and solid angle.

For simulating the cosmic-ray proton background, a proton spectrum averaged over the XMM-Newton orbit at the minimum of the solar cycle was calculated using the CREME86 model of the OMERE software (see [Ten08]). The resulting spectrum in the energy range of 10 MeV to 100 GeV is shown in Figure 4.4b. Numerical integration results in a total flux of 2.31 counts $\text{cm}^{-2}\,\text{s}^{-1}$ in the investigated energy range. Proton spectra for different solar cycle activities as well as additional primary particle types such as electrons or atomic nuclei were not part of the simulations performed in the course of this thesis and might be considered in future studies based on this work.

4.3.2. Normalization

Since normalization is a key principle to derive meaningful results from Monte Carlo background simulation studies, an introduction to normalization in general and more specifically how to calculate the simulated duration in case of sources in form of a spherical surface for isotropic background radiation is given in this section based on [San07].

Whenever absolute values are retrieved from Monte Carlo simulations, these results must be normalized in order to obtain the corresponding quantities in the real world.

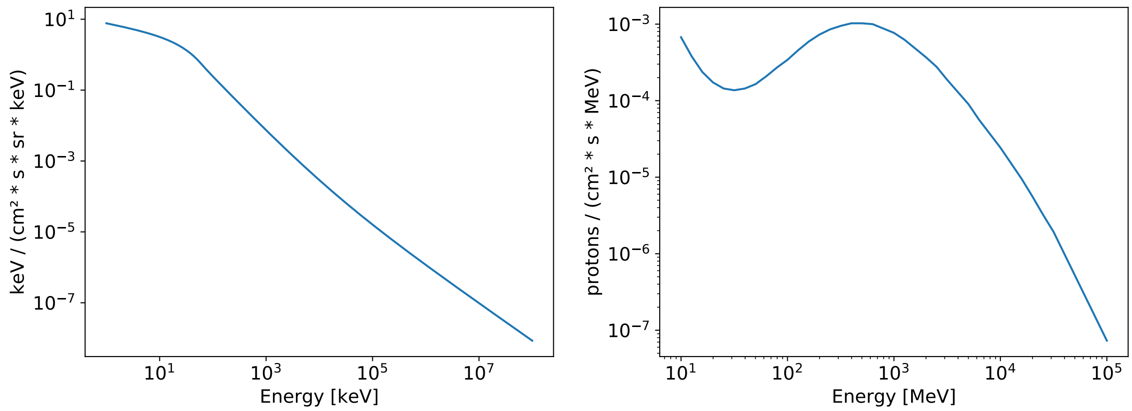

(a) Photon spectrum. (b) Proton spectrum.

Figure 4.4.: Cosmic X-ray background photon spectrum (a) as given by Equation 4.2 [GMPJ99] between 1 keV and 1×10^8 keV. The cosmic-ray proton spectrum (b) between 10 MeV and 1×10^5 MeV is calculated using the CREME86 model of the OMERE software for the minimum activity of the solar cycle averaged over the XMM-Newton orbit.

The simulation results are rescaled using

$$X_r = X_s \frac{N_r}{N_s} \tag{4.3}$$

with the quantitative results X_s and X_r in the simulation and real world, respectively, the number of simulated events N_s and the number of events expected in the real world N_r depending on the investigated source.

While N_r is known for many simulated experiments using simple source models therefore allowing for straightforward rescaling, it must be calculated from the external flux depending on the configuration of the spherical source in use for background simulations of detectors in space. Considering Lambert's cosine law as given in Equation 4.1, integration over the emission angle for a single point on the spherical surface emitting inside the volume of the sphere leads to

$$\int_0^{2\pi} d\phi \int_{\theta_{\min}}^{\theta_{\max}} d\theta \cos\theta \sin\theta = \pi \cdot \left(\sin^2\theta_{\max} - \sin^2\theta_{\min}\right) \tag{4.4}$$

with $\theta_{\max}$ and $\theta_{\min}$ defined for source biasing in order to save computing time as introduced in Chapter 4.3.1. In case the source is configured to shoot particles along all emission angles into the spherical volume, which is the default setting in the GPS, it holds $\theta_{\min} = 0$ and $\theta_{\max} = \pi/2$ resulting in a factor of π.

Consequently, integration over the surface of the sphere yields for an isotropic flux

$$\begin{aligned} n_r = \frac{N_r}{t_r} &= \int_0^{2\pi} d\phi \int_0^{\pi} d\theta R^2 \sin\theta \cdot \Phi \cdot \pi \cdot \left(\sin^2\theta_{\max} - \sin^2\theta_{\min}\right) \\ &= \Phi \cdot 4\pi^2 R^2 \cdot \left(\sin^2\theta_{\max} - \sin^2\theta_{\min}\right) \end{aligned} \tag{4.5}$$

with the considered time in the real experiment t_r, the sphere radius R and an isotropic flux Φ. Without source biasing the result simplifies to

$$n_r = \Phi \cdot 4\pi^2 R^2 \quad . \tag{4.6}$$

The simulated time duration can now be given using Equations 4.3 and 4.5 as

$$\begin{aligned} t_s &= N_s \cdot \frac{t_r}{N_r} \\ &= \frac{N_s}{\Phi \cdot 4\pi^2 R^2 \cdot (\sin^2\theta_{\max} - \sin^2\theta_{\min})} \quad , \end{aligned} \tag{4.7}$$

which reduces without source biasing to

$$t_s = \frac{N_s}{\Phi \cdot 4\pi^2 R^2} \quad . \tag{4.8}$$

For normalizing the detected flux resulting from the Monte Carlo simulation, the gathering power Γ of the telescope must be taken into account. In case of isotropic radiation this factor is referred to as the geometrical factor G meeting the proportionality relationship

$$C = G \cdot I \tag{4.9}$$

with the counting rate C and the isotropic intensity I. While calculating the geometrical factor can be cumbersome for arbitrary geometries, a simple analytical expression,

$$G = \pi \cdot A \tag{4.10}$$

with the detector area A with particles impinging from one side, can be derived for an ideal telescope with a single planar detector. In case of isotropic radiation, the detector area A of a planar detector and therefore the geometrical factor is doubled, since particles hit the detector from both sides [Sul71].

The normalized flux can therefore be calculated with the number of detected events in the simulation D_s using

$$\begin{aligned} \Phi_{res} &= \frac{D_s}{t_s \cdot G} \\ &= \frac{D_s \cdot \Phi \cdot 4\pi R^2 \, (\sin^2\theta_{\max} - \sin^2\theta_{\min})}{N_s \cdot A} \end{aligned} \tag{4.11}$$

and consequently without source biasing using

$$\Phi_{res} = \frac{D_s \cdot \Phi \cdot 4\pi R^2}{N_s \cdot A} \quad . \tag{4.12}$$

A simple test verifying the correct implementation of normalization and calculation of the resulting flux can be performed by using a spherical ideal detector in a vacuum environment artificially counting each particle inside its volume with a perfect and energy independent efficiency. In case the detector is completely contained inside the configured emission angle, the resulting flux should match the flux of created particles within statistical uncertainties. Further, the creation of isotropic radiation can be tested in a similar simulation by changing the detector shape to a rectangular plane. As long as the detector completely remains inside the configured emission angle, modifying the plane position and orientation should not affect the resulting count rate.

4.4. Simulation Studies

As stated in Section 4.1, understanding the detector background is crucial for X-ray satellite missions. Simulation studies determining the detector background induced by cosmic background sources such as the high energetic photons of the cosmic X-ray background or cosmic-ray protons are helpful in deepening the understanding of the measured detector background and the effects of the used shielding mechanisms.

Background simulation studies of the XMM-Newton EPIC pn-CCD camera were already attempted by several groups in the last years [Ten08]. The simulations face the combination of the low probability of background particles leading to a detected event, the isotropic nature of the background fluxes and the large energy range of particles, which could possibly result in detected signals. Therefore, these types of simulations need a very large amount of tracked particles in order to yield good statistics of the detected background spectra. However, the limiting factor of available computing power at that time necessitated the implementation of methods drastically reducing computing time or lowering the amount of tracked particles.

In the simulation environment described in [Ten08], a two-step approach is introduced to lower the effective count of tracked primary particles created on the spherical surface representing the cosmic background. In a first step, the interior of the camera vessel including the board and CCDs is filled with an ideal virtual detector producing a list of the physical properties of all impinging particles, such as energy, direction and particle type. A limited amount of primary particles is created and tracked while the data obtained by the virtual detector is recorded. This data is used in a second step to artificially create a large amount of particles directly on the surface of the virtual detector by interpolating and randomly sampling from the recorded data. Measured background spectra and detected images around single fluorescence lines could be reproduced with a high degree of accuracy, but it must be considered, that the particles created in the second step are not statistically independent from the first step results with less tracked primary particles.

In addition to the increased computing power since the last decade, many improvements were incorporated into recent versions of Geant4, including the ability of creating multithreaded applications, defining geometry separated from the application code using GDML as introduced in Section 2.2.2 and refined physics processes. Therefore, the objective of the work done in the course of this thesis was to repeat the previously performed background simulation studies using a new and independent[1] simulation environment based on modern Geant4 capabilities and design principles. Given the improved computing performance of the available workstation compared to the former studies, it should be evaluated whether the two-step method of reducing the amount of tracked particles introduced above can be dispensed with. Further, the new simulation environment could provide a modern basis for future background simulation studies.

[1] Independent in the sense, that implementation details and the source code of the former simulation environment are not known to the author.

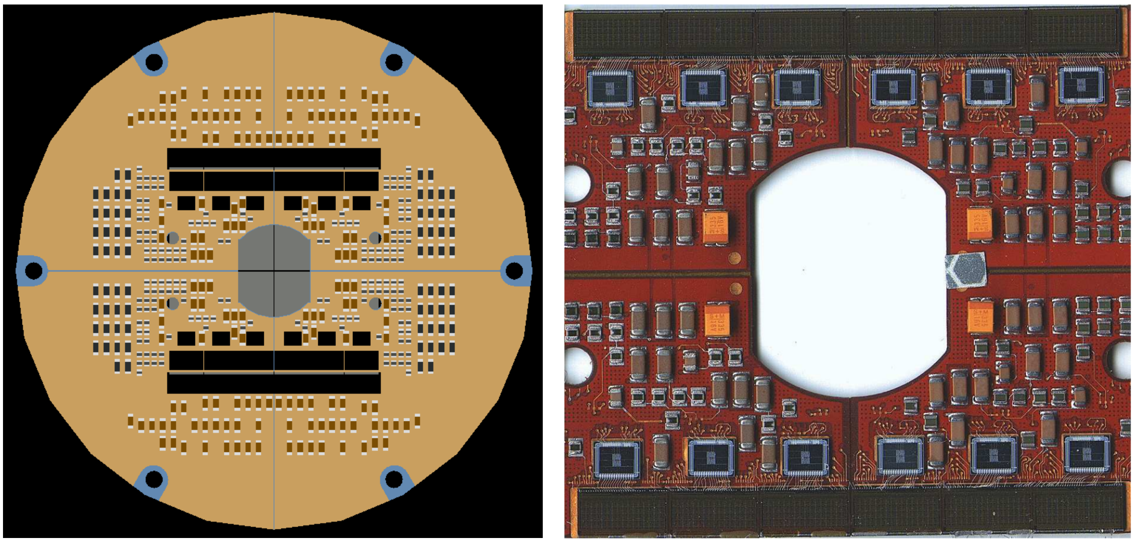

(a) GDML model. (b) Closeup photography.

Figure 4.5.: Visualization of the GDML model of the EPIC pn-CCD camera board (a) and a closeup photography of the area of a spare PCB, where the CCDs are placed on the backside (b). Many of the mounted components are reproduced in the model with a reduced level of details. Photography: [Ten08].

4.4.1. Simulation Environment

A central concern of the developed simulation environment is to provide an early revision of a modern and generic basis for future X-ray detector background simulation studies. Similar to the central approach of GATE, future revisions could therefore offer a generic application, allowing to configure and perform simulations without the necessity to know the Geant4 internals in detail or modifying the application core. Separating configuration, which is given by the user, from the application source code as far as possible is therefore of particular importance.

Traditional Geant4 applications showed a tight coupling between geometry definition and the simulation source code with the geometry developed in the C++ programming language as part of the application. Changing parts of the geometry, including only minor changes to details, required recompilation of the application. With the introduction of GDML support to Geant4, geometry definitions can be treated separately from the application. Consequently, the already existing detector geometry was ported to GDML and separated into multiple parts allowing independent reuse in simulations. The modeled EPIC pn-CCD PCB is illustrated in Figure 4.5 together with a closeup photography of the central board region without the CCDs mounted on the backside.

The simulation environment uses the sensitive detector based approach for tracking particles through the experimental setup, which allows to mark volumes in the detector geometry as sensitive. Volumes can be configured as sensitive using auxiliary fields in the GDML file and are registered in Geant4 during initialization of the simulation environment. For each interaction of a tracked particle with sensitive volumes, including the entering of the particle into the volume, a function implemented in the Geant4 application is called, saving the deposited energy and the exact position

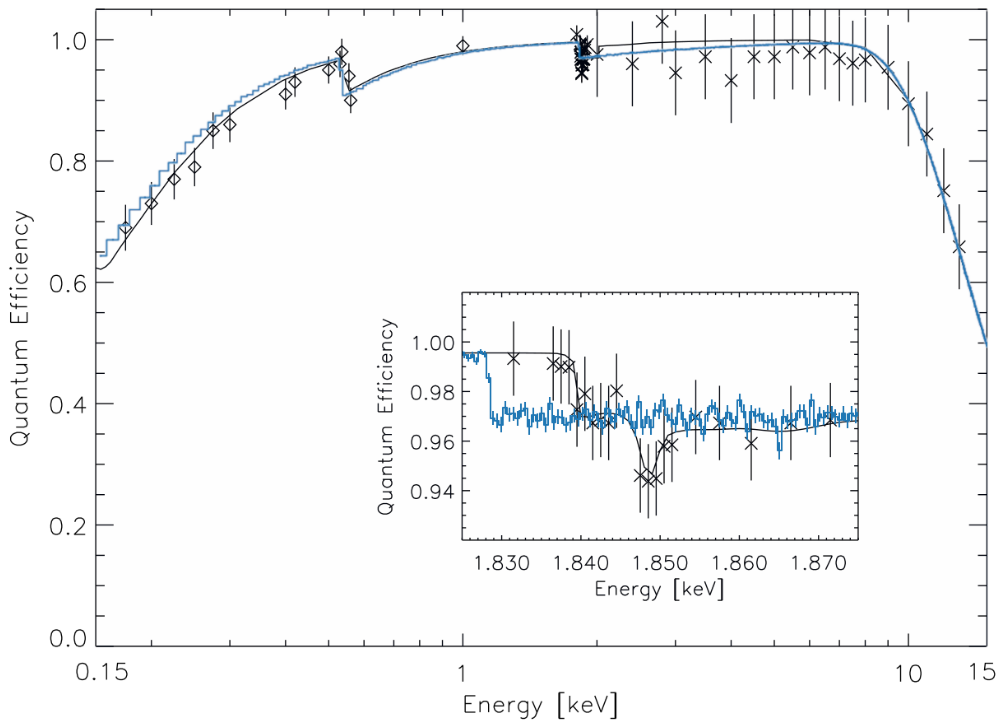

Figure 4.6.: Quantum efficiency of the pn-CCD. Simulated (blue overlay), calibration data measured at PTB (BESSY synchrotron in Berlin) and LURE (synchrotron in Orsay, Paris) and fit to the measured data assuming a sensitive silicon thickness of 298 µm (solid line). Original image: [S+01]

of this interaction. At the end of each detected event, representing the tracking of a single primary particle and all of the secondary particles produced, the initial energy of the primary particle, the deposited energy, the CCD identifier as well as the pixel number is written to a ROOT file.

Finite energy resolution can be applied to the detected particle energy at the end of each event. Two resolutions at specific energies can be defined to simulate a linear energy dependency of the energy resolution. Further effects introduced by readout electronics or readout processes are not included in the simulation environment and could be added in future revisions to allow for more realistic simulation of readout scenarios.

4.4.2. Detector Quantum Efficiency

The quantum efficiency of the pn-CCD detector was determined by simulating X-rays with a flat energy distribution between 0.15 keV and 15 keV shot from a point source towards the backside of the detector, with the beam perpendicular to the detector surface pointing towards the center of a single pixel located near the middle of one of the CCDs. A total of 1×10^8 primary particles were tracked one after another and marked as detected if the complete energy of the X-ray was deposited in the sensitive volume of the detector. The 300 µm thick sensitive silicon volume of the CCD is covered with a 30 nm thick layer made of silicon dioxide at the side facing the point source.

The simulated quantum efficiency calculated as the ratio of the numbers of detected events and tracked X-rays is shown in blue in Figure 4.6 together with measurement values obtained under conditions similar to space operation and a fit to the measured data for a silicon layer thickness of 298 µm [S+01]. The simulated data is divided in 2000 bins with a constant bin size of 7.425 eV. The simulation results agree with the measurement to a good degree of accuracy. At the low energy end, the simulated detector quantum efficiency overestimates the measurements. At energies between about 2 keV and 6 keV the simulation slightly underestimates the fit to the measured data, while still being consistent with the measurement uncertainties. The X-ray Absorption Fine Structure (XAFS) behavior at energies around the silicon K edge at 1.838 keV shown in the inlay is only partially reproduced by the simulation. While the simulation reproduces the order of the quantum efficiency drop, but shifted about 10 eV towards lower energies, the second dip is not reproduced. Further studies are required to investigate the reasons for the differences between the simulation results and the measurement around the silicon K edge.

At the low energy end, the quality of the entrance window determines the quantum efficiency with the drop at the lowest energies caused by the silicon L edge. Since the absorption length of X-rays with energies of 150 eV in silicon is about 30 nm, the thin silicon dioxide layer absorbs almost one half of the impinging photons. The significant drop of about 5 % quantum efficiency at 528 eV, which is precisely reproduced by the simulation, is caused by the oxygen K edge in the silicon dioxide layer. At the high energy end, the thickness of the sensitive silicon layer determines the quantum efficiency through its X-ray absorption characteristics [S+01].

In order to reduce the remaining differences between simulation and measurement, the effects of small variations to the geometry, such as modifying the thickness of the silicon dioxide layer and slightly varying material compositions and densities, can be investigated in further simulations.

4.4.3. Background Spectrum

For simulating the EPIC pn-CCD camera background spectrum, protons and photons were created on a spherical surface with a radius of 5 m mimicking an isotropic cosmic background and a maximum emission angle of $\theta_{\mathrm{max}} = 5°$ to avoid tracking of particles not directed towards the satellite geometry. The energy of the created primary particles was sampled from the proton and photon spectra introduced in Section 4.3.1. A total of 3×10^9 primary protons were tracked, corresponding to a simulated duration of 17 323 s or slightly less than 5 h according to Equation 4.7 and the total proton flux of 2.31 counts $\mathrm{cm}^{-2}\,\mathrm{s}^{-1}$ in the probed energy range between 10 MeV and 100 GeV. With a cosmic X-ray background flux of 197.23 counts $\mathrm{cm}^{-2}\,\mathrm{s}^{-1}$, about 2.56×10^{11} primary photons were created and tracked through the simulation setup corresponding to the same simulated duration.

The energy resolution of the EPIC pn-CCD in full frame mode determined using the calibration source on board of XMM-Newton is 152 eV FWHM at the Mn-K_α edge and 111 eV FWHM at the Al-K_α energy [S+01]. Based on a linear fit along the full detector energy range using these values, the energy resolution is simulated in the post processing stage of the simulation environment by randomly sampling from a

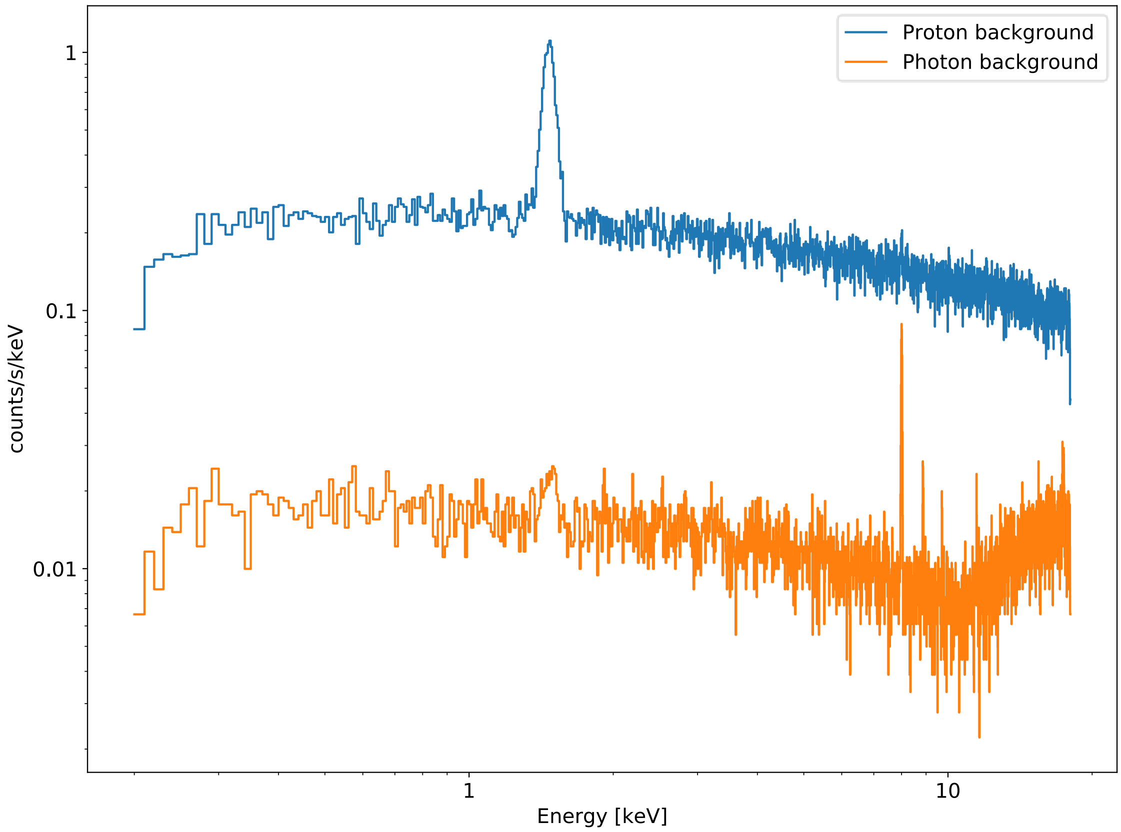

Figure 4.7.: Simulated EPIC pn-CCD background spectra induced by cosmic ray protons (blue) and the cosmic X-ray background (orange) between 0.2 keV and 18 keV for a simulated duration of 17 323 s and a constant bin size of 10 eV.

Gaussian function with the fitted FWHM at the precise detected energy resulting from the particle tracking.

Further properties of the CCDs such as the noise introduced by the readout electronics or the losses due to charge transfer were not implemented in the simulation. In addition, the electron clouds in the CCDs were not simulated to save computing time. Therefore, all detected particles are considered single events as long as the particle impinging the detector deposits all of its energy inside a single pixel. This process could be improved in further simulation studies by estimating the size of the electron cloud from the incoming particle without tracking the individual electrons of the cloud.

The simulated detector background spectrum separated into parts induced by proton or photon background is shown in Figure 4.7 with the resulting flux calculated using Equation 4.11 and subsequently dividing by the investigated energy range. At energies below 10 keV, the background induced by the cosmic ray protons is dominating. The number of proton induced events at lower energies is about one order of magnitude higher compared to the events due to the cosmic X-ray background. Above 10 keV, photon induced counts gain relevance, while still being responsible for significantly lower count rates than events induced by cosmic-ray protons. Strong aluminum and copper features can be seen in the proton induced and photon induced spectra, respectively.

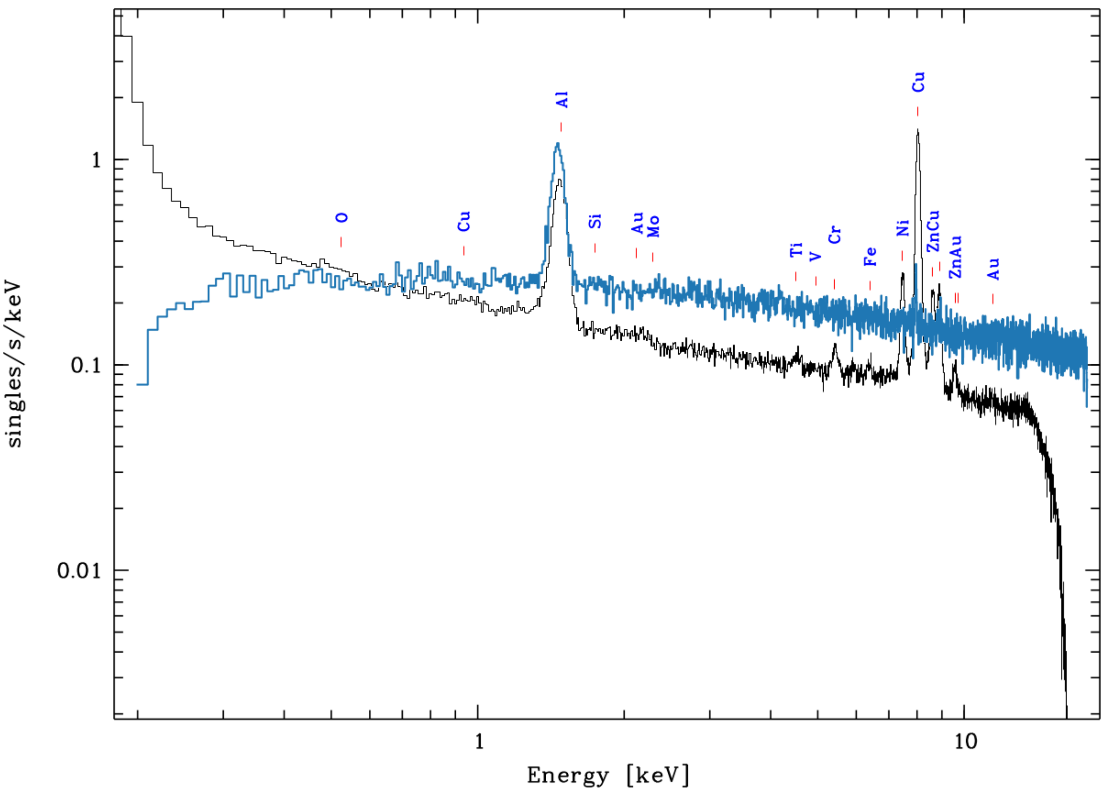

Figure 4.8.: EPIC pn-CCD background spectrum simulated (blue histogram) and measured (black histogram) between 0.2 keV and 18 keV. The measured data contains single pixel events taken in full frame and extended full frame modes for a measured time frame of 313 ks. The simulated duration is about 17 ks. Image: [FBD+04]

The composite simulated detector background spectrum including all detected events is depicted in Figure 4.8 as blue overlay together with a measured spectrum containing only single pixel events. The simulation results reproduce the trend of the measured data apart from the low and high energy limits. The measured flux is overestimated by the simulation results, which is probably mostly due to the electron clouds produced in the CCDs not considered in the simulation. Therefore, events producing an electron cloud spanning two pixels are considered single pixel events in the simulation.

Towards the low and high energy limits, the simulation results are strongly different from the measurement. This can be explained by the readout electronics and readout process not being included in the simulation. For single pixel events, a high energy threshold is applied onboard the satellite, suppressing events above 15 keV and producing the high energy cut off in the spectrum. At energies below 0.4 keV the peak is caused by noise of the readout electronics producing significantly different noise peaks for single and double pixel events [FBD+04].

The aluminum feature due to the camera vessel and the proton shield is nicely reproduced in the simulation results together with a matching energy resolution manifesting in the width of the peaks. While the copper fluorescence line is clearly visible but underestimated, smaller features are not visible in the simulated data due to the simplified geometry of the detector board containing only the materials producing the most prominent features in the spectrum.

4.5. Conclusion

For the performed simulations of the XMM-Newton EPIC pn-CCD quantum efficiency and the simulated background spectra, a Geant4 application inspired by the work of [Ten08] more than ten years ago was developed from scratch using improvements and implementing modernized design principles introduced to the Geant4 toolkit during the last years. Special attention was paid to prepare for strong separation of simulation configuration and implementation, allowing to quickly vary multiple degrees of freedom such as the simulated geometry, including definitions of the sensitive volumes, source definitions or further configuration options without the need of modifying the code or recompiling. Therefore, beyond the specific simulations described in this thesis, the developed simulation environment can be seen as a basis enabling further and more sophisticated background simulations for existing or planned high energy satellite missions.

Using the introduced simulation environment, the EPIC pn-CCD quantum efficiency on board the XMM-Newton mission as well as the estimated spectra for background radiation consisting of cosmic-ray protons and high energy photons were simulated and compared to measurements. The detector quantum efficiency estimated by simulating a flat spectrum of photons all hitting the same detector pixel agrees with measured data to a good degree of accuracy. The possible effects from adding more details to the idealistic detector geometry can be investigated in future simulation studies together with the implementation of electric fields in the detector, which were outside the scope of the performed simulation.

The simulated background spectra of the EPIC pn-CCD camera on board the XMM-Newton satellite mission show, that the detector background count rate induced by protons is about one order of magnitude higher than the count rate induced by cosmic X-ray background photons for large parts of the energy range. Apart from the regimes at the low and high energy thresholds of the detector, where effects in the detector electronics become significant, the simulated composite background spectrum reproduces the trend of the measurements and the aluminum feature. More realistic simulations can be performed in future studies by developing a simplified model of estimating the measures of the electron cloud produced in the detector from the properties of the impinging particle helping to distinguish between single and double pixel events more precisely. Further, adding more details to the detector geometry and materials might allow to reproduce less pronounced fluorescence lines seen in the measured spectrum.

Due to the large amounts of tracked primary particles needed for background simulation studies of X-ray detectors in a space environment, the available computing power is key especially for simulating long exposure times. While the background spectra simulated in the course of this thesis were calculated on a single workstation, high performance clusters are necessary to calculate extended simulations in a reasonable amount of time, enabling i.e. background images around single fluorescence lines visualizing the spatial distributions of fluorescence emissions.

Beyond simulations of the XMM-Newton geometry, the developed simulation environment can be used to investigate the expected effects of various background reducing techniques, such as different single material shieldings, a graded-z shielding or the use of a magnetic diverter.

5. Conclusions

In the course of this thesis, Monte Carlo simulation studies were applied to problems in the physics fields of medical imaging with the objective to quantify the expected performance characteristics of a planned detector system, and high energy astrophysics with the focus on understanding previous background measurements by reproducing the measured data using simulations. Both performed simulation studies represent promising first steps in the respective projects with simulation environments developed to enable further and more sophisticated studies.

Three different geometries for a planned breast PET/MR insert were investigated using GATE for Monte Carlo simulations, CASToR for reconstruction and custom helper tools allowing for convenient creation and simulation of generic geometries of PET detectors, which are not based on a cylindrical shape. Simulation results for sensitivity and spatial resolution were determined based on the procedures suggested in the NEMA NU 4 standard for small animal positron emission tomographs. The “two cylinders” and “peanut” geometries in particular showed promising PET performance characteristics. Especially, significant improvements of the spatial resolution near the center of the FOV were found for both geometries with simulated results better than 1.6 mm FWHM compared to spatial resolutions at the center of the FOV in modern clinical scanners of roughly 4 mm FWHM. Towards the edges of the FOV, radial elongation effects were discovered in all simulated inserts.

Further simulation studies are necessary to identify the benefits of a DOI detector on the radial elongation effect and estimate possible improvements to thorax lesion detection by operating the breast insert, optionally with a closing bottom lid, in coincidence with the outer PET scanner. By including realistic patient models, organ uptake and its impact on the imaging quality can be simulated together with possible shielding countermeasures.

The Geant4 simulation environment, which was implemented in the course of this thesis for performing background simulation studies for X-ray satellite missions, was used to reproduce measured results of the EPIC-pn detector quantum efficiency on board the XMM-Newton mission to a good degree of accuracy. The resulting background spectra of the simulated EPIC-pn detector in closed filter wheel position reproduced the trend and a strong aluminum fluorescence line found in previous closed lid measurements. Cosmic-ray protons were identified to be responsible for a significantly larger fraction of the background spectrum compared with the photons of the cosmic X-ray background.

Refined background spectra can be obtained in further simulation studies by increasing the degree of details both in the detector geometry to work out less pronounced fluorescence lines as well as in the simulation application to better distinguish single pixel from multi pixel events by estimating the size and position of the electron clouds produced in the detector. Further background simulation studies can be performed comparing the effects of different single material shieldings, a graded-z shielding or a magnetic diverter to support the development of future shielding mechanisms for X-ray satellites. In addition, the introduced simulation environment could be extended and generalized further by continuously decoupling configuration and code to reduce the time needed to create background simulation configurations similar to GATE in medical imaging.

Bibliography

[A+03] S. Agostinelli *et al.*, "Geant4—a simulation toolkit," *Nuclear Instruments and Methods in Physics Research Section A: Accelerators, Spectrometers, Detectors and Associated Equipment*, vol. 506, no. 3, pp. 250 – 303, 2003. [Online]. Available: https://doi.org/10.1016/S0168-9002(03)01368-8

[A+06] J. Allison *et al.*, "Geant4 developments and applications," *IEEE Transactions on Nuclear Science*, vol. 53, no. 1, pp. 270–278, Feb 2006. [Online]. Available: https://doi.org/10.1109/TNS.2006.869826

[A+16] J. Allison *et al.*, "Recent developments in Geant4," *Nuclear Instruments and Methods in Physics Research Section A: Accelerators, Spectrometers, Detectors and Associated Equipment*, vol. 835, pp. 186 – 225, 2016. [Online]. Available: https://doi.org/10.1016/j.nima.2016.06.125

[BFS+18] F. Bray, J. Ferlay, I. Soerjomataram, R. L. Siegel, L. A. Torre, and A. Jemal, "Global cancer statistics 2018: GLOBOCAN estimates of incidence and mortality worldwide for 36 cancers in 185 countries," *CA: A Cancer Journal for Clinicians*, vol. 68, no. 6, pp. 394–424, 2018. [Online]. Available: https://doi.org/10.3322/caac.21492

[BTVM05] D. L. Bailey, D. W. Townsend, P. E. Valk, and M. N. Maisey, Eds., *Positron Emission Tomography.* Springer, 2005. [Online]. Available: https://doi.org/10.1007/b136169

[Bud98] T. F. Budinger, "PET instrumentation: What are the limits?" *Seminars in Nuclear Medicine*, vol. 28, no. 3, pp. 247 – 267, 1998. [Online]. Available: https://doi.org/10.1016/S0001-2998(98)80030-5

[C+17] O. A. Catalano *et al.*, "An overview of PET/MR, focused on clinical applications," *Abdominal Radiology*, vol. 42, no. 2, pp. 631–644, Feb 2017. [Online]. Available: https://doi.org/10.1007/s00261-016-0894-5

[DFJ+11] G. Delso, S. Fürst, B. Jakoby, R. Ladebeck, C. Ganter, S. G. Nekolla, M. Schwaiger, and S. I. Ziegler, "Performance Measurements of the Siemens mMR Integrated Whole-Body PET/MR Scanner," *Journal of Nuclear Medicine*, 2011. [Online]. Available: https://www.doi.org/10.2967/jnumed.111.092726

[FBD+04] M. J. Freyberg, U. G. Briel, K. Dennerl, F. Haberl, G. D. Hartner, E. Pfeffermann, E. Kendziorra, M. G. F. Kirsch, and D. H. Lumb, "EPIC pn-CCD detector aboard XMM-Newton: status of the background calibration," 2004. [Online]. Available: https://doi.org/10.1117/12.506277

[FLB51] H. Friedman, S. W. Lichtman, and E. T. Byram, "Photon Counter Measurements of Solar X-Rays and Extreme Ultraviolet Light," *Physical Review*, vol. 83, pp. 1025–1030, Sep 1951. [Online]. Available: https://doi.org/10.1103/PhysRev.83.1025

[GGPR62] R. Giacconi, H. Gursky, F. R. Paolini, and B. B. Rossi, "Evidence for x Rays From Sources Outside the Solar System," *Physical Review Letters*, vol. 9, pp. 439–443, Dec 1962. [Online]. Available: https://doi.org/10.1103/PhysRevLett.9.439

[GMPJ99] D. E. Gruber, J. L. Matteson, L. E. Peterson, and G. V. Jung, "The Spectrum of Diffuse Cosmic Hard X-Rays Measured with HEAO 1," *The Astrophysical Journal*, vol. 520, no. 1, p. 124, 1999. [Online]. Available: https://doi.org/10.1086/307450

[Har10] R. L. Harrison, "Introduction To Monte Carlo Simulation," *AIP Conf Proc*, vol. 1204, pp. 17–21, Jan 2010. [Online]. Available: https://doi.org/10.1063/1.3295638

[J+01] F. Jansen *et al.*, "XMM-Newton observatory* - I. The spacecraft and operations," *A&A*, vol. 365, no. 1, pp. L1–L6, 2001. [Online]. Available: https://doi.org/10.1051/0004-6361:20000036

[J+04] S. Jan *et al.*, "GATE: a simulation toolkit for PET and SPECT," *Physics in Medicine & Biology*, vol. 49, no. 19, p. 4543, 2004. [Online]. Available: https://doi.org/10.1088/0031-9155/49/19/007

[J+11] S. Jan *et al.*, "GATE V6: a major enhancement of the GATE simulation platform enabling modelling of CT and radiotherapy," *Physics in Medicine & Biology*, vol. 56, no. 4, p. 881, 2011. [Online]. Available: https://doi.org/10.1088/0031-9155/56/4/001

[JSS+98] F. Jacobs, E. Sundermann, B. D. Sutter, M. Christiaens, and I. Lemahieu, "A Fast Algorithm to Calculate the Exact Radiological Path through a Pixel or Voxel Space," *Journal of Computing and Information Technology*, vol. 6, no. 1, pp. 89–94, 1998.

[KBA15] S. Koren and M. Bentires-Alj, "Breast Tumor Heterogeneity: Source of Fitness, Hurdle for Therapy," *Molecular Cell*, vol. 60, no. 4, pp. 537–546, Nov 2015. [Online]. Available: https://doi.org/10.1016/j.molcel.2015.10.031

[KPM+14] A. Kolb, C. Parl, F. Mantlik, C. C. Liu, E. Lorenz, D. Renker, and B. J. Pichler, "Development of a novel depth of interaction PET detector using highly multiplexed G-APD cross-strip encoding," *Medical Physics*, vol. 41, no. 8, 2014. [Online]. Available: https://doi.org/10.1118/1.4890609

[KSEG16] A. M. Karlberg, O. Sæther, L. Eikenes, and P. E. Goa, "Quantitative comparison of PET performance—Siemens Biograph mCT and mMR," *EJNMMI Physics*, vol. 3, no. 1, p. 5, Feb 2016. [Online]. Available: https://doi.org/10.1186/s40658-016-0142-7

[LG03] A. M. Loening and S. S. Gambhir, "AMIDE: A Free Software Tool for Multimodality Medical Image Analysis," *Molecular Imaging*, vol. 2, no. 3, 2003. [Online]. Available: https://doi.org/10.1162/15353500200303133

[MD14] R. F. J. Muzic and F. P. DiFilippo, "Positron emission tomography-magnetic resonance imaging: technical review," *Semin Roentgenol*, vol. 49, no. 3, pp. 242–254, Jul 2014. [Online]. Available: https://doi.org/10.1053/j.ro.2014.10.001

[Met87] N. Metropolis, "The Beginning of the Monte Carlo Method," *Los Alamos Science*, vol. 15, pp. 125–130, 1987.

[MNP+14] L. G. Martelotto, C. K. Ng, S. Piscuoglio, B. Weigelt, and J. S. Reis-Filho, "Breast cancer intra-tumor heterogeneity," *Breast Cancer Research*, vol. 16, no. 3, p. 210, May 2014. [Online]. Available: https://doi.org/10.1186/bcr3658

[Mos11] W. W. Moses, "Fundamental limits of spatial resolution in PET," *Nuclear Instruments and Methods in Physics Research Section A: Accelerators, Spectrometers, Detectors and Associated Equipment*, vol. 648, pp. 236–240, Aug 2011. [Online]. Available: https://doi.org/10.1016/j.nima.2010.11.092

[MSB+18] T. Merlin, S. Stute, D. Benoit, J. Bert, T. Carlier, C. Comtat, M. Filipovic, F. Lamare, and D. Visvikis, "CASToR: a generic data organization and processing code framework for multi-modal and multi-dimensional tomographic reconstruction," *Physics in Medicine & Biology*, vol. 63, no. 18, p. 185005, 2018. [Online]. Available: http://stacks.iop.org/0031-9155/63/i=18/a=185005

[NEM08] NEMA, "NEMA Standards Publication NU 4-2008," National Electrical Manufacturers Association, Rosslyn, VA, USA, Standard, 2008.

[PBD+17] E. Perinati, M. Barbera, S. Diebold, A. Guzman, A. Santangelo, and C. Tenzer, "Preliminary assessment of the ATHENA/WFI non-X-ray background," *Experimental Astronomy*, vol. 44, no. 3, pp. 387–399, Dec 2017. [Online]. Available: https://doi.org/10.1007/s10686-017-9541-6

[PG18] M. Pinto and P. Gonçalves. (2018) GUIMesh: a tool to import STEP geometries into Geant4 via GDML.

[RF16] S. L. Rice and K. P. Friedman, "Clinical PET-MR Imaging in Breast Cancer and Lung Cancer," *PET Clin*, vol. 11, no. 4, pp. 387–402, Oct 2016. [Online]. Available: https://doi.org/10.1016%2Fj.cpet.2016.05.008

[S+01] L. Strüder *et al.*, "The European Photon Imaging Camera on XMM-Newton: The pn-CCD camera," *A&A*, vol. 365, no. 1, pp. L18–L26, 2001. [Online]. Available: https://doi.org/10.1051/0004-6361:20000066

[S+12] J. Schindelin *et al.*, "Fiji: an open-source platform for biological-image analysis," *Nature Methods*, vol. 9, no. 7, pp. 676–682, Jul 2012. [Online]. Available: https://doi.org/10.1038/nmeth.2019

[S+16] J. Schmitz *et al.*, "Decoding Intratumoral Heterogeneity of Breast Cancer by Multiparametric In Vivo Imaging: A Translational Study," *Cancer Research*, vol. 76, no. 18, pp. 5512–5522, 2016. [Online]. Available: https://doi.org/10.1158/0008-5472.CAN-15-0642

[San07] G. Santin, "Normalisation modelling sources," 2007. [Online]. Available: http://geant4.in2p3.fr/2007/prog/GiovanniSantin/GSantin_Geant4_Paris07_Normalisation_v07.pdf

[SK06] A. K. Shukla and U. Kumar, "Positron emission tomography: An overview," *J Med Phys*, vol. 31, no. 1, pp. 13–21, Jan 2006. [Online]. Available: https://doi.org/10.4103/0971-6203.25665

[SKP18] F. P. Schmidt, A. Kolb, and B. J. Pichler, "Optimization, evaluation and calibration of a cross-strip DOI detector," *Physics in Medicine & Biology*, vol. 63, no. 4, p. 045022, 2018. [Online]. Available: https://doi.org/10.1088/1361-6560/aaac0b

[SRE12] C. A. Schneider, W. S. Rasband, and K. W. Eliceiri, "NIH Image to ImageJ: 25 years of image analysis," *Nature Methods*, vol. 9, no. 7, pp. 671–675, Jul 2012. [Online]. Available: https://doi.org/10.1038/nmeth.2089

[SSM+10] W. P. Segars, G. Sturgeon, S. Mendonca, J. Grimes, and B. M. W. Tsui, "4D XCAT phantom for multimodality imaging research," *Medical Physics*, vol. 37, no. 9, pp. 4902–4915, 2010. [Online]. Available: https://doi.org/10.1118/1.3480985

[Sul71] J. D. Sullivan, "Geometrical factor and directional response of single and multi-element particle telescopes," *Nuclear Instruments and Methods*, vol. 95, p. 5, 1971. [Online]. Available: https://doi.org/10.1016/0029-554X(71)90033-4

[SV82] L. A. Shepp and Y. Vardi, "Maximum Likelihood Reconstruction for Emission Tomography," *IEEE Transactions on Medical Imaging*, vol. 1, no. 2, pp. 113–122, 1982.

[Ten08] J.-C. Tenzer, "Monte-Carlo Background Studies for Space-Based Detectors in X-ray Astronomy," Ph.D. dissertation, Eberhard Karls Universität Tübingen, 2008.

[Tow08] D. W. Townsend, "Positron Emission Tomography/Computed Tomography," *Seminars in Nuclear Medicine*, vol. 38, no. 3, pp. 152–166, 2008. [Online]. Available: https://doi.org/10.1053/j.semnuclmed.2008.01.003

[UX07] T. Ullrich and Z. Xu. (2007) Treatment of Errors in Efficiency Calculations. [Online]. Available: https://arxiv.org/abs/physics/0701199

[VCD+17] C. Vuosalo, D. Carlsmith, S. Dasu, K. Palladino, and L.-Z. Collaboration, "A tool to convert CAD models for importation into Geant4," *Journal of Physics: Conference Series*, vol. 898, no. 4, p. 042024, 2017. [Online]. Available: https://doi.org/10.1088/1742-6596/898/4/042024

Appendix

A. Tabular View of the Simulated Spatial Resolution Results

Table A.1.: Simulated spatial resolution values for a point source moved along the x-axis for the cylinder of the „two cylinders“ geometry placed at the negative x-axis. Position values are relative to the center of the field of view at position $(-120.75, 0, 0)$ mm.

Reconstructed image pixel size: 0.5 mm								
Slice thickness: 0.5 mm								
At axial center								
	−90 mm		−75 mm		−50 mm		−25 mm	
	FWHM	FWTM	FWHM	FWTM	FWHM	FWTM	FWHM	FWTM
x	5.22	9.51	4.25	7.74	2.87	5.22	1.52	2.77
y	1.34	2.45	1.41	2.57	1.08	1.97	1.05	1.92
z	1.14	2.08	1.18	2.15	1.21	2.20	1.40	2.54
	−15 mm		−10 mm		−5 mm		5 mm	
	FWHM	FWTM	FWHM	FWTM	FWHM	FWTM	FWHM	FWTM
x	1.27	2.31	1.20	2.18	0.99	1.81	1.00	1.82
y	1.14	2.07	1.11	2.02	1.06	1.92	1.04	1.90
z	1.45	2.63	1.42	2.60	1.33	2.43	1.32	2.41
	10 mm		15 mm		25 mm		50 mm	
	FWHM	FWTM	FWHM	FWTM	FWHM	FWTM	FWHM	FWTM
x	1.14	2.07	1.22	2.22	1.61	2.93	2.86	5.21
y	1.02	1.87	1.04	1.89	1.17	2.13	1.17	2.13
z	1.46	2.66	1.37	2.50	1.48	2.69	1.39	2.12
	75 mm		90 mm					
	FWHM	FWTM	FWHM	FWTM				
x	4.21	7.68	5.53	10.08				
y	1.14	2.08	1.53	2.79				
z	1.48	1.78	1.33	2.01				
At 1/4 axial FOV from center								
	−90 mm		−75 mm		−50 mm		−25 mm	
	FWHM	FWTM	FWHM	FWTM	FWHM	FWTM	FWHM	FWTM
x	5.05	9.21	4.37	7.97	2.88	5.24	1.48	2.69
y	1.42	2.60	1.15	2.09	1.15	2.10	1.10	2.01
z	1.07	1.95	1.23	2.25	1.26	2.30	1.28	2.31
	−15 mm		−10 mm		−5 mm		5 mm	
	FWHM	FWTM	FWHM	FWTM	FWHM	FWTM	FWHM	FWTM
x	1.23	2.24	1.12	2.04	0.97	1.77	0.99	1.80
y	1.10	2.01	1.11	2.03	1.13	2.06	1.05	1.92
z	1.14	2.07	1.37	2.28	1.42	2.35	1.36	2.25
	10 mm		15 mm		25 mm		50 mm	
	FWHM	FWTM	FWHM	FWTM	FWHM	FWTM	FWHM	FWTM
x	1.13	2.07	1.25	2.29	1.47	2.67	2.79	5.09
y	1.11	2.02	1.08	1.97	1.15	2.09	1.06	1.94
z	1.30	2.15	1.41	2.33	1.40	2.32	1.11	2.03
	75 mm		90 mm					
	FWHM	FWTM	FWHM	FWTM				
x	4.25	7.74	5.35	9.75				
y	1.17	2.13	1.47	2.67				
z	1.10	2.00	1.08	1.96				

Table A.2.: Simulated spatial resolution values for a point source moved along the y-axis for the cylinder of the „two cylinders“ geometry placed at the negative x-axis.

Reconstructed image pixel size: 0.5 mm								
Slice thickness: 0.5 mm								
At axial center								
	−90 mm		−75 mm		−50 mm		−25 mm	
	FWHM	FWTM	FWHM	FWTM	FWHM	FWTM	FWHM	FWTM
x	1.54	2.80	0.88	1.60	1.10	2.00	0.96	1.76
y	5.29	9.65	4.63	8.43	3.01	5.48	1.75	3.19
z	1.21	2.21	1.18	2.14	1.41	2.56	1.43	2.61
	−15 mm		−10 mm		−5 mm		5 mm	
	FWHM	FWTM	FWHM	FWTM	FWHM	FWTM	FWHM	FWTM
x	1.00	1.82	0.82	1.49	0.90	1.63	0.95	1.73
y	1.24	2.25	1.28	2.33	1.07	1.96	1.00	1.82
z	1.36	2.48	1.32	2.40	1.34	2.44	1.20	2.19
	10 mm		15 mm		25 mm		50 mm	
	FWHM	FWTM	FWHM	FWTM	FWHM	FWTM	FWHM	FWTM
x	0.84	1.53	0.97	1.78	0.97	1.77	1.04	1.89
y	1.35	2.46	1.32	2.41	1.70	3.10	2.95	5.38
z	1.32	2.41	1.32	2.41	1.46	2.67	1.41	2.57
	75 mm		90 mm					
	FWHM	FWTM	FWHM	FWTM				
x	0.83	1.51	1.26	2.30				
y	4.50	8.20	5.23	9.53				
z	1.16	2.11	1.26	2.30				
At 1/4 axial FOV from center								
	−90 mm		−75 mm		−50 mm		−25 mm	
	FWHM	FWTM	FWHM	FWTM	FWHM	FWTM	FWHM	FWTM
x	1.50	2.74	0.84	1.53	1.04	1.90	0.96	1.76
y	5.38	9.81	4.54	8.28	2.88	5.25	1.68	3.06
z	1.16	2.11	1.21	2.20	1.37	2.49	1.21	2.21
	−15 mm		−10 mm		−5 mm		5 mm	
	FWHM	FWTM	FWHM	FWTM	FWHM	FWTM	FWHM	FWTM
x	0.95	1.74	0.85	1.54	0.99	1.80	0.96	1.76
y	1.36	2.48	1.40	2.55	1.06	1.94	1.02	1.86
z	1.19	2.17	1.20	2.18	1.11	2.02	1.08	1.97
	10 mm		15 mm		25 mm		50 mm	
	FWHM	FWTM	FWHM	FWTM	FWHM	FWTM	FWHM	FWTM
x	0.83	1.50	0.93	1.70	0.90	1.65	1.03	1.87
y	1.34	2.44	1.26	2.31	1.68	3.06	2.97	5.41
z	1.18	2.15	1.13	2.06	1.21	2.21	1.19	2.17
	75 mm		90 mm					
	FWHM	FWTM	FWHM	FWTM				
x	0.98	1.79	1.26	2.29				
y	4.68	8.54	5.04	9.18				
z	1.24	2.25	1.40	2.56				

Table A.3.: Simulated spatial resolution values for a point source moved along the x-axis for the „stretched cylinder“ geometry. Position values are relative to the center of the field of view at position $(-110, 0, 0)$ mm.

Reconstructed image pixel size: 0.5 mm								
Slice thickness: 0.5 mm								
At axial center								
	−90 mm		−75 mm		−50 mm		−25 mm	
	FWHM	FWTM	FWHM	FWTM	FWHM	FWTM	FWHM	FWTM
x	5.29	9.65	3.97	7.23	3.04	5.55	2.09	3.81
y	1.74	3.17	1.09	1.99	1.49	2.72	2.16	3.94
z	1.12	2.04	1.27	2.31	1.34	2.44	1.40	2.55
	−15 mm		−10 mm		−5 mm		5 mm	
	FWHM	FWTM	FWHM	FWTM	FWHM	FWTM	FWHM	FWTM
x	1.87	3.42	1.66	3.02	1.65	3.01	1.48	2.70
y	2.22	4.04	2.56	4.67	2.70	4.92	2.79	5.09
z	1.25	2.29	1.19	2.18	1.11	2.03	1.26	2.29
	10 mm		15 mm		25 mm		50 mm	
	FWHM	FWTM	FWHM	FWTM	FWHM	FWTM	FWHM	FWTM
x	1.53	2.79	0.76	1.39	1.37	2.49	0.92	1.68
y	3.26	5.95	3.10	5.64	3.27	5.95	3.03	5.53
z	1.16	2.11	1.16	2.12	1.21	2.20	1.08	1.97
	75 mm		90 mm					
	FWHM	FWTM	FWHM	FWTM				
x	0.56	1.01	0.63	1.15				
y	3.25	5.92	2.39	4.35				
z	1.09	1.99	0.99	1.80				
At 1/4 axial FOV from center								
	−90 mm		−75 mm		−50 mm		−25 mm	
	FWHM	FWTM	FWHM	FWTM	FWHM	FWTM	FWHM	FWTM
x	5.05	9.21	3.97	7.24	2.98	5.44	2.17	3.95
y	1.80	3.28	1.10	2.00	1.66	3.02	2.04	3.72
z	1.01	1.84	1.14	2.08	1.38	2.51	1.26	2.30
	−15 mm		−10 mm		−5 mm		5 mm	
	FWHM	FWTM	FWHM	FWTM	FWHM	FWTM	FWHM	FWTM
x	1.91	3.48	1.86	3.39	1.68	3.06	1.61	2.94
y	1.99	3.63	2.36	4.30	2.88	5.25	2.29	4.17
z	1.32	2.41	1.18	2.15	1.18	2.15	0.91	1.66
	10 mm		15 mm		25 mm		50 mm	
	FWHM	FWTM	FWHM	FWTM	FWHM	FWTM	FWHM	FWTM
x	1.77	3.24	1.42	2.59	1.64	2.99	1.10	2.01
y	2.94	5.36	2.76	5.04	2.54	4.63	3.80	6.92
z	1.02	1.86	1.00	1.82	0.81	1.47	1.10	2.00
	75 mm		90 mm					
	FWHM	FWTM	FWHM	FWTM				
x	1.07	1.96	1.24	2.26				
y	3.77	6.87	2.71	4.93				
z	1.27	2.31	1.12	2.04				

Table A.4.: Simulated spatial resolution values for a point source moved along the y-axis for the „stretched cylinder“ geometry.

Reconstructed image pixel size: 0.5 mm								
Slice thickness: 0.5 mm								
At axial center								
	−90 mm		−75 mm		−50 mm		−25 mm	
	FWHM	FWTM	FWHM	FWTM	FWHM	FWTM	FWHM	FWTM
x	1.68	3.06	1.11	2.02	1.21	2.20	1.20	2.19
y	5.24	9.55	4.52	8.24	3.52	6.42	2.78	5.08
z	1.24	2.26	1.23	2.23	1.22	2.23	1.18	2.15
	−15 mm		−10 mm		−5 mm		5 mm	
	FWHM	FWTM	FWHM	FWTM	FWHM	FWTM	FWHM	FWTM
x	1.30	2.37	1.32	2.41	1.40	2.56	1.40	2.56
y	2.87	5.23	2.52	4.59	3.00	5.47	2.95	5.38
z	1.34	2.44	1.17	2.13	1.15	2.09	1.20	2.19
	10 mm		15 mm		25 mm		50 mm	
	FWHM	FWTM	FWHM	FWTM	FWHM	FWTM	FWHM	FWTM
x	1.03	1.87	1.58	2.87	1.15	2.09	1.11	2.02
y	2.51	4.58	2.85	5.18	2.71	4.94	3.33	6.07
z	1.16	2.12	1.22	2.22	1.16	2.11	1.17	2.13
	75 mm		90 mm					
	FWHM	FWTM	FWHM	FWTM				
x	1.30	2.37	1.59	2.90				
y	4.38	7.97	4.96	9.04				
z	1.14	2.07	1.11	2.02				
At 1/4 axial FOV from center								
	−90 mm		−75 mm		−50 mm		−25 mm	
	FWHM	FWTM	FWHM	FWTM	FWHM	FWTM	FWHM	FWTM
x	1.50	2.73	1.36	2.49	0.67	1.22	1.09	1.99
y	6.54	11.92	5.95	10.85	5.41	9.87	3.87	7.06
z	1.18	2.15	1.03	1.88	1.01	1.83	1.00	1.82
	−15 mm		−10 mm		−5 mm		5 mm	
	FWHM	FWTM	FWHM	FWTM	FWHM	FWTM	FWHM	FWTM
x	1.13	2.07	0.95	1.73	0.81	1.48	0.83	1.51
y	4.01	7.31	4.04	7.36	3.58	6.53	3.65	6.66
z	0.93	1.69	0.84	1.53	0.82	1.49	0.84	1.53
	10 mm		15 mm		25 mm		50 mm	
	FWHM	FWTM	FWHM	FWTM	FWHM	FWTM	FWHM	FWTM
x	0.87	1.58	1.10	2.00	0.99	1.81	0.78	1.42
y	4.06	7.39	4.00	7.28	3.75	6.83	5.18	9.44
z	0.83	1.51	0.88	1.60	0.92	1.68	1.02	1.86
	75 mm		90 mm					
	FWHM	FWTM	FWHM	FWTM				
x	1.39	2.53	1.37	2.50				
y	5.98	10.90	6.22	11.33				
z	1.02	1.86	1.02	1.85				

Table A.5.: Simulated spatial resolution values for a point source moved along the x-axis for the „peanut“ geometry. Position values are relative to the center of the field of view at position $(-110, 0, 0)$ mm.

Reconstructed image pixel size: 0.5 mm								
Slice thickness: 0.5 mm								
At axial center								
	−90 mm		−75 mm		−50 mm		−25 mm	
	FWHM	FWTM	FWHM	FWTM	FWHM	FWTM	FWHM	FWTM
x	4.99	9.09	3.19	5.81	2.46	4.47	1.58	2.88
y	2.06	3.75	0.60	1.09	0.74	1.34	1.51	2.76
z	1.22	2.23	1.23	2.23	1.31	2.38	1.44	2.62
	−15 mm		−10 mm		−5 mm		5 mm	
	FWHM	FWTM	FWHM	FWTM	FWHM	FWTM	FWHM	FWTM
x	1.06	1.94	1.09	1.99	0.93	1.69	0.80	1.46
y	1.50	2.73	1.47	2.67	1.56	2.84	1.57	2.86
z	1.27	2.31	1.36	2.48	1.33	2.42	1.35	2.46
	10 mm		15 mm		25 mm		50 mm	
	FWHM	FWTM	FWHM	FWTM	FWHM	FWTM	FWHM	FWTM
x	1.05	1.91	1.04	1.91	1.41	2.56	3.17	5.77
y	1.61	2.94	1.33	2.42	1.86	3.40	2.65	4.82
z	1.36	2.48	1.18	2.16	1.36	2.48	1.17	2.14
	75 mm		90 mm					
	FWHM	FWTM	FWHM	FWTM				
x	4.57	8.33	4.22	7.69				
y	1.55	2.83	1.37	2.50				
z	0.97	1.77	1.09	2.00				
At 1/4 axial FOV from center								
	−90 mm		−75 mm		−50 mm		−25 mm	
	FWHM	FWTM	FWHM	FWTM	FWHM	FWTM	FWHM	FWTM
x	4.89	8.91	3.32	6.06	2.30	4.18	1.53	2.79
y	2.10	3.82	1.98	3.61	1.39	1.52	1.56	2.83
z	1.05	1.91	1.13	2.02	1.27	2.29	1.17	2.13
	−15 mm		−10 mm		−5 mm		5 mm	
	FWHM	FWTM	FWHM	FWTM	FWHM	FWTM	FWHM	FWTM
x	1.12	2.04	1.05	1.92	0.69	1.25	0.74	1.35
y	1.40	2.54	1.44	2.63	1.65	3.00	1.59	2.90
z	1.14	2.08	1.10	2.00	0.99	1.81	0.99	1.80
	10 mm		15 mm		25 mm		50 mm	
	FWHM	FWTM	FWHM	FWTM	FWHM	FWTM	FWHM	FWTM
x	0.96	1.75	1.09	1.99	1.30	2.37	2.90	5.28
y	1.69	3.08	1.25	2.27	1.50	2.73	1.96	3.57
z	1.00	1.82	1.12	2.04	1.09	1.98	1.29	2.36
	75 mm		90 mm					
	FWHM	FWTM	FWHM	FWTM				
x	4.69	8.54	4.91	8.94				
y	1.58	2.87	1.08	1.97				
z	1.16	2.11	1.02	1.86				

Table A.6.: Simulated spatial resolution values for a point source moved along the y-axis for the „peanut“ geometry.

Reconstructed image pixel size: 0.5 mm								
Slice thickness: 0.5 mm								
At axial center								
	−90 mm		−75 mm		−50 mm		−25 mm	
	FWHM	FWTM	FWHM	FWTM	FWHM	FWTM	FWHM	FWTM
x	1.57	2.86	1.47	2.68	0.75	1.37	0.86	1.57
y	5.03	9.17	4.37	7.97	3.04	5.55	1.76	3.21
z	1.21	2.20	1.41	2.56	1.31	2.39	1.25	2.27
	−15 mm		−10 mm		−5 mm		5 mm	
	FWHM	FWTM	FWHM	FWTM	FWHM	FWTM	FWHM	FWTM
x	0.79	1.44	0.78	1.42	0.57	1.04	0.56	1.02
y	1.58	2.88	1.30	2.38	1.13	2.05	1.08	1.96
z	1.40	2.56	1.30	2.37	1.37	2.50	1.35	2.47
	10 mm		15 mm		25 mm		50 mm	
	FWHM	FWTM	FWHM	FWTM	FWHM	FWTM	FWHM	FWTM
x	0.78	1.42	0.77	1.41	0.99	1.80	0.88	1.61
y	1.39	2.54	1.56	2.84	1.78	3.24	3.14	5.73
z	1.28	2.34	1.29	2.34	1.28	2.34	1.37	2.50
	75 mm		90 mm					
	FWHM	FWTM	FWHM	FWTM				
x	1.46	2.65	1.50	2.73				
y	4.34	7.92	5.31	9.67				
z	1.33	2.42	1.28	2.34				
At 1/4 axial FOV from center								
	−90 mm		−75 mm		−50 mm		−25 mm	
	FWHM	FWTM	FWHM	FWTM	FWHM	FWTM	FWHM	FWTM
x	1.27	2.32	1.52	2.77	0.94	1.72	0.94	1.71
y	5.35	9.76	4.42	8.06	3.03	5.52	1.64	2.99
z	1.29	2.35	1.38	2.51	1.36	2.47	1.14	2.08
	−15 mm		−10 mm		−5 mm		5 mm	
	FWHM	FWTM	FWHM	FWTM	FWHM	FWTM	FWHM	FWTM
x	0.75	1.38	0.73	1.32	0.53	0.96	0.51	0.92
y	1.48	2.70	1.33	2.43	0.94	1.72	0.97	1.76
z	1.14	2.08	1.11	2.02	1.17	2.13	1.16	2.11
	10 mm		15 mm		25 mm		50 mm	
	FWHM	FWTM	FWHM	FWTM	FWHM	FWTM	FWHM	FWTM
x	0.75	1.37	0.76	1.38	0.97	1.77	0.87	1.59
y	1.40	2.55	1.52	2.77	1.69	3.08	3.00	5.46
z	1.13	2.06	1.14	2.08	1.12	2.04	1.31	2.38
	75 mm		90 mm					
	FWHM	FWTM	FWHM	FWTM				
x	1.28	2.33	1.48	2.71				
y	4.41	8.04	5.26	9.58				
z	1.23	2.23	1.14	2.08				

Acknowledgments

An dieser Stelle möchte ich mich bei allen Personen bedanken, die zum Gelingen dieser Masterarbeit beigetragen haben. Ein besonderer Dank gebührt folgenden Personen:

- Prof. Dott. Andrea Santangelo für das Ermöglichen und Bereitstellen der sehr interessanten Forschungsthemen, der Korrektur dieser Masterarbeit sowie für das Ermöglichen der Kollaboration mit dem WSIC.
- Prof. Dr. Bernd Pichler für die Kollaboration von Seiten des WSIC sowie das Ermöglichen der produktiven Reise nach Rockford.
- Dr. Chris Tenzer und Dr. Sebastian Diebold für die hervorragende Betreuung, die offenen Türen zu allen Zeiten, das Beantworten sämtlicher Fragen, das Korrekturlesen dieser Arbeit und den Espresso.
- Fabian Schmidt für die Unterstützung und Betreuung von Seiten des WSIC, das Beantworten aller Fragen, das Durchführen der Validierungsmessung sowie der Gesellschaft in Rockford,
- Dr. Johannes Breuer für die wertvollen Ideen und Diskussionen sowie das Durchführen der Simulation des Validierungsexperiments mit PETSim,
- Dr. Matthias Schmand and the team at SHS DI MI DC R&D in Rockford. Thank you for the very helpful tips, conversations, discussions and all the time you have given us.
- Meinen Mitstudierenden im Büro für die allzeit gute Stimmung.
- All of the members at the IAAT. It is a pleasure working with you.

Ein ganz besonderer Dank geht an meine Familie und meine Freundin Sabrina für die anhaltende Unterstützung über den gesamten Zeitraum meines Studiums hinweg, insbesondere auch bei meiner Rückkehr an die Universität für das Masterstudium.